# ADVANCED CARBON-BASED NANOCOMPOSITE CATHODES FOR ENERGY HARVESTING AND STORAGE

By

Mesut Yilmaz

Dissertation

Submitted to the Faculty of the

Graduate School of Vanderbilt University

in partial fulfillment of the requirements

for the degree of

DOCTOR OF PHILOSOPHY

in

Electrical Engineering

August 31st, 2019

Nashville, Tennessee

Approved:

Professor Weng P. Kang

Professor Supil Raina

Professor William Hofmeister

Professor Deyu Li

Professor Bharat Bhuva

*To my dear family*

# ACKNOWLEDGMENTS

I would like to thank my advisors, Dr. Weng Poo Kang and Dr. Supil Raina, and evince my gratitude to them for sharing their wisdom with me throughout my research studies and providing me a valuable opportunity to conduct my research. They always motivated me throughout my studies and helped me equip myself with the capabilities and tools that are vital to become a successful scientist. I also want to thank my colleagues, Dr. Shao-Hua Hsu, Dr. Siyu Wei, and Dr. Serkan Akbulut and Mick Howell, for their keen support on my experiments.

In addition, I would like to express my appreciation to professors Bharat Bhuva, Deyu Li, and William Hofmeister for serving on my Ph.D. committee and providing their valuable opinions.

I am also thankful to Dr. Anthony Hmelo and Dr. Dmitry Koktysh for their splendid support during my use of the VINSE equipment.

Lastly, I would like to express my appreciation to my department, Electrical Engineering, and the Graduate School, for their financial and educational support, which enabled me to complete my Ph.D. studies. I also want to thank Linda Koger, Lauren Fox, and Devin Rogers for their precious administrative help.

# TABLE OF CONTENTS

# LIST OF TABLES

# LIST OF FIGURES

Figure Page

# LIST OF SYMBOLS

| Symbol | Meaning |
|---|---|
| A | Area |
| Ag | Silver |
| AgCl | Silver chloride |
| Ah | Ampere-hour |
| Al | Aluminum |
| Ar | Argon |
| β | Beta, frequency independent parameter of CPE |
| Cd | Cadmium |
| $CH_4$ | Methane |
| $C_2H_2$ | Acetylene |
| $C_2H_4$ | Ethylene |
| Co | Cobalt |
| CO | Carbon monoxide |
| *D* | Diffusion coefficient |
| $e_0^-$ | Elementary charge |
| $e_{CB}^-$ | Conduction band electron |
| *eV* | Electron Volt |
| *E* | Energy |
| η | Efficiency |
| F | Farad |
| $Fe_3O_4$ | Ferroferric oxide |

GaAs……..……Gallium arsenide

GaSb……..……Gallium antimonide

*h*……..……Planck's constant

*c*……..……Speed of light

*c*……..……Concentration

*C*……..……..……Capacitance

C……..……Current rate

Co……..……Cobalt

*F*……..……..……Faraday constant

Fe……..……..……Iron

$H_2$……..……Hydrogen

$H_2SO_4$……..……Sulfuric acid

Hz……..……Hertz

*I*……..……Current

$I^-$……..……Iodide

$I_3^-$……..……..……Triiodide

*J*……..……..……Current density

*k*……..……..… Boltzmann constant

*K*……..……Kelvin

KCl ……..……Potassium chloride

kg……..……..……Kilogram

KOH……Potassium hydroxide

$KMnO_4$……..…Potassium permanganate

$K_2SO_4$……...Potassium sulfate

*L*…… Distance

Li……Lithium

$LiBF_4$……..Lithium tetrafluoroborate

$LiClO_4$…… Lithium perchlorate

$LiCoO_2$…… Lithium cobalt oxide

$Li_2(Fe_xMn_yCo_z)SiO_4$…….Dilithium ternary silicate

$LiFePO_4$……..…….Lithium iron phosphate

$Li_2FeSiO_4$……..…….Lithium iron silicate

$Li_2MnSiO_4$…… Lithium manganese silicate

LiI……..Lithium iodide

$LiPF_6$……..Lithium hexafluorophosphate

m……..……An integer used for creating the vector (n,m)

*m*……..……Meter

M……Molar weight

MH……Metal hydride

$MnO_2$……..Manganese dioxide

*μ*……Electrochemical potential

n……...Integer used to create vector (n,m)

*n*……...Number of electrons, or a positive integer for Bragg's equation

$N_2$…… Nitrogen

Na……Sodium

$Na_2SO_4$……...Sodium sulfate

$NH_3$……..……Ammonia

$N_2H_4$…….……Hydrazine

Ni…….……Nickel

NiOOH……..……...…Nickel oxide hydroxide

nm…….……Nanometer

Ω……Ohm

$^oC$……Degree Celcius

*P*……..……..……Power

Pb…… Lead

$PbO_2$……..……..…… Lead oxide

$PbSO_4$……..……..…… Lead sulfate

Pt……..……Platinum

q……..……An integer

*Q*……..……Charge

R…….……..……Resistance

$R_O$…….…....Reduced component of the redox couple

rpm……..……...Rotation per minute

$R_R$……..……Oxidized component of the redox couple

$RuO_2$…….Ruthenium dioxide

*s*……Second

S……..Sulfur

Si……Silicon

$SiO_2$…….…….Silicon dioxide

$SnO_2$……..Tin dioxide

*sq*……..Square

*SR*……..……...Scan rate

*T*……..Temperature

TEABF4…….Tetra ethyl ammonium tetrafluoro borate

Ti……Titanium

$TiO_2$……..Titanium dioxide

*V*……..…Voltage

$V_2O_5$……..…Vanadium pentoxide

λ…….…….. …….. Wavelength

*ω*…… ……..……..Admittance

W…… ……..……Tungsten

Wh…… ..……Watt-hour

Z…… ……Impedance

Zn…… …… ……..……Zinc

ZnO …….……...Zinc oxide

# LIST OF ABBREVIATIONS

| Abbreviation | Word/Phrase |
|---|---|
| 3D | 3-Dimensional |
| AC | Activated Carbon |
| ACN | Acetonitrile |
| ALD | Atomic Layer Deposition |
| AM | Air Mass |
| CB | Carbon Black |
| CNT | Carbon Nanotube |
| CVD | Chemical Vapor Deposition |
| c-Si | Monocrystalline Silicon |
| CPE | Constant Phase Element |
| ct | Charge Transfer |
| CV | Cyclic Voltammetry |
| D | Dye |
| DEC | Diethyl Carbonate |
| dl | Double Layer |
| DMC | Dimethyl Carbonate |
| DSSC | Dye-Sensitized Solar Cell |
| DTS | Dilithium Ternary Silicate |
| EC | Ethylene Carbonate |
| EDLC | Electric Double Layer Capacitor |
| EIS | Electrochemical Impedance Spectroscopy |

EMC……...Ethyl Methyl Carbonate

EV……..……Electric Vehicle

FF……..……Fill Factor

FTO…… Fluorine-Doped Tin Oxide

G…….……Global

GIC……..…..…Graphite Intercalation Compound

h…….hour

HEV……..……Hybrid electric vehicles

HFCVD…….Hot Filament Chemical Vapor Deposition

HMDS……Hexamethyldisilazane

HOMO……..……..Highest Occupied Molecular Orbital

ICP-MS……...…Inductively Coupled Plasma- Mass Spectrometry

ITO……..…… Indium-Doped Tin Oxide

ICP-MS……...Inductively Coupled Plasma- Mass Spectrometry

LFP…….$LiFePO_4$

LIB……..…….……Lithium-Ion Battery

LiTFSI……...……..Lithium Bis(trifluoromethanesulfonyl)Imide

LUMO…….....Lowest Unoccupied Molecular Orbital

MA-CNT……Micro-Array Carbon Nano Tube

min……...minutes

MWCNT……..……Multi-Walled CNT

NBB……..……Sodium-Beta-Alumina Battery

NMP……..……N-Methyl Pyrrolidone

OC……Open-Circuit

PC……Photocapacitor

P-CNT…… Planar CNT

pc-Si…… ……..Polycrystalline Silicon

PVA…… ……..…… Poly Vinyl Alcohol

PVDF…… ……..…… Polyvinylidene Fluoride

redox…… ……..…….Reduction-Oxidation

SC…… ……..……Short Circuit

SEI……..…… ……Solid Electrolyte Interphase

SEM……Scanning Electron Microscope

SWCNT……...……...Single-Walled CNT

TEOS……..…… ……Tetra Ethyl Ortho Silicate

TNT……..Titanium dioxide Nanotube

VACNT……..… ……..Vertically-Aligned CNT

XRD……X-Ray Diffraction

# CHAPTER I

# INTRODUCTION AND BACKGROUND

## 1.1. Carbon Nanotubes

Carbon is an abundant element on earth. Recently, many advanced carbon allotropes have been devised, including graphene, carbon nanotubes (CNTs), carbon nanofibers, and nanodiamond [1,2]. Graphene, a single layer of graphite, is a one-atom-thick sheet of carbon atoms ordered in hexagonal arrays. Rolled-up graphene sheets, on the other hand, are CNTs. Based on the number of rolled graphene sheets, they are called single or multi-walled CNTs (SWCNTs or MWCNTs). Since the publication of Lijima and others' work in 1991, CNTs have been of intense interest for the researchers and industry [3]. They have extraordinary material properties such as high electrical and thermal conductivity, strong mechanical strength, good photoconductivity, extreme chemical inertness, high aspect ratio, and tune-ability of the nanostructure features [4-7]. Accordingly, CNTs have been used in a wide variety of applications such as supercapacitors, batteries, solar cells, actuators, lightweight electromagnetic shields, transistors, paints, composite materials for enhanced reinforcement, filters, drug delivery systems, and so on [8,9]. Many other applications, which utilize CNTs, are also likely to emerge in the future.

## 1.1. Solar Energy Harvesting

The world's ever-increasing energy demand and related problems, pollution and global warming, have called for cleaner and renewable energy supplies. The primary renewable energy sources are wind, solar, wave and tidal, biomass, hydroelectric, and geothermal. With 75% of the worlds' population living in the Sun Belt, where the solar irradiation is as high as producing average energy of 2000 $kWh/m^2$ per year: harvesting this energy becomes a promising solution to help solve the global energy challenge [10]. There have been many approaches in this respect like concentrated solar power, where the concentrated heat of sun rays is first converted into mechanical energy and then to electricity; solar thermal, in which the solar energy is used to heat the heat transfer fluid and used as a direct heat source; solar cooling, where a chemical sorbent compound uses solar energy for cooling; artificial and natural photosynthesis, where a chemical fuel is created through photosynthesis either with practical chemicals, or with photosynthetic organisms, respectively [11]; photovoltaics, where the solar energy is converted directly to electric energy via photovoltaic semiconducting materials [12].

## 1.2. Energy Storage

As the global energy challenge remains a critical issue, the cost of energy production and the flexibility/availability for using it independently of time and location have made energy storage a priority. Historically, the most popular and the lowest cost energy storage system is hydroelectric power plants, where the

water is collected into high altitude lakes, and when the energy is demanded it flows downhill through turbines; the gravitational potential energy is converted first into kinetic energy, and then to electric energy. In 2016, 16.4% of the world's total electricity generated was obtained through hydroelectric power plants [13]. Other less popular alternatives include using compressed air and flywheels for storing potential and kinetic energy, respectively, but they're not feasible for large-scale systems [14]. Fuel cells are another way of storing energy, by bypassing the heat-generating stage in their chemical reaction; chemical energy is directly converted into electrical energy. A typical fuel cell consists of two electrodes and an electrolyte, and the common fuel is pure hydrogen ($H_2$) or hydrogen-containing agents: methanol, methane, hydrogen sulfide, and hydrazine. Alternatively, people have also used carbon monoxide [15]. When the energy density, load leveling, mobility, smooth energy output (constant voltage), and carbon emissions are concerned, batteries can be deemed as the future of the energy storage [14,16,17]. On the other hand, supercapacitors are a possible alternative for batteries in the case of high-power requirements, but unable to operate at fixed voltages. In Figure 1.1, the Ragone plots show the operational difference between batteries and electric double layer supercapacitors (EDLC), which tend to excel in energy density and power density, in order [18].

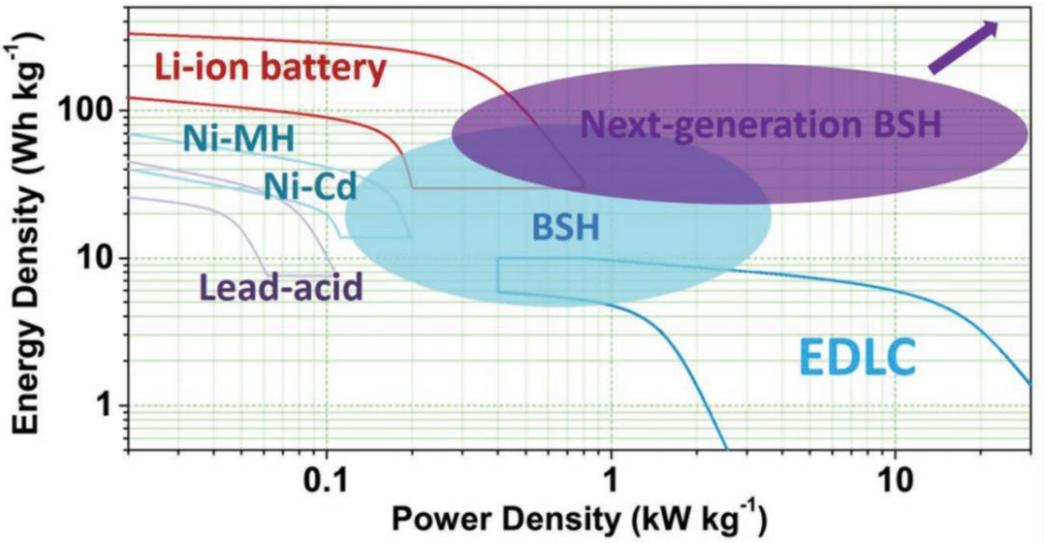


Figure 1.1 Ragone plots of batteries, electric double-layer capacitors (EDLCs), and battery supercapacitor hybrids (BSHs) [18].

## 1.3. The Aim of the Research

The objective of this research is to develop novel cathodes utilizing the advanced features of carbon-based nanocomposite materials, especially carbon nanotube-based composites. The fabricated cathodes are to be used in energy-related applications: dye-sensitized solar cells (DSSCs), photocapacitors, and lithium-ion batteries.

Electrodes using carbon nanomaterials have been actively investigated recently, and they, especially CNTs, are suggested as the preferred electrode material for energy conversion and solving the energy storage bottlenecks [19,20].

Conventional DSSC counter electrodes (cathodes) are made of platinum (Pt) metal, which is a high-performance catalyst but unfortunately corrodes in the electrolytes with the iodide/triiodide redox couple; that has prompted to the search of more durable and less expensive alternative materials such as carbon-

based nanomaterials. CNTs have shown competitive catalytic performance to Pt in DSSCs, but there has not been any report using micro-patterned vertically aligned CNTs (VACNTs) nor their composite as a DSSC counter electrode [21].

Scientists have also tried to combine DSSCs with the energy storage feature in a single device, either with batteries or capacitors. In the DSSC-capacitor combination (also called photocapacitor), single-cell integration has always been a big challenge, and the charged voltage of the photocapacitors was lower than that of DSSCs'. Besides, mostly the conventional DSSC electrolytes were used in the compact two-electrode photocapacitors, which have compatible redox couples for a DSSC operation but are not always suitable for the capacitor operation.

There has been an immense amount of research interest in the DoD for developing Li-ion based batteries with high-energy and high-power density, and high operating voltage (more than 300 mAh/g specific capacity and higher than 4 V operating voltage), using novel active cathode materials. In order to exploit the most from the cathode, the conventional cathode structure, hence the fabrication technique must be changed to a simpler yet effective one, as some of the researchers have been trying to achieve.

In my studies, I have achieved the following by developing CNT-based nano-structured cathodes for energy applications, including DSSCs, photocapacitors, and Li-ion batteries:

- Fabrication of micro-array patterned CNTs (MA-CNTs) counter electrode and testing it in a DSSC to replace the conventional Pt-film electrodes;

- Development of a two-electrode, compact photocapacitor with an electrolyte which has never been practiced with DSSCs before;
- Photovoltaic and capacitive performance analyses of the photocapacitor;
- Development of a novel active cathode material, $Li_2(Fe_xMn_yCo_z)SiO_4$ dilithium ternary silicate (DTS), which has a high theoretical capacity and operating voltage;
- Analysis of the DTS material through a scanning electron microscope (SEM), X-Ray diffraction (XRD), and inductively coupled plasma- mass spectrometry (ICP-MS);
- Electrochemical characterization of the DTS as active cathode material in a pouch cell configuration;
- Synthesize microarray patterned CNTs on Al (MA-CNT/Al), which is used as a novel host material for the cathode in LIBs;
- Utilization of MA-CNT/Al as the host for electrophoretically deposited $LiFePO_4$, and electrochemical characterization of this cathode in a LIB cell.

## 1.4. Organization of the Dissertation Proposal

This thesis has eight chapters, and they are arranged as follows:

- ***Chapter I*** includes the background information about carbon nanotubes, the emerging solar energy harvesting using DSSC, and

literature survey of the energy storage solutions. The purpose of this research is also detailed in this chapter.

- ***Chapter II*** covers a review of the recent technologies about carbon nanotube fabrication. Dye-sensitized solar cells and supercapacitors made of different electrodes are reviewed. Recent advancements in photocapacitors were also included. Developments in battery technologies, especially in lithium-ion batteries, are overviewed.
- ***Chapter III*** has detailed information about the fabrication of our dye-sensitized solar cells with an iodide-based electrolyte. Micropatterning of the vertically aligned carbon nanotubes is described in this chapter. The synthesis of vertically aligned carbon nanotubes on Si using a hot filament chemical vapor deposition system is also explained. The structural and photovoltaic analyses of the cells with carbon nanotube-based cathodes were carried out.
- ***Chapter IV*** elaborates the work done to fabricate compact, two-electrode photocapacitors. The photovoltaic and capacitive performances of the photocapacitors, which have $MnO_2$ and carbon nanotube-based cathodes, are analyzed.
- ***Chapter V*** is about the synthesis of a novel lithium-ion battery cathode material with a high theoretical specific capacity. Structural and electrochemical analyses of the novel cathode material were carried out via SEM, ICP-MS, XPS, XRD, charge-discharge, and AC impedance tests.

- ***Chapter VI*** entails the work done to fabricate a new cathode host structure, micro-array patterned carbon nanotube on Al. Accompanied with different cathode material deposition techniques, for achieving a novel MA-CNT/Al electrode incorporated with $LiFePO_4$ in a LIB cell, the cathode's structural and electrochemical performance are investigated.
- ***Chapter VII*** describes the novel binder-free LIB cathode fabrication method. It is based on the in-situ fabrication of the lithium iron phosphate cathodes by a sol-gel process on CNT arrays on Al substrates.
- ***Chapter VIII*** provides conclusions of this thesis and directions for further study.
- ***Appendix A*** covers uncertainty analysis performed for our measurements and calculations.

# CHAPTER II

# LITERATURE REVIEW

## 2.1. Carbon Nanotube Structure and Synthesis

A single layer of carbon atoms, arranged in a honeycomb lattice, form a graphene sheet. Rolling the graphene sheet around a lattice vector, (n,m), results in a single-walled carbon nanotube (SWCNT) [20]. The lattice vector determines the diameter and chirality of the nanotube, such that it can be in either armchair (n = m), zigzag (n = 0), or chiral (other n,m combinations), as shown in Figure 2.1 [22]. The chirality of carbon atoms, which is expressed as the chiral angle between

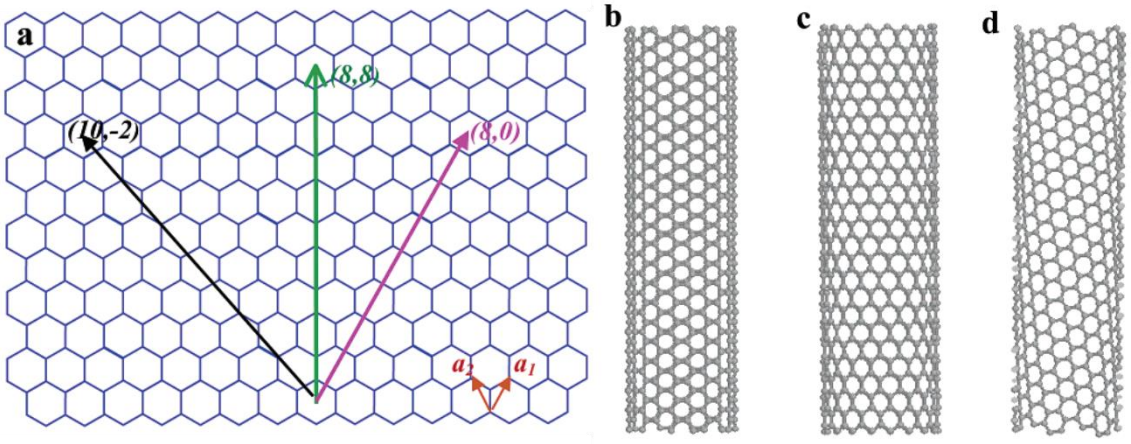


Figure 2.1 (a) Schematic of a graphene sheet in a honeycomb structure. The basis vectors are denoted as $a_1$ and $a_2$ and used to create lattice vectors, along which single-walled carbon nanotubes can be created by folding the sheet. Accordingly, lattice vectors (8,8), (8,0), and (10,-2) yield to armchair (b), zigzag (c), and chiral (d) nanotubes, respectively [22].

the tube axis and the hexagon, defines the electrical properties of SWCNTs to be either metallic or semiconducting; if 2n+m = 3q (q is an integer), the nanotube is metallic [20,22]. Besides, MWCNTs, which are rolled up multilayered graphene sheets with an interlayer distance of ~3.4 Å, exhibit mostly metallic behavior. CNTs can be synthesized in either non-oriented (randomly entangled and spaghetti-like), or oriented (vertically aligned and forest-like) alignments [23]. Recent research studies have shown the feasibility of growing CNTs on various types of substrates [23].

A key element in the CNT growth is the catalyst, which is deposited onto the substrate initially and preferably onto a buffer layer on the substrate. During the growth process, at high temperatures, it breaks down into nanoparticles with a diameter directly proportional to the catalyst thickness. Carbon atoms diffuse into these catalytic particles in the hexagonal orientation and precipitate to form the nanotube, while the buffer layer acts as a barrier against carbon atoms' further diffusion into the substrate. Figure 2.2 shows the schematic stages of CNT growth on a $SiO_2$/Si substrate with an emphasis on the carbon-catalyst interaction [24]. By varying the thicknesses of catalyst from a few to tens of angstroms thick, the resulted CNT formations would vary from SWCNTs to well-aligned MWCNTS to intertwined MWCNTs [25]. According to Moulton et al., the individual tube diameter is also proportional to catalyst thickness, since the amount of carbon atoms diffusing into the catalyst nanoparticle increases with the particle size [25]. Iron, nickel, cobalt, and their alloys have been the most popular catalysts because their carbon diffusion coefficients are high, varying from $0.4\times10^{-10}$ to $1\times10^{-10}$ $m^2/s$ at $T$ = 1173 – 1373 $^oK$, for a single metal [26,27].

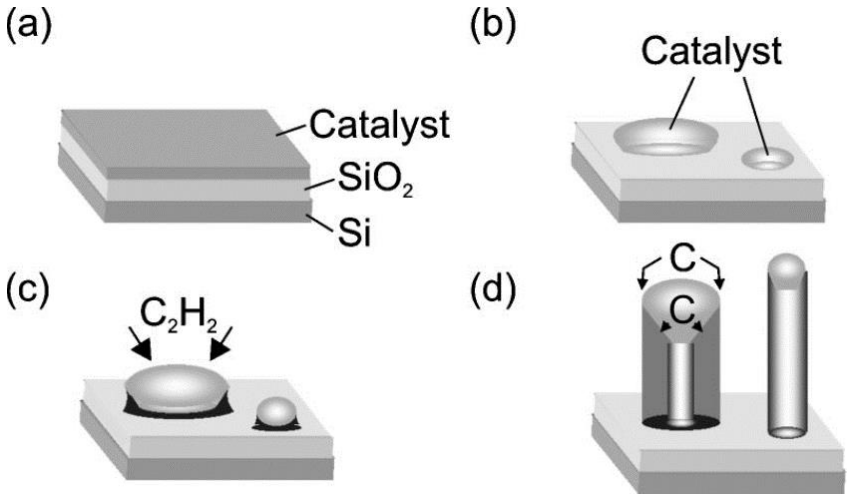


Figure 2.2 Schematic stages of the CNT growth for single and multi-walled tubes. (a) A catalyst layer deposited onto a $SiO_2$/Si substrate. (b) The catalyst film fragmented into nanoparticles at high temperatures. (c) The carbon source ($C_2H_2$ gas) decomposes and initiates the CNT growth. (d) Carbon atoms diffused through the catalyst nanoparticles yield to the growth of either MWCNT (under big nanoparticles) or SWCNT (under small nanoparticles) [24].

Arc discharge, laser ablation, and chemical vapor deposition (CVD) are the prevalent methods for synthesizing CNTs [20,28]. Particularly, CVD has distinctive advantages like allowing the CNT growth at lower temperature directly on a substrate, and compatible with the conventional micro-fabrication process [28]. These include plasma-enhanced CVD, microwave plasma CVD, laser-induced CVD, and hot filament CVD (HFCVD) [28-33].

In a CVD process, there is an energy source that is used to break down the precursor gases at high temperatures as well as to heat the samples, break down the catalyst film into nanoparticles, and start the CNT growth [28]. An HFCVD uses a hot filament (preferably tungsten (W)) as the primary heat source to decompose the precursor gases along with a heating stage to control the substrate temperature and has been very efficient for growing VACNT forests

[34-36].

Precursor gases are the other key elements in the CNT synthesis. For example, hydrogen ($H_2$), ammonia ($NH_3$), and hydrazine ($N_2H_4$) are well known reducing agents, which keep the catalyst surface active. They can also be used as cooling agents after synthesis [28,36]. Ammonia, on the other hand, helps to maintain the alignment of the CNTs during the growth process by etching amorphous carbon, which occurs at the tip of the CNTs because of catalyst particle exhaustion [37,38]. There are also different hydrocarbon gases that have been utilized as the carbon source: commonly ethylene ($C_2H_4$), acetylene ($C_2H_2$), and methane ($CH_4$); occasionally carbon monoxide (CO), alcohols, benzene, and other gases [28].

Nucleation of the CNTs and their continuous synthesis in a CVD system are very fragile processes, which are affected by substrate and filament temperatures, chamber pressure, and precursor-gases' flow rates and residence times. Substrate temperatures required for adequate catalysis typically range from 400 to 900 $^oC$ [28]; working at lower temperatures might need compensation with longer reduction-gas residence time. Besides, different hydrocarbon gases' thermal decomposition starts at varying temperatures because of varying interatomic bonds. For example, in hot filament CVD systems, Ishikawa et al. heated the filament to 1500 $^oC$ (minimum) to decompose $C_2H_4$; Cojocaru's group used 1800 $^oC$ for $C_2H_2$; we and the other researchers have been using 2000$^oC$ to 2100 $^oC$ filament temperatures to break down $CH_4$ [36,39,40].

### 2.1.1. Raman Spectroscopy

Raman Spectroscopy is a light scattering technique which is based on the incident radiation's inelastic scattering after interacting with vibrating molecules. When a sample is illuminated with a monochromatic laser beam, the molecules of the sample interact with the photons and emit a scattered light, which has a frequency different than that of the incident light. Raman spectrum consists of these molecule-specific scattered light intensities at varying wavelengths [41].

Structural analysis of the carbonaceous materials is mostly carried out using Raman spectroscopy. This technique provides information about the crystalline quality of the MWCNTs through the D-band to G-band peak intensity ratio [42]. Besides, the diameter of the CNTs, the effect of inter-tube interactions on the vibrational modes, disorders of the $sp^2$-hybridized carbon materials are some of the fundamental aspects that can be obtained from Raman spectroscopy [43].

## 2.2. Solar Photovoltaic Cells

Among different solar harvesting technologies, photovoltaics, also called solar cells, step forward with in-situ solar to electric energy conversion and better applicability to mobile platforms, since their discovery in 1839 [44]. A solar cell consists of a semiconducting material to generate electricity when exposed to light. Scientists were able to record the energy distribution of the solar irradiation coming to earth in wide wavelengths, ranging from $\lambda$ = 280 to 4000 nm. Since more than 95% of this solar energy is in between $\lambda$ = 280 to 2500 nm, scientists

are aiming at harvesting the photons in this spectrum [45]. The energy ($E$) of a photon is derived from the equation:

$$E(joules) = \frac{h\,c}{\lambda} \quad (2.1),$$

where $h$ is Planck's constant, and $c$ is the speed of light. The energy required for a photon to fall through a potential of 1 Volt, is

$$E(eV) = \frac{E(joules)}{1.602 \times 10^{-19}} \quad (2.2).$$

Based on the equations (1) and (2), photovoltaic materials used in solar cells allow harvesting photons in a specific range of wavelength, hence operate in a limited bandgap, which is measured in electron-volts (eV). There are many parameters to evaluate the performance of a solar cell: solar conversion efficiency ($\eta$) is the ratio of the energy output of the device to the total solar energy received; fill factor ($FF$) is the ratio of maximum practical power ($P_{max}$) to maximum theoretical power of the device; open-circuit potential ($V_{OC}$) is the maximum potential the device can reach and is determined at zero current; short circuit current ($I_{SC}$) is the maximum current that can be drawn from the device and at zero potential. These parameters are determined from the photocurrent vs. voltage ($I$-$V$) test of the device, as shown in Figure 2.3 [44]. The following equations express the maximum power, fill factor, and solar efficiency of a photovoltaic cell, respectively:

$$P_{max} = I_m \times V_m \quad (2.3),$$

$$FF = \frac{P_{max}}{V_{OC} \times I_{SC}} \quad (2.4),$$

and

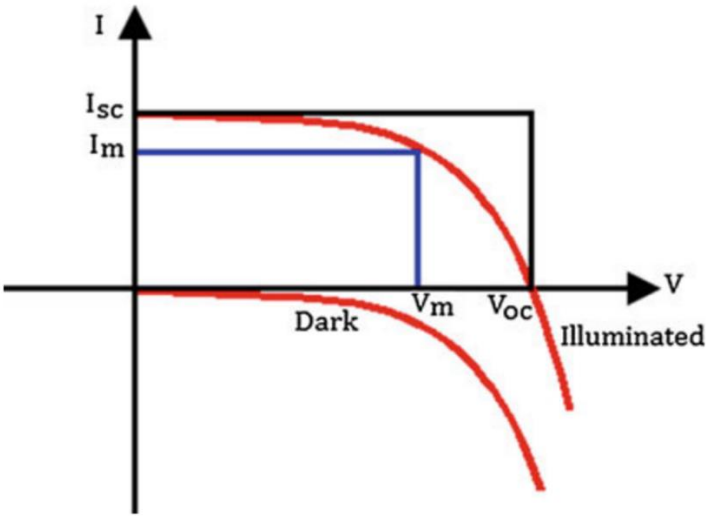


Figure 2.3 The current (*I*) vs. voltage (*V*) curve of a p-n junction (as a photovoltaic cell) under illumination and in the dark [44].

$$\eta = \frac{P_{max}}{P_{in}} = \frac{V_{OC} \times I_{SC} \times FF}{P_{in}} \qquad (2.5),$$

where $I_m$ and $V_m$ are current and voltage values, respectively.

Depending on the semiconducting material along with the photosensitizer used, different types of solar cells have been fabricated: monocrystalline silicon solar cells, polycrystalline silicon solar cells, thin-film solar cells, multi-junction solar cells, polymer solar cells, quantum structured solar cells, and DSSCs [44]. Silicon-based monocrystalline (c-Si) and polycrystalline (pc-Si) solar cells are the first examples of solar cells made and use different purity of crystalline silicon as the semiconductor to create a p-n junction. While c-Si solar cells have efficiencies more than 20%, its fabrication-cost/efficiency ratio is very high; pc-Si solar cells cost less but have lower efficiency; c-Si and pc-Si solar cells also are not readily applicable to integrated photovoltaic but are better for large-scale systems [45-47]. Thin-film solar cells, on the other hand, come with flexibility and

transparency and use less material while sacrificing efficiency, making them suitable for small-scale systems [45,48]. Starting in the 1960s, in order to exploit a broader spectrum of solar irradiation, and hence, to obtain more energy, scientists employed a variety of photovoltaic materials with different bandgaps on a single device, called multi-junction cells [44]. As of 2017, Lumb et al. claimed to have a very high efficiency of 44.5% from their 5-junction solar cell that is based on gallium arsenide (GaAs) and gallium antimonide (GaSb) semiconducting materials [49]. Even though this technology can yield very high efficiencies with complex structures, the high fabrication cost is an issue. Polymer solar cells, which employ polymer semiconductors as the photovoltaic material, are well known for their flexibility and low-cost [44]. However, they suffer from a short lifetime and low efficiencies [44]. In most of the single bandgap solar cells, when the photon energy in a light beam is higher than the energy bandgap of the cell's semiconductor, the excess energy is lost as electron-phonon recombination or heat [44]. As a new technology, quantum structured solar cells utilize quantum dots, whose sizes are smaller than the exciton Bohr radius, reduce the hot carrier cooling rate, thus increasing the impact ionization and enhancing the photovoltaic efficiency [44,50]. Another merit of the quantum dot solar cells is the tunability of energy bandgap through the size of the quantum dot. However, considerable research is still required to improve their low energy conversion efficiencies [44].

### 2.2.1. Dye-Sensitized Solar Cells

Dye-sensitized solar cells (DSSCs), since their invention in 1991, are considered to be one of the most prominent new generation solar cells [44,51].

DSSCs offer high conversion efficiencies, ease of fabrication, and low-cost manufacturing. A typical DSSC generally consists of a photoanode, an electrolyte, and a counter electrode. The photoanode contains a transparent substrate (glass or plastic) covered with an electrical conductive layer (fluorine-doped tin oxide-FTO, or indium-doped tin oxide-ITO) for light absorption and electron transport and a wide bandgap semiconducting layer ($TiO_2$, ZnO, or $SnO_2$) coated and sensitized with dye molecules (acting as electron pumps) for the photoexcitation and photoinduced electron transfer. The electrolyte is composed of a redox mediator (mostly iodide based iodide/triiodide couple, $I^-/I_3^-$) for the regeneration of dye and itself. The counter electrode (typically Pt), on the other hand, catalyzes the redox couple's regeneration and captures the generated electrons [52,53]. Under the exposure to a light source of a DSSC, when the photoanode absorbs the photons, the dye (D) gets excited ($D \rightarrow D^*$) and releases the electron from its lowest unoccupied molecular orbital (LUMO) to the conduction band of the semiconducting layer, yielding an oxidized dye ($D^* \rightarrow D^+$). Subsequently, the electron passes through the external load and migrates to the cathode, stimulating the redox reactions in the redox couple (reduced component-$R_R$, and oxidized component-$R_O$). Afterward, $R_R$ gets oxidized and the dye is reduced ($D^+ \rightarrow D$). The reduction of the dye also happens in a dark reaction, where a semiconductor's conduction band electron ($e_{CB}^-$) combines with the oxidized dye. Besides, an $e_{CB}^-$ which migrated through the external load to the cathode regenerates the iodide by reducing the triiodide. Upon these reaction mechanisms, the highest $\eta$ obtained for a DSSC is 14% in full sunlight at air mass (AM) 1.5 global (G) [54].

*2.2.1.1 DSSCs with Pt-Free Counter Electrodes*

Among the DSSC counter electrodes, Pt has been a well-known catalyst material because of its excellent catalytic reactivity on reducing $I_3^-$ to $I^-$. However, Pt is an expensive, rare metal, and it corrodes in iodide-based electrolytes, causing the formation of $PtI_4$ [55]. Therefore, various Pt-free counter electrodes for DSSCs have been developed by scientists, mostly employing iodide-based electrolytes accompanied with the dye-sensitized $TiO_2$ photoanodes. Kang et al. used carbon black (CB) and 3D network epoxy polymer composite based counter electrode in their DSSCs. Their Pt-free flexible counter electrodes could only yield maximum short circuit current density ($J_{SC}$) of 14.9 mA/cm$^2$ [55]. Roy-Mayhew et al. developed DSSC cathodes with functionalized graphene sheets (FGS), which have a large surface area, lattice defects, and oxygen-containing functional groups for high catalytic activity. During the photovoltaic tests, their device reached $J_{SC}$ of 13.16 mA/cm$^2$ and $\eta$ of ~5% [56]. Shi et al. investigated the applicability of new catalytic material, $CoNi_2S_4$, for the counter electrode of their DSSC. They were able to achieve $J_{SC}$ of 8.86 mA/cm$^2$, and $\eta$ of 4.61% [57]. Carbon nanotubes have also been a prevalent material for the Pt-free cathodes. Zhang et al. tried to fabricate a low-cost counter electrode with carbon nanotube-based conductive composite polymer (CNT-CCP) film for their DSSC's cathode. Their device's $J_{SC}$, $V_{OC}$, and $\eta$ were 12.35 mA/cm$^2$, 0.64 V, and 4.47%, respectively [58]. Han et al. made a DSSC cathode with polyelectrolyte (poly(styrene-4-sodiumsulfonate))-grafted MWCNTs, which is prepared through an electrostatic

spray method. The highest $J_{SC}$ and $V_{OC}$ they obtained were 16.63 mA/cm$^2$ and 0.692 V, in order [59].

## 2.3. Supercapacitors

Intermittent power loading from the renewable energy production plants into the grid systems, photovoltaic powering of small mobile devices, storing the high kinetic energy via regenerative braking in state-of-the-art vehicles from cars to maglev trains, driving electric cars at high speed or acceleration are bringing a quest for a high-power and charge load-flexible energy storage solution. A supercapacitor, or ultracapacitor, is an energy storage device that has components similar to a battery: two electrodes, electrolyte, and a separator to electrically isolate the electrodes [60]. Supercapacitors can be categorized into two: electric double-layer capacitors (EDLC) and pseudocapacitors. Inside the EDLCs, energy is stored in a Helmholtz double layer as the separation of opposite charges at the surface of the electrodes. By virtue of high electrode surface area, EDLCs can yield a ~100-fold increase in energy density compared to regular electrolytic capacitors. Most of the EDLC electrodes consist of carbonaceous materials because of carbon's high conductivity and chemical stability, low thermal expansion coefficient, low cost and low density, and high surface area pertaining to some of its nano-allotropes [61]. Based on these unique features, different carbonaceous electrode materials have been utilized in EDLCs: carbon nanotubes, graphene, carbon quantum dots, nitrogen-doped carbons, and carbon nanofiber [61,62]. Pseudocapacitors, on the other hand, are

based on transition metal oxides, which are deposited onto the working electrode's surface and support reversible redox reactions at very high rates, thus exhibiting pseudocapacitance. Some examples of the pseudocapacitive materials are $V_2O_5$, $RuO_2$, $Fe_3O_4$, and $MnO_2$ [61]. Compared to EDLCs, they provide considerably higher gravimetric charge capacitance and better cyclic performance [61].

$MnO_2$-based pseudocapacitors are becoming more popular because of the abundance, thus cost-efficiency, and low toxicity of $MnO_2$. However, it suffers from low conductivity, and in order to exploit the most from its redox reactions, it must be coated (as a thin nano-film) on a highly conductive substrate. Therefore, carbonaceous structures, again, have been remarkably attractive in $MnO_2$-based supercapacitors; microfibrous carbon paper, graphene, activated carbon, microporous carbon, carbon aerogels, standard carbon black, and carbon nanotubes are some examples to carbonaceous electrodes [61]. Manganese dioxide is electrochemically operable in aqueous solution electrolytes such as KOH, KCl, $K_2SO_4$, and $Na_2SO_4$ [60]. Some of the other compatible electrolytes that have been successfully tested are tetraethylammonium tetrafluoroborate (TEABF4)/acetonitrile organic electrolyte, $H_3PO_4$/polyvinyl alcohol (PVA) solid electrolyte, and ([Bmim]PF6)/N, N-dimethylformamide ionic liquid electrolyte [63-65].

Application of the active material onto conductive electrode surface as a film can be carried out through conventional slurry technique where the mixture of metal oxide and conductive additives are applied onto aluminum foil with a binder [60], using chemical processes such as atomic layer deposition (ALD) and microwave irradiation [61], and cyclic voltammetry (CV) as electrodeposition [66].

The capacitance of a supercapacitor electrode can be calculated through running a CV scan first and calculating the half of the area (since charging and discharging processes include the same amount of charge transferred) of the CV curve, as shown in Figure 2.4. If the CV scan is performed at a fixed voltage scan rate ($\nu$), where

$$\nu = \frac{dV}{dt} \quad (2.7),$$

and between a potential window of $V_1$ to $V_2$, from times $t_i$ to $t_f$, the total charge ($Q_t$) transferred during the scan can be calculated as

$$Q_t = \int_{t_i}^{t_f} I\, dt = 2 \times \int_{V_1}^{V_2} I\, dV \times \frac{1}{\nu} \quad (2.8),$$

where $I$ is the current. Accordingly, the capacitance ($C$) of a supercapacitor electrode is

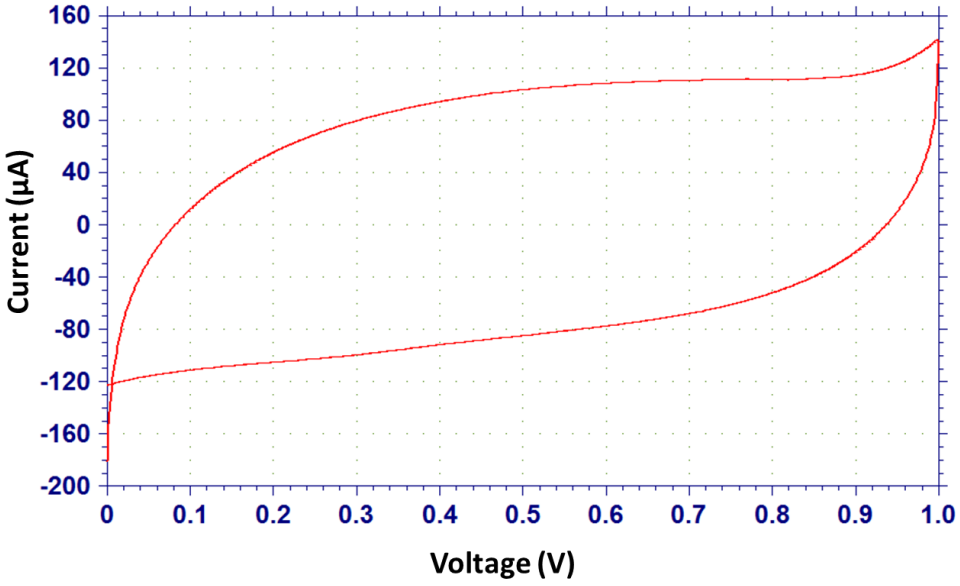


Figure 2.4 A nearly symmetric Cyclic Voltammetry scan behavior of a supercapacitor in a voltage window of 0 V - 1 V.

$$C(F) = \frac{1}{2} \times \left| \frac{Q_t}{V_2 - V_1} \right| = \frac{1}{2} \times \left| \int_{V_1}^{V_2} I \, dV \times \frac{1}{V_2 - V_1} \times \frac{1}{v} \right| \quad (2.9).$$

## 2.4. Photocapacitors

While efforts have been made to optimize DSSC's performance, the storage of the harvested energy has always been crucial, which otherwise limits its real-world application. Several reports have been published combining the DSSC and the energy storage electrodes into a single device using three-electrode (with two electrolytes) or two-electrode configurations [67-72]. Miyasaka et al. developed a photocapacitor consisting of a TCO coated glass with layers of dye-adsorbed $TiO_2$ particles with LiI coating and activated carbon (AC) as the photoanode while the counter electrode consisted of a Pt-coated glass with a layer of AC. Despite achieving a discharge capacitance of 0.69 F/cm$^2$, their device could not be charged above 0.5 V [67]. Murakami et al.'s photocapacitor consisted of a three-electrode system: dye-sensitized $TiO_2$/Pt DSSC with iodide-based electrolyte and two AC electrodes for the symmetric capacitor with TEABF4 in propylene carbonate as the electrolyte. Even with their well-separated photovoltaic and capacitive components, they were only able to charge up to 0.8V and had a limited energy density of only 47 μWh/cm$^2$ [68]. Zhang et al. designed a compact but costly photocapacitor made up of a dye-sensitized $TiO_2$ photoelectrode, and Pt/Au catalytic layers coated onto polyvinylidene fluoride (PVDF)/ZnO nanowires as counter electrode, mediated by a liquid electrolyte: 0.05 M LiI, 0.03 M $I_2$, 0.1 M guanidinium thiocyanate (GNCS), 1.0 M 1,3-dimethylimidazolium iodide (DMII), 0.5 M 4-tertbutyl pyridine (TBP) in 3-

methoxyproionitrile and acetonitrile (6:4). Although their open-circuit voltage ($V_{OC}$) was 0.8 V based on the J-V tests, however, they observed potentials less than 0.1 V at the onset of discharge [69]. Bagheri et al. also fabricated a three-electrode setup made of $TiO_2$ modified with LEG4 ((E)-3-(6-(4-(bis(2',4'-dibutoxy-[1,1'-biphenyl]-4-yl)amino)-phenyl)-4,4-dihexyl-4H cyclopental [1,2-b:3,4-b']dithiophen-2-yl)-2-cyanoacrylic acid) sensitizer as photoanode, conductive polymer layer (PEDOT) covered Ni-foil as photocathode, cobalt polypyridyl complex as solar cell electrolyte; and an asymmetric capacitor based on $Ni(Co)O_x$ and AC as positive and negative electrodes, respectively, together with KOH electrolyte. Their device was able to charge up to only 0.8 V under the exposure to sunlight, and when operated with the supercapacitor, it yielded only 10.2 $mF/cm^2$ [70]. Cohn et al.'s three-electrode photocapacitor consists of a carbon-terminated porous-Si wafer with a dye-sensitized $TiO_2$-based photoanode on one side to form the DSSC, and a similar wafer on the other side, to create the symmetric supercapacitor component. Two different electrolytes were employed in this design: $I^-/I_3^-$ redox electrolyte for the solar cell, and poly(ethylene-oxide)/1-ethyl-3-methylimidazolium tetrafluoroborate (PEO-EMIBF4) ionic polymer electrolyte for the supercapacitor. Their operational potential was less than 0.7 V and an accompanying discharge capacitance of only 3.5 $mF/cm^2$ [71]. Nuckowska et al. also designed a complicated and expensive three-electrode photocapacitor with an intermediate bipolar Ag film with D35 dye-sensitized $TiO_2$/FTO as photoanode on one side as the DSSC while a symmetric supercapacitor made of $RuO_x(OH)_y$ coated onto the Ag and FTO substrates, respectively, on the other side. Two different electrolytes were used for this

integrated device; poly-(3-hexylthiophene-2,5-diyl) (P3H4) conducting polymer electrolyte for the photovoltaic operation, and Nafion membrane as the solid electrolyte for the supercapacitor part. They were able to charge up to 0.9 V and extract 3.26 F/cm$^2$ of energy storage; however, the complexity and the cost of the components renders this approach impractical [72].

## 2.5. Batteries

A battery is an energy storage device which converts electrical energy into chemical energy during the charging step, and vice versa during the discharging stage. It operates through an electrochemical reduction-oxidation (redox) reaction between the active reactants that are separated by an ion-source electrolyte [73]. A simple electrochemical battery operation during discharge is shown in Figure 2.5: the electrons flow from anode to cathode through a circuit load (e.g., a light bulb), where the electrical energy of the battery is being consumed; inside the battery, the negatively charged anions and the positively charged cations move towards the anode and the cathode, respectively.

Based on the rechargeability, batteries are categorized into two: primary (non-rechargeable), and secondary (rechargeable) batteries. A primary battery does not have any reversible energy conversion mechanism and is therefore disposed of after the stored energy is drained. A secondary battery, however, has a reversible energy conversion mechanism because of its active materials on the electrodes and thus has attracted the main focus of battery research as a response to world's ever-increasing demand for advanced energy

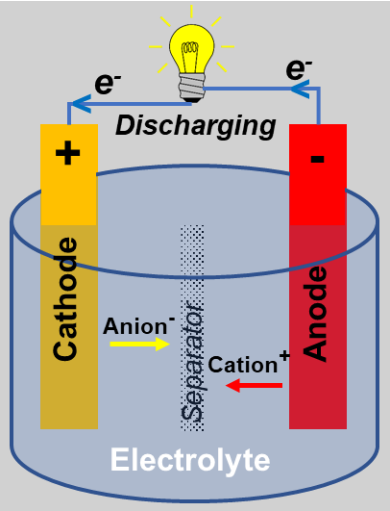


Figure 2.5 The operation of an electrochemical battery during discharge.

sources for electric vehicles (EVs), consumer electronic devices, and grid services [73].

Independent of its size and shape, a battery can be replicated by its most fundamental unit: electrochemical cell, or cell [73]. In a battery cell, active reactants are attached to conductive substrates, constituting a battery electrode: anode or cathode. In addition, a cell has an electrolyte and a separator, which can be optional depending on the setup. During the cell charging, a reduction reaction occurs at the anode, absorbing electrons coming from the external voltage source, and charge carriers migrating from the cathode to the anode through electrolyte and separator; oxidation reaction occurs at the cathode, releasing electrons. During discharge, these reactions are reversed and forced by the chemical-potential difference between two electrodes: oxidation at the anode releases electrons that flow through the load circuit and reach the cathode, contributing to reduction reaction; charge carriers also migrate toward the

cathode [73]. The discharge current is the flow of electrons from the anode to the cathode through the external load, which is being balanced by the ionic current between anode and cathode. Rechargeable batteries can be fabricated using different material combinations in their constituting parts.

Lead-acid batteries, the oldest well-known rechargeable batteries first developed in 1859 by Gaston Planté, rely on the transformation of lead (Pb) anode and lead oxide ($PbO_2$) cathode into lead sulfate ($PbSO_4$) during discharge, and vice versa during charging; accompanied with sulfuric acid electrolyte ($H_2SO_4$) [74]. Pb-acid batteries are well established and economical, therefore widespread in small-to-large scale systems: backup UPS devices for electronics, ignition starters for automobiles, and large-scale renewable power plants' energy storage system [74,75]. They also favor high recyclability (over 98%) of their components, from Pb-based electrodes to electrolytes [74]. There are two different designs for Pb-acid batteries: classic flooded design, where electrodes are vertically dipped into an excess amount of electrolyte solution; sealed design, where less amount of electrolyte is fixated in between the electrodes [74]. The flooded design suffers from high maintenance requirement of electrolyte since it stratifies and evaporates over time [74]. Nonuniform distribution of electrolyte concentration on the electrodes also causes uneven utilization of the active materials, which reduces the cycle life of the batteries. Sealed Pb-acid battery, on the other hand, has a more secure electrolyte use and is operable in different orientations, but suffer from the gassing reactions inherent to the battery's charge-discharge operations, and thus requires a gas exhaust. Besides, additional concerns arise for thermal safety in dense packaging [74]. In general,

although Pb-acid batteries benefit from low cost and ease of fabrication, design restrictions and toxic electrolyte have made them inapplicable to very small-scale portable systems such as smartphones and tablet PCs.

Nickel-based batteries, mostly dominated by nickel-cadmium (Ni-Cd), nickel-iron (Ni-Fe), nickel-zinc (Ni-Zn), nickel-metal hydride (Ni-MH), and nickel-hydrogen (Ni-$H_2$) batteries, are based on nickel oxide hydroxide (NiOOH) positive electrode [76]. Among these, Ni-Cd and Ni-MH batteries, akin to each other in design, were dominant in the industry of portable electronics such as cell phones and computers, before the onset of lithium-ion batteries. For example, one of the first hybrid electric vehicles (HEV), Toyota's Prius, has employed Ni-MH batteries as its energy storage unit [76]. A Ni-MH battery uses a hydrogen-absorbing alloy as an anode, which oxidizes to metal alloy when discharging; the battery is environmentally safe, durable under various temperatures and other harsh conditions, has high capacity and recently-improved cycle life [76]. These features have made them attractive for portable power sources and electronics. Ni-Cd batteries, on the other hand, use Cd anode, which is highly toxic, but have high-power discharge capability, good performance at low temperatures, and excellent cyclability. They were mostly used in portable and standby power sources. Both Ni-MH and Ni-Cd batteries, however, lack of energy density and cycle life, compared to lithium-ion batteries [76].

Nickel-hydrogen batteries, possessing excellent cycle life, high-power, high-specific energy density, and overcharge tolerance, found a place in space applications like satellites. Nonetheless, their low volumetric energy density, high self-discharge, and high cost are limiting their use inside other applications. The

newer Ni-based batteries are Ni-Fe and Ni-Zn batteries, which are less popular. Although Ni-Fe batteries are robust, environmentally safe, with high cyclability, their low energy, power density, and high self-discharge have limited their use to mining and recently, in renewable energy plants [76]. Ni-Zn batteries' high practical gravimetric energy (~140 Wh/kg) and environmental safety have made them a competitor to Pb-acid and Li-ion batteries, according to researchers [77]. However, the inherent feature of the Zn dendrite growth during cycling, which causes shorting of the electrodes and hence thermal runaway, is raising safety concerns and decreasing the battery life, which pushes scientists to quest for a stable design for Ni-Zn batteries [76,77].

Molten salt batteries are based on molten salt electrodes and electrolytes, which operate at a high range of temperatures (from 90$^{o}$C to 375 $^{o}$C) depending on the material [78,79]. They can have high power and energy densities and are usually preferred in medium to large-scale energy storage systems [78]. The reason these batteries operate at high temperatures is that of the high melting point of the salts they use, but it raises concerns about the material durability. If only the electrodes are made of molten salts, an electrically separating, physically strong solid electrolyte with high ionic conductivity and electrochemical stability, must be employed [78]. For this sake, β-Alumina, benefiting from high ionic conductivity and utilized along with a $K^+$, $Li^+$, $Ag^+$, $Pb^{2+}$, $Ba^{2+}$, $Sr^{2+}$, or especially $Na^+$ (for its highest ionic conductivity in β-Alumina) ion providing anode, has been the most suitable solid electrolyte developed so far [78]. There are two classes of sodium-β-alumina (NBBs): sodium-metal halide (ZEBRA)

batteries, using a semisolid cathode with a mixture of transition metal halides and molten salt; sodium-sulfur (Na-S) batteries, using molten-sulfur cathode [78].

First invented in 1968 to use in electric vehicles by the Ford Motor Company, Na-S batteries have found interest in the market by their high theoretical gravimetric energy (~760 Wh/kg), high coulombic efficiency, good cyclability, and are economical. Nevertheless, the instability of the battery due to corrosive polysulfide melts is a big problem and paused Na-S batteries' development in the 1990s, with the introduction of Li-ion and Ni-based batteries. More stable operation of ZEBRA batteries with the use of less corrosive materials, ease of fabrication, higher voltage, and the lower operating temperature has made them be preferred over Na-S batteries [78]. On the other hand, their most significant disadvantage is the low energy density (~260 Wh/kg).

Lithium-air (Li-air) batteries, carrying a different design than regular batteries, offer extremely high theoretical gravimetric energies, even 3-4 times higher than Li-ion batteries [80]. They are based on oxygen ($O_2$) as the reactant, which is stored outside the cell in a tank and flown onto $O_2$-breathing porous electrodes; Li metal anode; a Li-conducting electrolyte. The redox reaction

$$2Li^+ + O_2 + 2e^- \leftrightarrow Li_2O_2 \quad (2.10)$$

takes places inside the electrodes at 2.96 V vs. $Li/Li^+$ [80]. In order to obtain a pure reaction, filtering the air off any moisture and other gases is crucial. Based on the selection of the electrolyte materials, there are four different types of Li-air batteries: non-aqueous, aqueous, hybrid, and solid-state Li-air batteries, as shown in Figure 2.6 [81]. Among these, non-aqueous Li-air batteries, with the advantage of using the bare Li metal anode, have been the most popular [80].

Considerable research has been going on to improve their specific energy density, low durability, and low efficiencies [80].

Aluminum (Al)-ion batteries are recently gaining popularity due to their low-cost fabrication, high theoretical capacity (2.98 Ah/g for Al anode; 400 Ah/kg for Al-λ-$Mn_2O_4$ battery), no solid electrolyte interphase (SEI) formation, and the ease of fabrication with using Al for both the casing and the anode [82]. In order to be a competitor to Li-ion batteries, Al-ion battery technology must evolve to allow rechargeability, high discharge capacities, and power.

Flow batteries, which allow fast recharging by the continuous flow of anolytes and catholytes into the system with long durability, have low specific

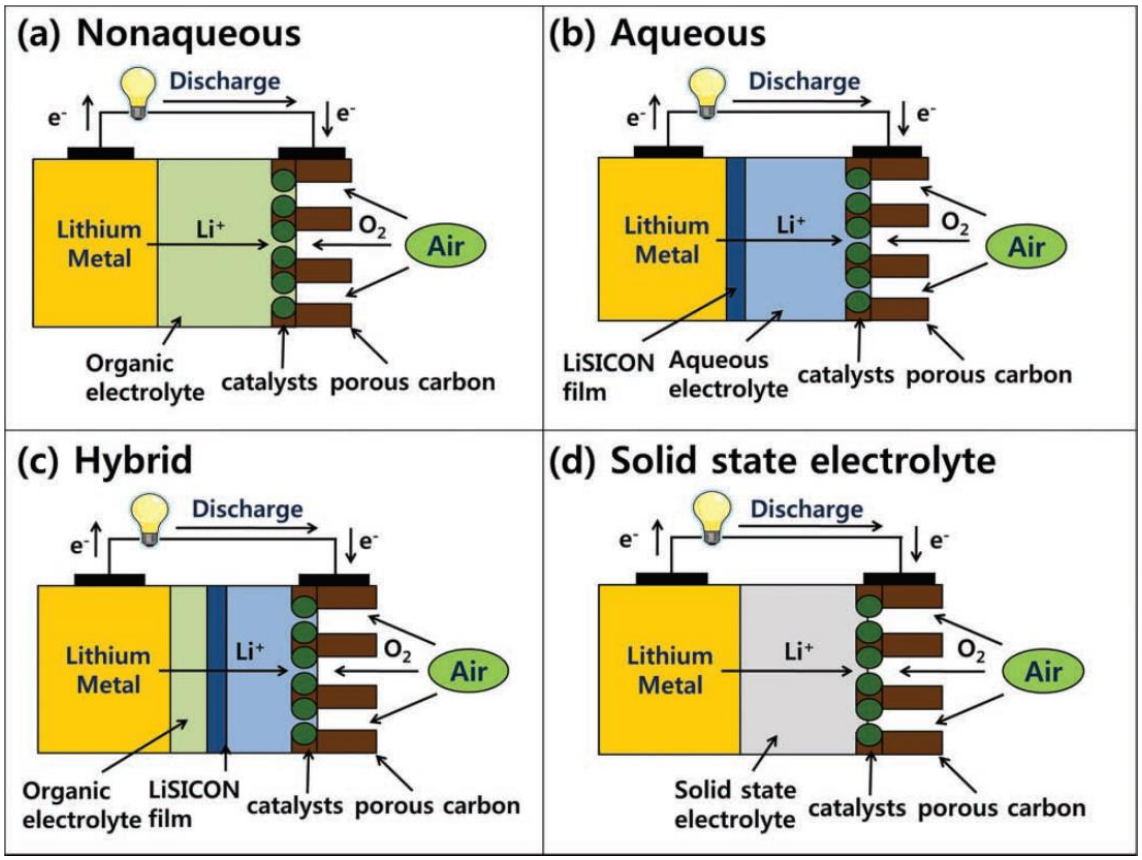


Figure 2.6 Schematic representations of the most popular four Li-air batteries [81].

energy and a low discharge voltage (< 2 V) compared to Li-ion batteries [83,84].

### 2.5.1. Lithium-Based Batteries

Lithium-based batteries, since the invention of the lithium battery by Whittingham in 1976, have been well established, and currently dominate the battery market [85]. Lithium is the lightest and a very reactive metal with an atomic mass of 6.94. It has, therefore, a high theoretical gravimetric capacity (3829 mAh/g), making it attractive to be employed as a metallic anode for rechargeable batteries [86]. However, after charge-discharge cycles, Li metal forms dendrites on the surface which can penetrate through the electrolyte and separator, causing shorts with the cathode, and thus a huge thermal runaway. Therefore, today, Li metal is only being used in Li-batteries, which are primary batteries, and the Li-ions only intercalate into the cathode host structure during the one-time discharge, raising no safety issues. For the rechargeable Li-ion batteries, lithium metal had to be replaced with the lithium intercalation anodes, on which the lithium dendrite formation is reduced. Graphite intercalation compound (GIC) $LiC_6$ has been the most popular intercalation anode because of its low cost and its ability to further impede faradaic reactions with the organic solvents of the electrolytes that formed a protective SEI layer coating onto the carbon particles [86]. Most of the SEI layer forms on the graphite anode in the first full cycle, due to its electrochemical potential being higher than the electrolyte's LUMO, and is still developed in the following cycles at a gradually decreasing rate; it allows the penetration of Li-ions and protects the electrolyte from further decomposition as well as the Li-ions' consumption, but, is a resistive layer [87]. In addition, an SEI-

like layer develops on the cathode, too, at high potentials after the oxidation of electrolytes, due to cathode's electrochemical potential being lower than the electrolyte's highest occupied molecular orbital (HOMO), but has less effect on the performance [87]. Commonly used electrolytes are carbonate-based ones, for their stability, and they consist of a lithium salt ($LiPF_6$, $LiBF_4$, $LiClO_4$, lithium bis(trifluoromethanesulfonyl)imide (LiTFSI)) dissolved in a mixture of solvents (ethylene carbonate(EC)+dimethyl carbonate(DMC), EC+ethymethyl carbonate (EMC), or EC+diethyl carbonate(DEC)) with high dielectric permittivity and low viscosity [86,88]. Other popular electrolytes are solid-polymer and polymer-gel based ones used for the flexibility and safety of the Li-ion batteries, also called lithium-polymer batteries [88]. The operation of a Li-ion battery during charging and discharging is shown in Figure 2.7. At the charging step, Li ions deintercalate from the cathode material, and diffuse toward and intercalate into the anode. During discharge, Li ions intercalate into the cathode while some of them also deintercalate from the anode; these reactions are supported by the flow of electrons from the anode to the cathode through a circuit load until the equilibrium state is reached.

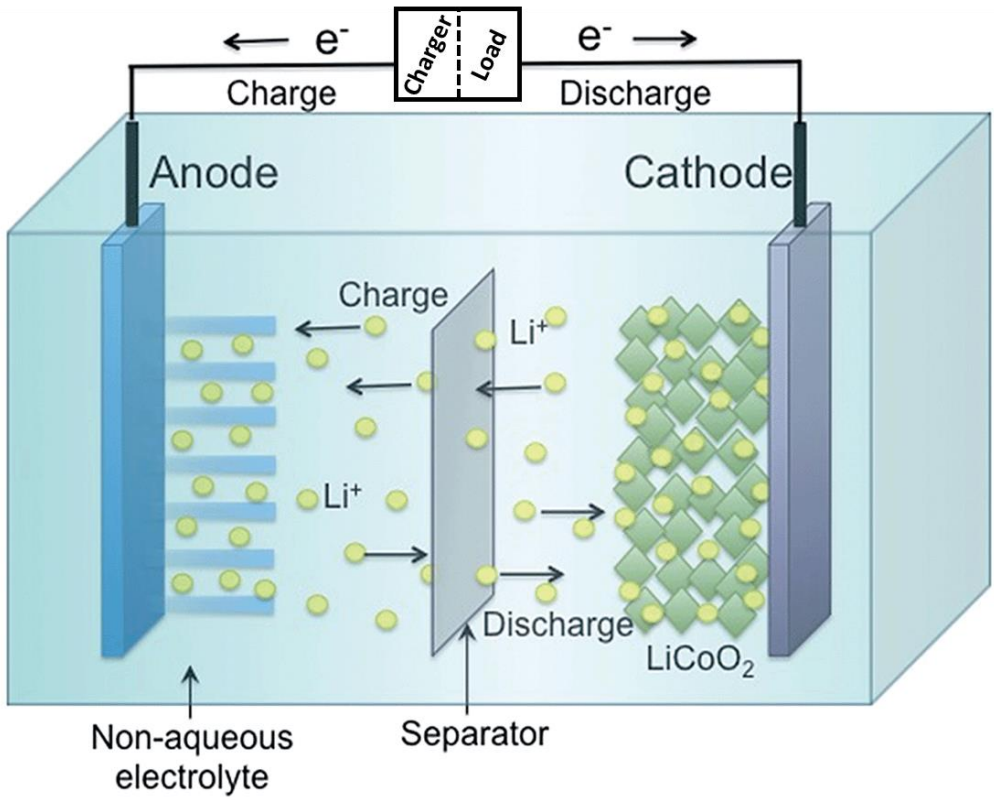


Figure 2.7 Schematic representation of a rechargeable Li-ion battery cell with a liquid electrolyte, illustrating the lithium intercalation-deintercalation mechanism during charging and discharging [89].

### *2.5.1.1 Li-Ion Battery Cathodes*

Among many other materials such as anode, electrolyte, and separator, the most crucial part of a Li-ion battery is its cathode. After the work of Whittingham et al. on Li-ion's intercalation into cathodic $TiS_2$ in 1975, researchers have been focusing on developing different lithium intercalation cathode materials [86]. The most common LIB cathode materials are the lithium transition metal oxides and polyanion ($MO_4^{c-}$, where M = Si or P, and c = 4 or 3, respectively) based materials, all of which contain lithium as the charge carrier and a transition metal (Co, Fe, Mn, and Ni) as the valence electron provider for

the redox reactions happening during the lithium intercalation/deintercalation reactions. The number of Li-ions inserted into the cathode material per unit mass during discharge determines the specific capacity of the cathode, hence the total energy of the battery. The potential at which Li-ions intercalate into the cathode material is the operational voltage of the Li-ion battery. The rate of Li ions' intercalation into the cathode material determines the power of the battery. The soundness of the cathode material after the charge (Li-deintercalation) and discharge (Li-intercalation) determines the battery's cycle life. Some of the most attractive Li-ion battery cathode materials developed so far are $LiCoO_2$, $LiMn_2O_4$, $LiNi_xCo_yAl_zO_2$ ($x + y + z = 1$), $LiNiCoMnO_2$ as transition metal oxides, and $LiFePO_4$ as a polyanion-based material [86]. In Table 2.1, their operation potential, specific capacity, specific energy, and structure are tabulated [86]. Figure 2.8 also shows these cathodes' crystal structures, in which Li ions are represented as spheres: $LiCoO_2$ with the octahedrally ordered Li-ions and $CoO_6$ octahedra; $LiMn_2O_4$ with the tetrahedrally ordered Li-ions and $MnO_6$ octahedra; $LiFePO_4$ with the octahedrally coordinated Li-ions and $PO_4$ and $FeO_6$ as tetrahedra and

Table 2.1 Commercially available lithium-ion battery cathode materials and their attributes [86].

| **Material** | **Structure** | **Potential vs. Li/Li+, average V** | **Specific Capacity, mAh/g** | **Specific Energy, Wh/kg** |
|---|---|---|---|---|
| $LiCoO_2$ | layered | 3.9 | 140 | 546 |
| $LiNi_{0.8}Co_{0.15}Al_{0.05}O_2$ (NCA) | layered | 3.8 | 180-200 | 680-760 |
| $LiNi_{1/3}Co_{1/3}Mn_{1/3}O_2$ (NMC) | layered | 3.8 | 160-170 | 610-650 |
| $LiMn_2O_4$ and variants (LMO) | spinel | 4.1 | 100-120 | 410-492 |
| $LiFePO_4$ (LFP) | olivine | 3.45 | 150-170 | 518-587 |

octahedra, in order [86]. Among these popular cathode materials, $LiFePO_4$ has been the most attractive in EVs, HEVs, and different electronic applications, due to its high safety and stability, good operating voltage (3.4 V vs. $Li^+/Li$), and adequate specific discharge capacity (170 mAh/g) [90].

The energy diagram of a Li-ion battery at open-circuit is shown in Figure 2.9. From this diagram, the open-circuit voltage ($V_{OC}$) can be derived as:

$$q\,V_{OC} = \bar{\mu}_{e^-}^{a} - \bar{\mu}_{e^-}^{c} \leq E_g \qquad (2.11),$$

where $q$ is the magnitude of an electron's electric charge, $E_g$ is the energy window of the electrolyte, which lays between the energy levels of LUMO and HOMO; $\bar{\mu}_{e^-}^{c}$ and $\bar{\mu}_{e^-}^{a}$ are the Fermi energies (eV) of the cathode and anode, consecutively [91]. For the stable operation of the battery electrolyte, its potential window must be bigger than or equal to the operation potential of the battery.

The theoretical capacity ($C_t$) of the cathode material is calculated as follows:

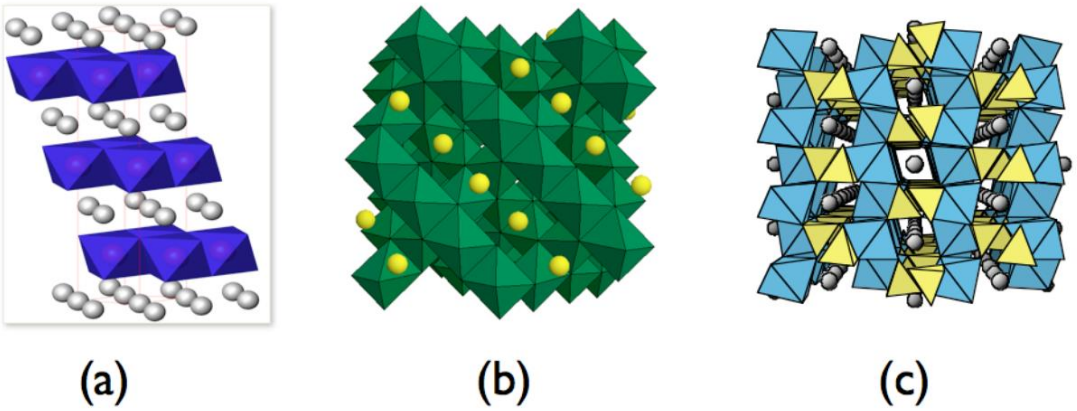


Figure 2.8 Schematic crystal structures of the cathode materials (a) $LiCoO_2$, (b) $LiMn_2O_4$, and (c) $LiFePO_4$ [86].

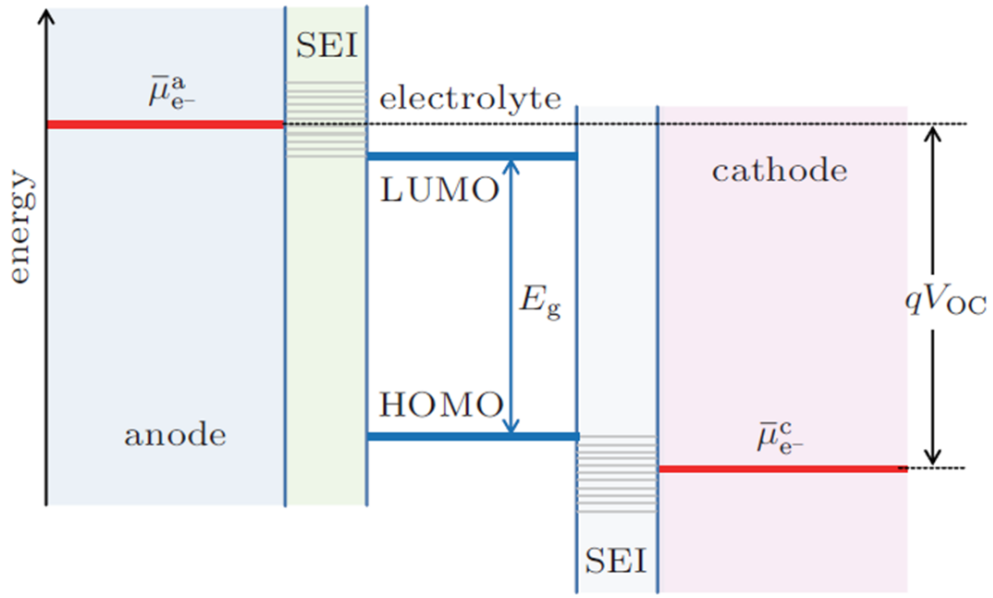


Figure 2.9 Energy band diagram of a lithium-ion battery at open-circuit. Both anode and cathode have SEI layers. $E_g$ is the electrolyte's potential window at thermodynamic equilibrium. $V_{OC}$ is the open-circuit potential of the battery. $\bar{\mu}^{c}_{e^-}$ and $\bar{\mu}^{a}_{e^-}$ are the electrochemical potential of the anode and cathode, respectively [91].

$$C_t = \frac{n\,F}{3.6 \times M} \qquad (2.12),$$

where $n$ is the number of electrons that go into reaction per formula unit, $F$ is the Faraday constant, and $M$ is the molar mass of the material [92]. Based on this formula, increasing the number of reactive electrons, or the number of Li ions available in the unit formula, and reducing $M$, are essential for having a higher specific capacity. For this reason, scientists have been on a quest for employing more than one Li atom per formula unit in the novel cathode materials: $Li_2MSiO_4$ (M = Fe, Mn, Co, or combination of these, with a theoretical capacity of ~331 mAh/g), and recently developed $Li_3Mo_4P_5O_{24}$ (with a theoretical capacity of 198 mAh/g) are some examples.

In some cases, adding different metal(s) into the cathode host structure, while maintaining the total metal's stoichiometric ratio and the unit crystal structure, might be beneficial in utilizing most of the Li-ions available in the structure. As a result, a higher amount of usable energy and high-power can be obtained, with the help of new high-voltage plateaus at which Li-ion extraction/insertion occurs corresponding to the added metal's redox couples, during charging and discharge. For example, $LiMn_2O_4$ and $LiNi_{0.5}MnO_4$ operate at 4.1 V and ~4.7 V, respectively; the potential difference arises from $Ni^{2+}/Ni^{3+}$ and $Ni^{3+}/Ni^{4+}$ redox couples' Li extraction/insertion mechanism from 4.6 V to 4.8 V [86,93]. In the case of $Li_2MSiO_4$, where M can be Fe, Ni, Co, etc., Dompablo et al. calculated different Li deintercalation voltages based on the oxidation states, as shown in Figure 2.10 [94]. It is clear that employing different transition metals,

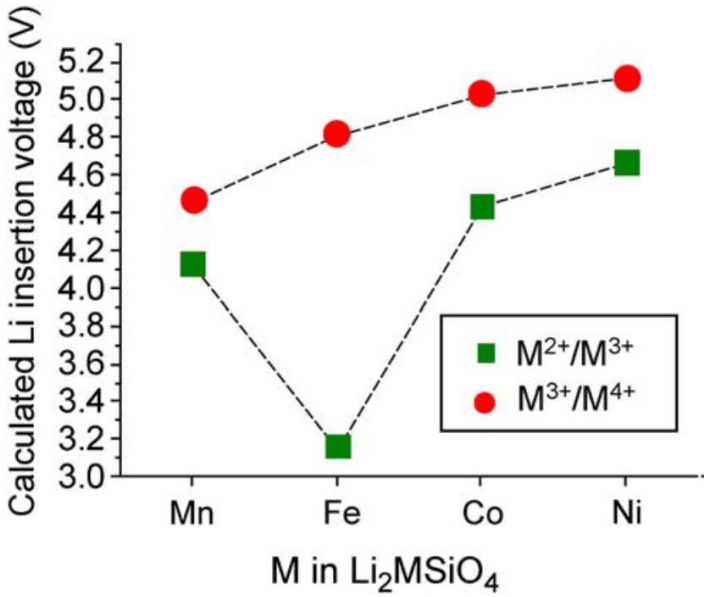


Figure 2.10 Lithium deintercalation voltages of the reactions $Li_2MSiO_4 \leftrightarrow LiMSiO_4 + Li$ (green squares) and $LiMSiO_4 \leftrightarrow MSiO_4 + Li$ (red circles); where M can be Mn, Fe, Co or Ni [94].

dilithium ternary silicate (DTS) cathode can operate at voltages close to or higher than 5 V.

There are different cathode material synthesis methods, as shown in Figure 2.11: sol-gel, solvothermal process, hydrothermal process, mechanochemical process, combustion process, spray pyrolysis, emulsion-drying, co-precipitation, and solid-state synthesis are some methods [95]. Among

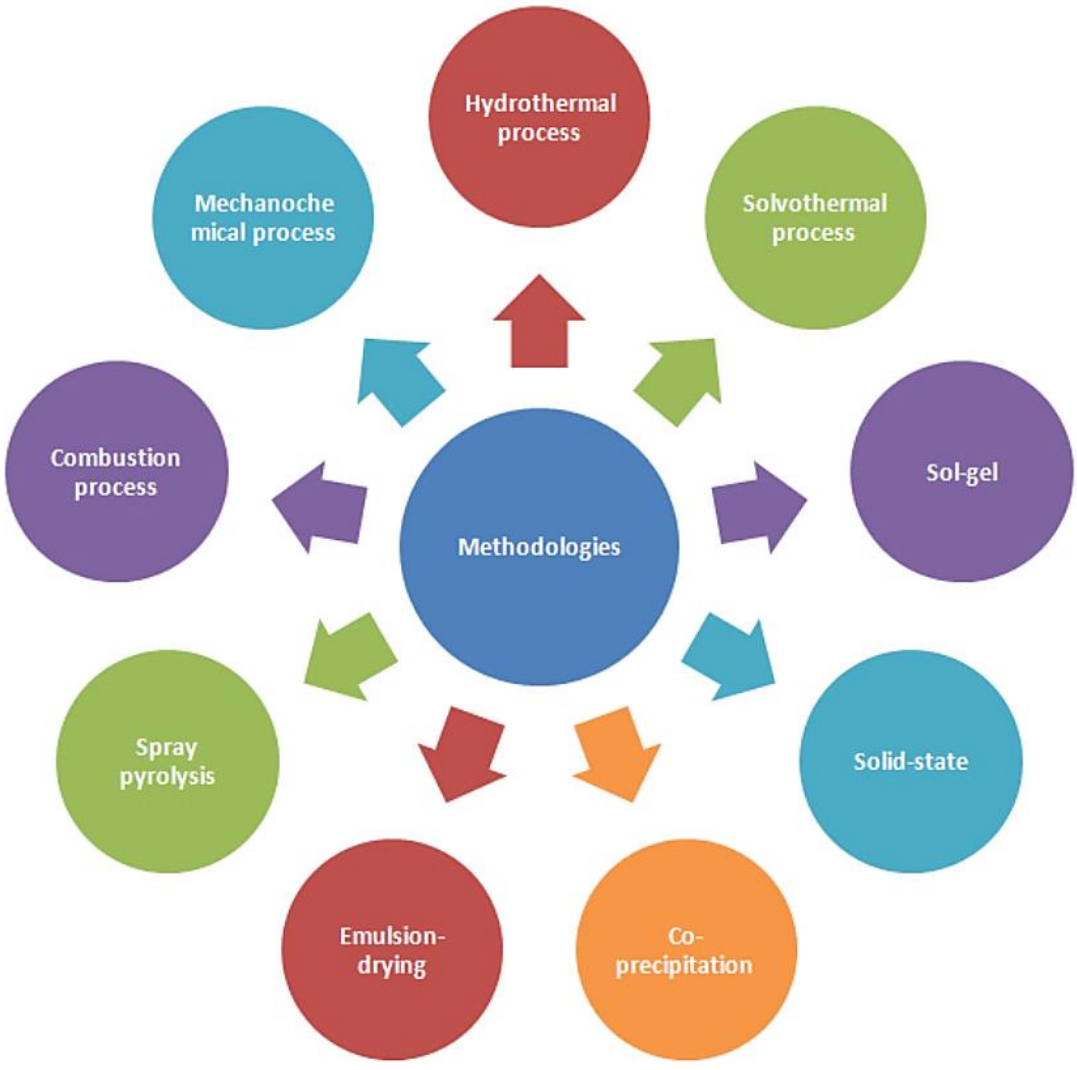


Figure 2.11 Common synthesis methods for the fabrication of cathode materials [95].

these, hydrothermal synthesis, spray pyrolysis, and especially sol-gel synthesis have been more widespread for synthesizing nanosized materials due to their low-temperature requirement [96]. During a battery material synthesis, achieving high purity, controllable crystallinity, and uniform size distribution, are crucial for high-power applications, as well as cyclability [96]. According to Shen et al., nanosized crystallites have shorter $Li^+$ solid-state diffusion distance, and hence more ionic conductance; fewer point defects; increased the contact area between the electrolyte and electrode, thus resulting in a better rate capability [96].

The structural characterization of the synthesized crystalline cathode material is carried out through X-ray diffraction (XRD) analysis. A crystalline material consists of repeating arrangements of unit cells, each containing the smallest number of atoms spatially arranged in a material-specific orientation. A unit cell's symmetric repetition in three-dimensions builds up the crystal of the material, which also extends long distances three-dimensionally, forming the material. When a solid material is exposed to incident light (X-rays) with a wavelength comparable to the interatomic spacings of its crystal, the light diffracts as a result of elastic scattering [97]. As shown in Figure 2.12, if two parallel rays hit two parallel planes (separated by the distance *d*) of the crystal with an angle of incidence *Θ,* the diffracted beams are constructive only if the equation

$$2\,d\sin\theta = n\,\lambda \qquad (2.13),$$

where *n* is a positive integer, is satisfied, as per the Bragg's Law [97]. Therefore, crystals with precise three-dimensional periodicities have intense and sharp diffraction peaks [97]. If a sample is illuminated with X-rays through a wide range of incident angles, the sample's crystal structure yields constructive interference at

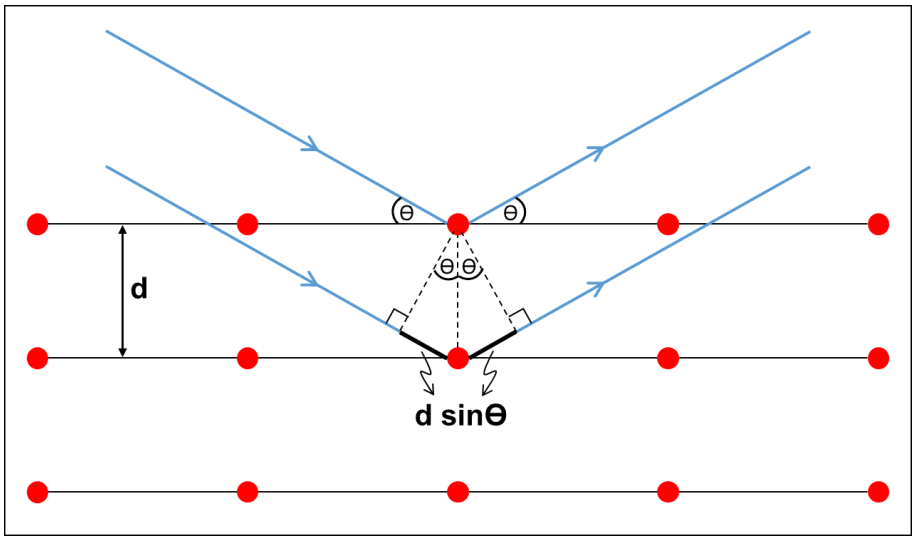


Figure 2.12 Constructive interference of two parallel X-rays after hitting to the atoms of a material's crystal planes (having a distance *d* in between) with an incident angle *Θ*, satisfying Bragg's Law. The red dots denote atoms of the crystal plane.

different incident angles, each corresponding to a different interplanar spacing *d* [97]. The resulting X-ray diffraction spectrum has many strong diffraction peaks at these incident angles, which are material-specific.

### *2.5.1.2 Utilization of the Cathode Materials*

Even though a good crystal structure was obtained, underutilization of the cathode material by the intercalation/deintercalation of $Li^+$ ions is very common due to the inherent low ionic and electronic conductivities [98]. Some of the cathode materials' conductivities are listed in Table 2.2, and it is evident that the popular cathode materials $LiCoO_2$, $LiMn_2O_4$, and $LiFePO_4$ suffer from low electronic conductivity, which limits their performance at high current rates [99]. Among these cathode materials, $LiFePO_4$ (LFP) has the lowest conductivity and

Table 2.2 Resistivity of the commonly used materials in a Li-ion battery cell [99].

| **Cell Component** | **Material** | **Band Gap (eV)** | **Electrical Conductivity (S $cm^{-1}$)** |
|---|---|---|---|
| Current Collector (anode) | Copper (C11000) | 0 | $5.8\times10^{5}$ |
| Current Collector (cathode) | Aluminum (1100) | 0 | $3.4\times10^{5}$ |
| Anode | Graphite | 0 | $(2\text{-}1)\times10^{3}$ |
| Cathodes | $LiCoO_2$<br>$LiMn_2O_4$<br>$LiFePO_4$ | 0.5-2.7<br>0.28-2.20<br>0.3-1.0 | $\sim10^{-4}$<br>$\sim10^{-6}$<br>$\sim10^{-9}$ |

slow lithium diffusion, which reduce its electrochemical performance and makes approaching its theoretical specific capacity (170 mAh/g) very challenging [100]. Scientists have tried several methods to overcome this problem as well as to attain a higher rate capability. Chung's group attempted to dope LFP with different cations ($Mg^{2+}$, $Al^{3+}$, $Ti^{4+}$, $Zr^{4+}$, $Nb^{5+}$, and $W^{6+}$) and observed up to ~$10^{8}$-fold increment in its conductivity; the doped LFP was able to reach ~86 mAh/g discharge capacity at 10.8 C. Ni et al. doped LFP with manganese (Mg) to enhance its electrical conductivity [102]. Although their cathode material exhibited a steady charge-discharge performance over 40 cycles, it only achieved a discharge capacity of 156 mAh/g at a current density of 17mA/g. Besides, Chen's group developed a vanadium (V)-doped LFP material through a quasi sol-gel process [103]. They claim that V-doping is beneficial for the lattice distortion and enhanced Li-diffusion, better conductivity, and smaller particle size; hence, the

high-power operation of the LFP. Their cathode material achieved a discharge capacity of only 150.4 mAh/g at a C-rate of 0.1 C, which is lower than that of their undoped LFP's capacity (156.6 mAh/g), and 105.8 mAh/g at a C-rate of 20 C. Alternatively, scientists have tried to coat LFP with carbon in situ of the synthesis [104-106]. Choi and Kumta developed a surfactant-based sol-gel technique to fabricate LFP nanomaterials with a high surface area, and they coated their LFP material with carbon black, afterward [104]. After the charge-discharge tests, their cathode yielded specific discharge capacities of 123 mAh/g and 157 mAh/g at the current rates of 10 C and 1 C, respectively. Bao et al. coated the LFP particles with carbon using P123, the triblock copolymer of poly (ethylene oxide)-poly (propylene oxide)-poly (ethylene oxide) [106]. After the cathode material was cast onto an aluminum (Al) foil with acetylene black as the additional carbon source and polyvinylidene fluoride (PVDF) as the binder, its charge-discharge performance was tested in a LIB cell. At the current rates of 0.05 C and 10 C, their cathode showed discharge capacities of 166 mAh/g and 50 mAh/g, respectively. Scientists have also aimed at increasing the conductivity of their LFP material via carbon coating it post-synthesis [107-109]. Tian et al., after coating their LFP nanorods with carbon using solid glucose, obtained a specific discharge capacity of ~130 mAh/g at the current rate of 10 C [107]. Different carbonaceous nanostructures such as graphene [90,110,111], carbon nanotubes [112-114], and carbon fibers [115,116] have also been used to coat the cathode materials for a high-rate capability.

In those as mentioned earlier and many other studies, Li-ion cells were fabricated through a conventional method: preparing a paste consisting of active

cathode material, dissolved binder and an additional conductive additive such as carbon black, then blade-casting it onto an electrically conductive substrate. However, this method has many drawbacks. Firstly, binders occlude the surface of active materials, hence drop the material conductivity as well as reduce the gravimetric capacity [117,118]. Secondly, as a popular binder, polyvinylidene fluoride (PVDF), for example, has inadequate flexibility and therefore cannot endure contraction and expansion stresses during the charge and discharge of a battery, and causes the bond between the active cathode material, carbon material, and current collector to be weakened or lost over time [119]. Thirdly, N-methyl pyrrolidone (NMP) solvent, which is used with PVDF is expensive, highly toxic, and flammable, even though it is evaporated and not present in the final electrode structure [120]. Fourthly, it is a well-known fact that binders can contribute to thermal runaway reactions in LIBs [121].

There have been many studies aiming at eliminating the use of binders in LIB cathodes. Zeng et al. used liquid phase deposition of $V_2O_5$ nanosheet thin film, with a thickness of 300-350 nm as a binder and carbon-free cathode, demonstrating that a thicker material deposition has led to a less conductive network [122]. Lalia's group grew carbon nanotubes on fiber substrates and incorporated $LiFePO_4$ particles into this structure to produce a binder-free cathode [123]. However, their specific discharge capacity was very low (107 mAh/g at C/5), possibly due to poor charge transfer kinetics because of large $LiFePO_4$ particles. Sreelakshmi et al. synthesized hybrid composites of $LiMn_2O_4$/graphene without binder, using electrophoretic deposition [124]. They obtained a specific capacity of 49 mAh/g, which is much smaller than the theoretical capacity (296

mAh/g) of $LiMn_2O_4$, possibly due to the high internal resistance of the structure and consequently a high *IxR* drop during discharge. Huang et al., on the other hand, developed a binder-free, efficient cathode material by electrophoretically coating $LiFePO_4$/graphene oxide onto a carbon cloth, which required annealing of the structure at a high temperature (700 $^oC$) to reduce the graphene, as an extra fabrication step [125]. Liu's group, on the other hand, fabricated an LFP cathode through in-situ gelatin carbonation and using acetylene black as the conductive additive. Their cathode yielded a specific discharge capacity of ~109 mAh/g at a current rate of 5C [126].

### 2.5.2. AC Impedance Spectroscopy

AC impedance spectroscopy, or electrochemical impedance spectroscopy (EIS), is a technique used for characterizing the equivalent circuit of an electrochemical system. It allows one to identify the impedance of each component that resists/affects the charge carriers between the electrodes of the system. In a typical two-electrode electrochemical cell, under equilibrium, two opposing forces balance each other: migration of the anions/cations in between the electrodes due to the potential difference, and diffusion of the ions at the electrode surface due to a change in the concentration gradient, as depicted in Figure 2.13 [127]. When an AC voltage signal is applied between the electrodes, the output current will be either in or out of phase with the input voltage. By identifying the phase shift in a range of frequencies, it can be understood if the circuit component is resistive, capacitive, inductive, or any combination of these. For example, under the steady-state condition, a double-layer forms on an

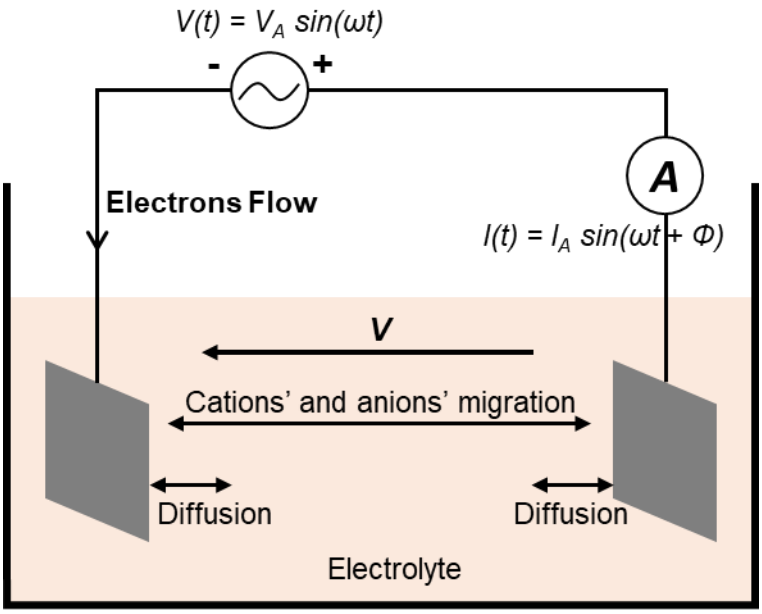


Figure 2.13 An electrochemical system with two electrodes separated by an electrolyte, and under steady-state condition. If a sinusoidal voltage "$V(t) = V_A \sin(\omega t)$" is applied to the system, the current response will be out of phase with the input voltage by $\Phi$ [127].

electrode's surface. Diffusion of the ions at the electrode's surface, accompanied with the charge transfer, thus creating a double-layer between the inner and outer Helmholtz layers, is equivalent to a resistor in parallel with a capacitor, whose impedance is

$$Z_{eq} = \left(\frac{1}{R} + j\omega C\right)^{-1} = \frac{R}{1+j\omega CR} \quad (3.2),$$

where $\omega$ is angular frequency. The Nyquist plot of this circuit is also illustrated in Figure 2.14.

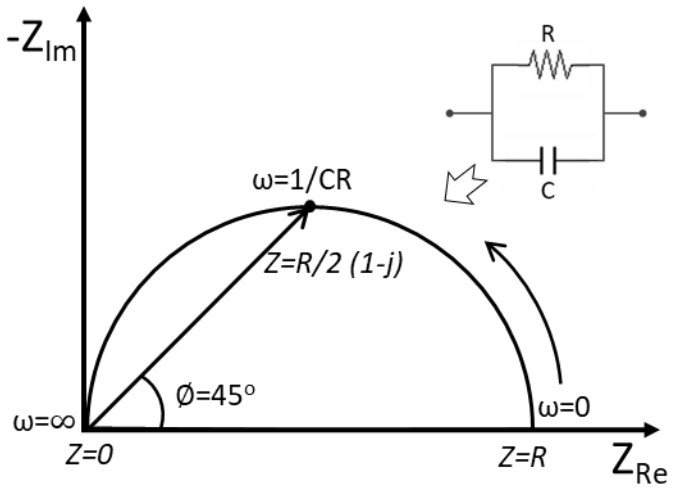


Figure 2.14 Nyquist plot of an R-C parallel circuit in the angular frequency range of $\omega = 0$ to $\infty$ rad/s.

# CHAPTER III

# CARBON NANOTUBE-BASED CATHODES FOR SOLAR ENERGY HARVESTING WITH DYE-SENSITIZED SOLAR CELLS

This chapter elucidates the work done to fabricate DSSCs with Pt-alternative planar CNT (P-CNT) and micro-array CNT (MA-CNT) counter electrodes (cathodes) and analyze their photovoltaic characteristics. Conventional UV photolithography and a simple lift-off process were employed to micropattern the buffer and catalyst layers on highly-doped n-type Si substrates. Both P-CNTs and MA-CNTs were grown on Si substrates in an HFCVD system. Photoanodes were made of titanium dioxide ($TiO_2$) films spin-coated onto FTO glass substrates and sensitized with an N-719 dye. An iodide-based electrolyte was also utilized in the DSSCs. Photovoltaic tests of the cells were conducted at 1 sun of AM 1.5 G illumination intensity, and the performance of VACNTs in planar and micropatterned configurations was scrutinized.

## 3.1. Micropatterning and Synthesis of Carbon Nanotubes

Before synthesizing MA-CNTs, Si substrates were micropatterned through a lift-off process. Figure 3.1 delineates the schematic flow chart for the fabrication of MA-CNT electrodes. Rectangular (2x1 $cm^2$) cut Si substrates were first cleaned with acetone and methanol, followed by drying on a 100 $^oC$ hot plate.

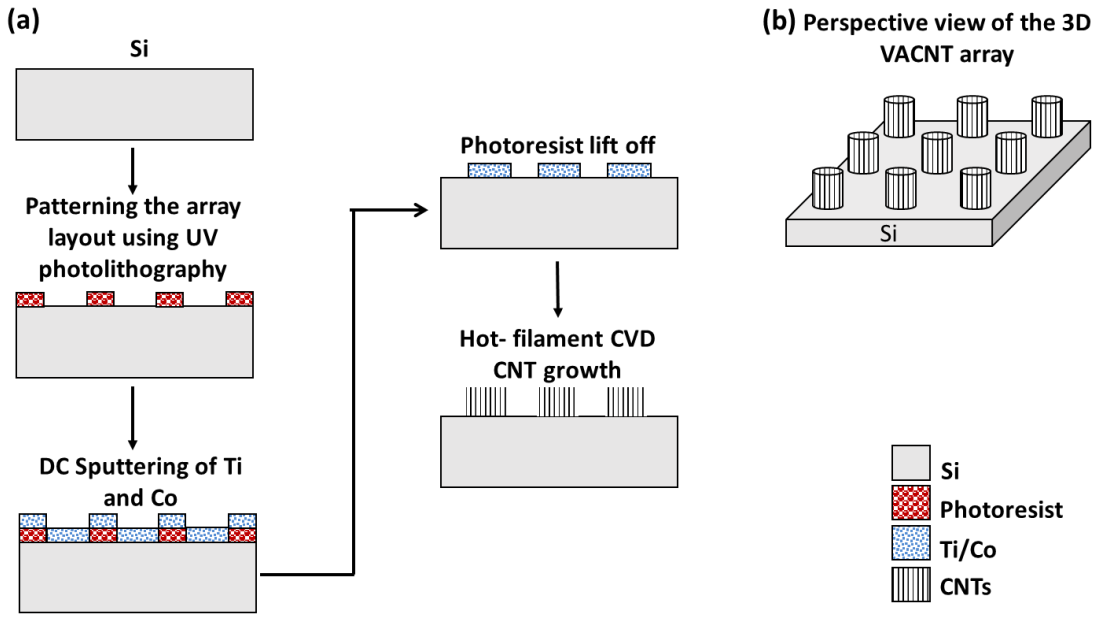


Figure 3.1 (a) Application of the lift-off process for the micropatterning of Si, followed by CNT growth. (b) Perspective view of the HFCVD grown 3D VACNT array on Si.

After mounting the substrate on the vacuum chuck on a WS-400-B-6NPP spin coater, HMDS was applied, followed by drying at 100 $^{o}$C for 30 s. The photoresist was then coated with the spin coater at 4000 rpm and soft baked at 100 $^{o}$C for 90 s. This step was followed by UV exposure through a photo-mask with the array layout on a Cobilt mask-aligner. The samples were developed in an AZ400K /$H_2O$ (1:2 v/v) bath for 45 s and rinsed in de-ionized (DI) water. After hard baking at 135 $^{o}$C for 2 min, thin films of the buffer (Ti - 45 nm) and catalyst (Co - 3 nm) layers were sequentially sputtered in a Cressington 308R D.C. magnetron sputtering system. In the final step of the lift-off process, the samples were agitated via ultrasonication in acetone, and an array of Ti/Co on silicon was obtained.

### 3.1.1. Synthesis of Carbon Nanotubes on Si

The vertically-aligned multi-walled CNTs were synthesized on highly-doped n-type silicon substrates by using HFCVD system. In the HFCVD system, the samples were positioned on the adjustable stage, 25 mm below the tungsten filament and then heated up to 580 $^{o}$C by a substrate heater in a hydrogen ambient at a pressure of 15 torrs. The catalysts were pretreated in this condition for 20 min, followed by an additional 7 min under $H_2$ and ammonia ($NH_3$, 100 ppm in $N_2$) ambient at the same temperature and pressure. After the pre-treatment process, $CH_4$, the carbon precursor gas for CNT growth, was introduced into the chamber with the hot-filament maintained at 2000 $^{o}$C (measured by an Omega dual-color infra-red pyrometer) to break down the input gas mixture. The substrate temperature was maintained at 380 $^{o}$C during the 10 min CNT growth step. The gas flow ratio used in this process was 3:1:3 ($H_2$:$CH_4$:$NH_3$). After the CNT growth, the chamber was cooled down under $H_2$ ambient.

The cross-sectional SEM micrograph of the as-synthesized P-CNTs in Figure 3.2(a) shows the vertically-aligned CNT structures with a height of ~45 μm, while the top-view image in Figure 3.2(b) displays the porous structures of the CNT network which would allow the electrolyte to diffuse freely and enhance the contact/active area. The tilted-view SEM micrograph of the MA-CNTs at 3 kX magnification can be seen in Figure 3.2(c), showing the array of VACNTs; each element of the array has a footprint of ~7.5 x 7.5 μm$^2$ with a height of ~45 μm. These structures possess more open spacing between CNTs that allows the electrolyte to diffuse more easily into the CNT network. The higher magnification

of the MA-CNTs shows the CNT network and a CNT diameter of ~30-50 nm, as illustrated in Figure 3.2(d).

The characterization result using the Raman spectroscopy of the CNTs, which were synthesized in our HFCVD system, was reported elsewhere, as shown in Figure 3.3 [128]. The CNTs have signature $sp^2$-graphitic G-peak at 1590 $cm^{-1}$ and disorder-induced D-peak at 1350 $cm^{-1}$, which indicates that the tubes may have a small degree of structural defects and amorphous carbon.

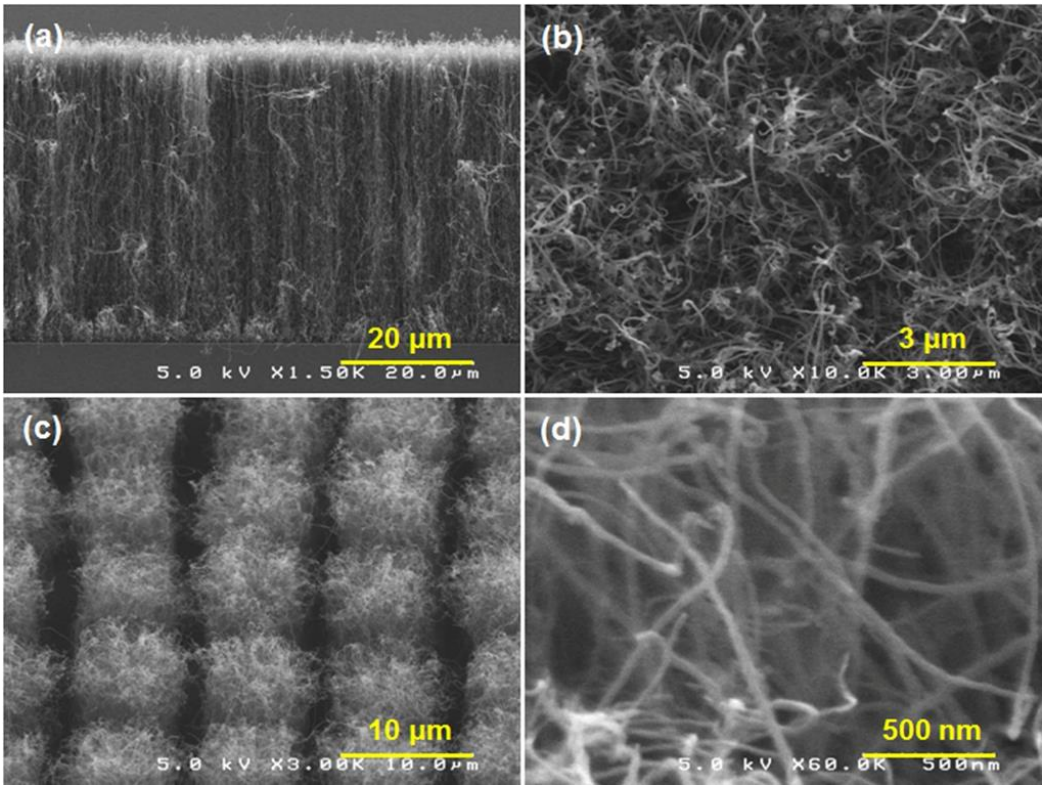


Figure 3.2 (a) and (b) Cross-sectional and top-view SEM micrographs of P-CNT (planar CNTs) grown on a silicon substrate with a height of ~45 µm and the porous structure of the CNT network; (c) and (d) Tilted-view SEM micrographs of MA-CNT (micro-array patterned CNTs) at 3 kX and 60 kX magnifications, showing a part of the array of CNTs and the CNT tube diameter of ~30-50 nm.

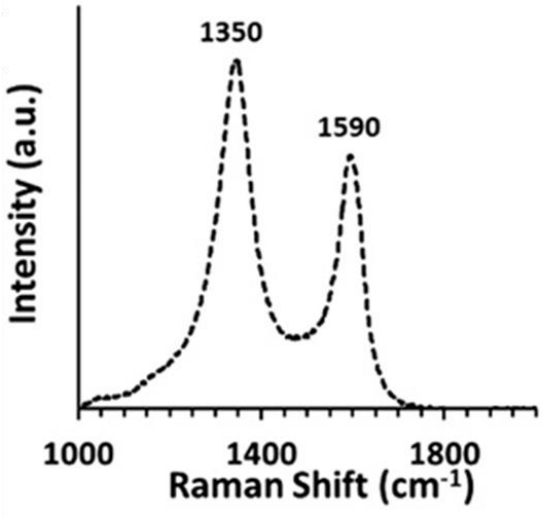


Figure 3.3 Raman spectra of the CNTs, which were synthesized in the HFCVD system. Performed with a green laser (532 nm), the Raman test shows D and G peaks at 1350 $cm^{-1}$ and 1590 $cm^{-1}$, respectively [128].

## 3.2. DSSCs with CNT-Based Cathodes and LiI Electrolyte

### 3.2.1. Fabrication of Dye-Sensitized $TiO_2$ as Photoanode

The $TiO_2$ colloidal paste was first prepared by mixing $TiO_2$ nano-powder (Sigma-Aldrich, P-25) with 0.035 M acetic acid and surfactant (Sigma-Aldrich, X-100). The uniform and reproducible $TiO_2$ films were then fabricated by a repeatable method of spin coating the $TiO_2$ paste onto FTO-coated glass substrates (Hartford Glass Co.) at a given spin rate, followed by a sintering process at 450 °C for 30 min with 50 °C/min ramp-up rate. The sheet resistance of the FTO layer is 10 Ω/sq. Figure 3.4(a) shows that the $TiO_2$ film has a mesoporous structure with $TiO_2$ nanoparticles of ~30 nm in diameter. The total film thickness varied with the spin-coating speed; in the experiments, it was fixed at 1200 r.p.m giving a ~17 μm thick $TiO_2$ film, as shown in Figure 3.4(b). The sintered $TiO_2$ films were then immersed into the dye solution mixed with

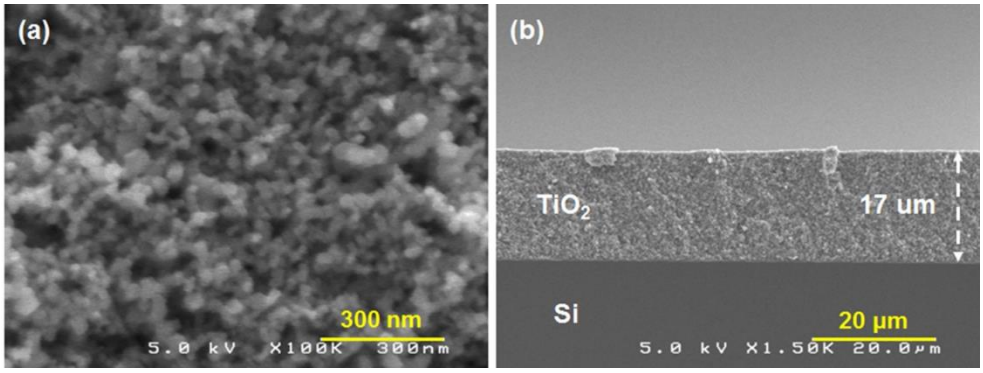


Figure 3.4 SEM micrographs of (a) top-view of the spin-coated $TiO_2$ films with an average ~30 nm $TiO_2$ nanoparticle size; (b) cross-section with a film thickness of ~17 µm.

Di-tetrabutylammonium cis-bis(isothiocyanato)bis(2,2'-bipyridyl-4,4'-dicarboxylato)ruthenium(II) dye (Sigma-Aldrich, N719) in ethanol for 12 h, followed by cleaning with ethanol and drying.

### 3.2.2. Fabrication of CNT and CNT/$MnO_2$ Counter Electrodes

The counter electrodes with bare CNTs were prepared as mentioned before and were used as a comparison with the electrodes with $MnO_2$ coated CNTs, both of which had a circular active area with a diameter of 0.7 cm. The $MnO_2$ films were deposited onto the MA-CNTs using electrochemical reduction of potassium permanganate solution by using a three-electrode configuration with Pt wire as the counter electrode and Ag/AgCl (3 M KCl) as the reference electrode. This three-electrode system is depicted in Figure 3.5 [129]. The permanganate ion ($MnO_4^-$) is reduced to manganese dioxide directly onto the CNTs. This reaction can be expressed as follows:

$$MnO_4^- + 2H_2O + 3e^- \rightarrow MnO_2 + 4OH^- \quad (3.1).$$

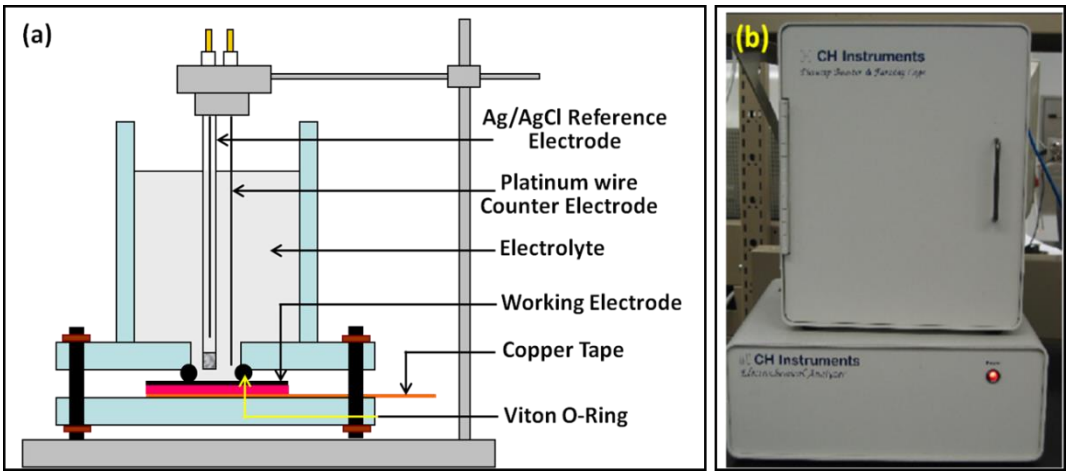


Figure 3.5 The sketch of the three-electrode system in a flat cell with the CNT/Si as the working electrode, Ag/AgCl as the reference electrode, and Pt wire as the counter electrode. (b) The flat cell was employed in CH Instruments' CHI660C model electrochemical workstation [129].

The uniform coating of the $MnO_2$ onto the CNTs can be seen in Figure 3.6(a), while the $MnO_2$-coated MA-CNTs maintain a porous structure, as shown in Figure 3.6(b). The slightly thicker $MnO_2$ coating near the top of each CNT bundle can be attributed to the electric field enhancement, which results in higher deposition rates during the electrochemical deposition process. Figure 3.7 shows

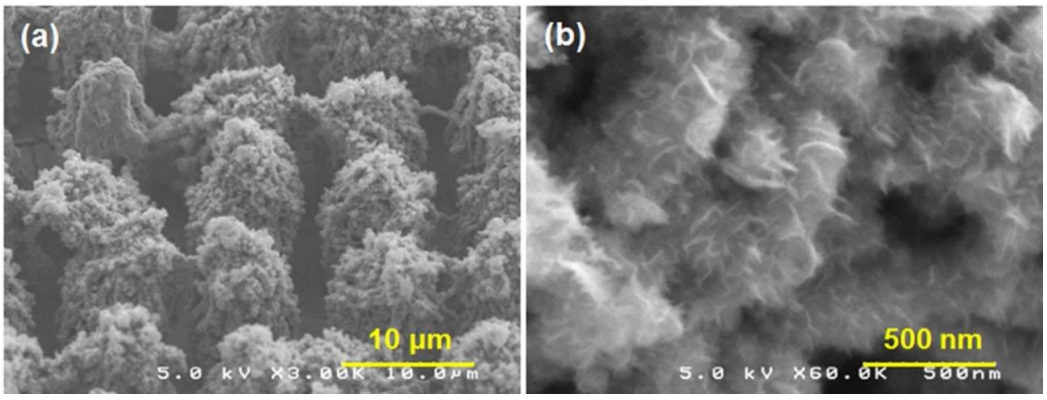


Figure 3.6 The tilted-view SEM micrographs of the micro-array patterned CNTs uniformly coated with porous $MnO_2$ layers at (a) 3 kX and (b) 60 kX magnifications, respectively.

the Raman spectrum for the $MnO_2$ coated CNTs fabricated in our laboratory [128]. The sharp peak at 635.5 $cm^{-1}$ (with FWHM = 40 $cm^{-1}$) can be attributed to the presence of α-$MnO_2$ phase and the absence of $sp^2$-graphitic and disorder-induced signals from the CNTs due to the overlying $MnO_2$ layer. A 400 nm thick Pt-film was also sputtered onto an *n*++ silicon substrate for characterization as the control counter electrode.

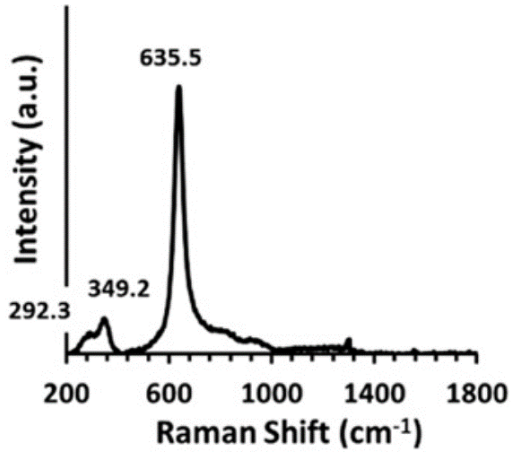


Figure 3.7 Raman spectra of the $MnO_2$ coated CNTs, which were synthesized in the HFCVD system. The excitation source was a green laser (532 nm). Different peaks are the indicators of the Mn-O vibration bands [128].

### 3.2.3. Photovoltaic Performance of the DSSCs

The iodide-based electrolyte was prepared in acetonitrile solvent with a composition of 0.5 M LiI, 0.05 M $I_2$ and 0.5 M 4-tert-butylpyridine, purchased from Sigma-Aldrich. The electrodes, which had an active area of ~0.38 $cm^2$ (0.786 $cm^2$ for Pt electrode), were saturated with the electrolyte before assembling them in a sandwich with a 50 µm thick scotch tape as the spacer. Binder clips were used to apply external pressure on the photoelectrode–counter electrode

assembly. The photovoltaic performance of the solar cells was determined by the photocurrent density (J) vs. voltage (V) characteristics at 1 sun (100 mW/cm$^2$) of air mass 1.5 G illumination intensity without a mask. An Oriel solar simulator (model 96000, power calibration performed based on user manual instructions) with an AM 1.5 G filter was used, and staircase voltammetry technique in an electrochemical workstation (CH Instruments CHI660C) were utilized for the I-V measurements. The sampling delay time and the measuring integration time were both 0.5 s, and the voltage source step size was set to 10 mV [130].

In Figure 3.8, the photocurrent density versus voltage plots of the DSSCs using the P-CNTs, MA-CNTs, $MnO_2$-coated MA-CNTs, and Pt counter electrodes are overlaid. The short-circuit current density ($J_{sc}$), the open-circuit voltage ($V_{oc}$) and the fill factor for Pt-DSSC are 20.6 mA/cm$^2$, 0.7 V, and 0.44, respectively, while those of the P-CNTs are 26.3 mA/cm$^2$, 0.74 V, and 0.38, respectively. The DSSC with P-CNTs exhibited a higher $\eta$ of 7.13 % as compared to the cell with the Pt counter electrode with an $\eta$ of only 6.29 %. The enhancement of $\eta$ can be attributed to the increased $J_{sc}$ and $V_{oc}$ by using vertically-aligned CNTs counter electrode, which provided a larger surface area to the electrolyte and thereby a better catalytic behavior than Pt.

The value of $J_{sc}$ is determined by several factors such as the efficiency of light absorption by the dye molecules, the efficiency of charge transfer at dye-sensitized-$TiO_2$/electrolyte interface, and the catalytic performance of the counter electrode. The catalytic activities of the counter electrode depend on the charge-transfer resistance ($R_{ct}$), the Nernst diffusion impedance inside the electrode pores ($Z_{N,\ pore}$), the electrochemical capacitance at the CNT/electrolyte interface,

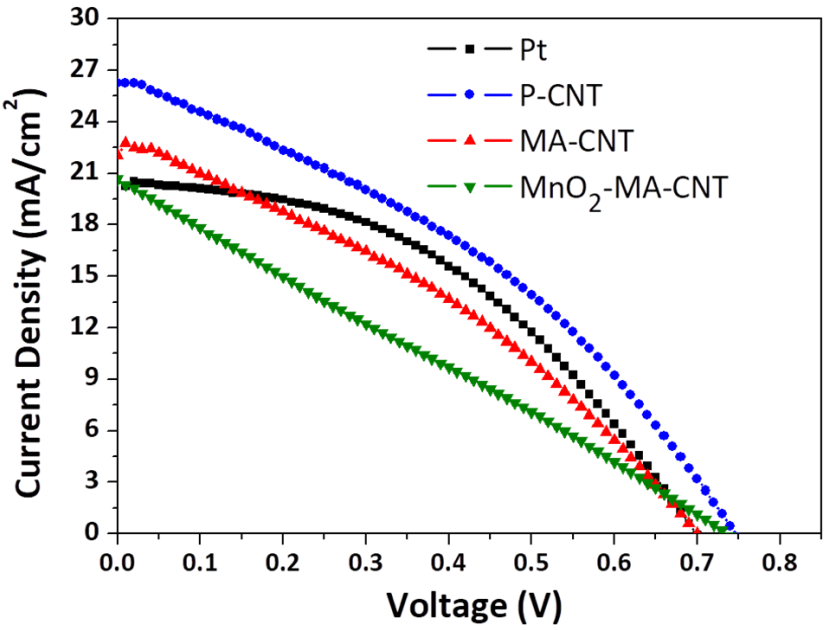


Figure 3.8 The photocurrent density versus voltage curves of the DSSCs using different counter electrodes consisting of Pt, P-CNT (planar CNTs), MA-CNTs (micro-array patterned CNTs), and $MnO_2$-coated MA-CNTs under 1 sun AM 1.5 G illumination.

and the series electrical resistance ($R_e$) at the CNT/silicon interface [131,56]. The vertically-aligned CNT geometry provides a 3D network for greater access of the electrolyte to the CNT surfaces and increases the contact area between the counter electrode and the electrolyte. Thus, $R_{ct}$ becomes smaller, and the electrochemical capacitance increases, thereby enhancing the charge transfer at the CNT/electrolyte interface. Therefore, the enhanced catalytic performance of CNTs with more efficient charge transfer and larger surface area than that of conventional Pt possibly leads to higher $J_{SC}$ and $V_{OC}$ [132].

A lower fill factor, ~14 % less compared to Pt-DSSC, is possibly due to the high series resistance associated with the large thickness of the vertically aligned CNT electrode. In the previous studies where 3D carbon structures, such as CNT

or carbon nanofiber-based counter electrodes were used in DSSCs, scientists witnessed similar effects on the fill factor [132-134]. For example, Velten's group observed a higher series resistance between the CNTs and the substrate as compared to that between a few nanometer thick Pt-film and the substrate, which restrained electrons' motion, causing a lower fill factor [133]. In addition, our cell with MA-CNTs counter electrode exhibited a $J_{sc}$ of 22.1 mA/cm$^2$ and a $V_{oc}$ of 0.7 V. The reduced $J_{sc}$ can be attributed to the increased $R_{ct}$ due to the lower quantity of vertically-aligned CNTs, and thus, the reduced contact area at the interface of MA-CNTs and the electrolyte, as compared to the P-CNT electrode. The overall fill factor of the cell with MA-CNTs decreased by 8 % to 0.35, and a lower η of 5.47 % was obtained.

Electrochemical impedance spectroscopy (EIS) measurements of the DSSC counter electrodes were conducted using the CHI660C electrochemical workstation in a three-electrode configuration with a Pt wire as the counter electrode and an Ag/AgCl as the reference electrode in the same LiI/$I_2$ electrolyte solution. The frequency range of the EIS was between 0.1 Hz and 0.1 MHz, and the AC amplitude was 10 mV. The Nyquist plots recorded for the P-CNTs and MA-CNTs are overlaid and can be seen in Figure 3.9. The semicircles at lower frequencies on the right correspond to the charge transfer resistance at the CNT/electrolyte interface, while the parts of other semicircles at higher frequencies on the left correspond to the Pt/electrolyte interface [135].

To better understand the physical processes contributing to the counter electrode's catalytic response, an equivalent circuit was designed, as shown in Figure 3.10 [136]. Electrolyte and wire resistances (in series) are written as $R_e$. The

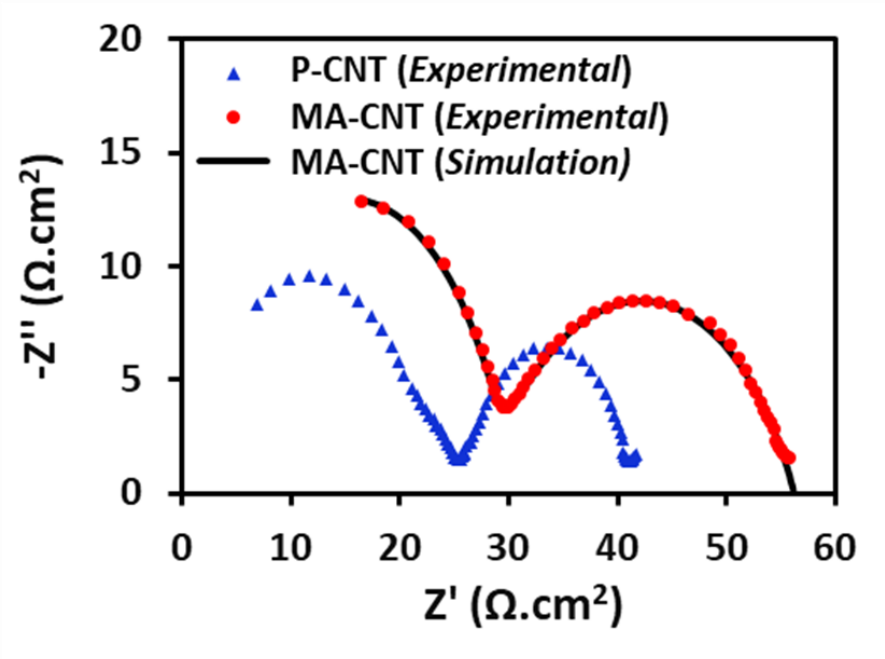


Figure 3.9 The electrochemical impedance spectra (Nyquist plots) of the P-CNTs (planar) and MA-CNTs (micro-array patterned CNTs) evaluated in a three-electrode configuration using Pt wire as the counter electrode and an Ag/AgCl reference electrode in LiI/$I_2$ electrolyte solution. The simulated impedance spectrum of the MA-CNTs' equivalent circuit is also overlaid.

component, $R_{eq}$, denotes the equivalent resistance of $R_{ct}$ in series with $Z_{N,\ pore}$. The $R_{eq}$ is also in parallel to a double layer constant phase element ($CPE_{dl}$), which is an imperfect capacitor, having an impedance formulated as

$$Z_{CPE} = \frac{1}{Q_0\,\omega^{\beta}}\, e^{-i\frac{\pi}{2}\beta} \qquad (3.2),$$

where $0 \leq \beta \leq 1$, and $\omega$ stands for angular frequency [137]. The numerical value of $Q_0$ (Siemens-second$^{\beta}$) is the same as that of the admittance ($1/|Z_{CPE}|$) of the structure when $\omega = 1$ *rad/s*. The CPE is closer to an ideal capacitor when the value of $\beta = 1$; it is equivalent to a resistor when $\beta = 0$. A similar imperfect capacitive effect is seen during the diffusion of ions at lower frequencies, which is represented by $CPE_{diff}$ and accompanied by a parallel Nernst diffusion

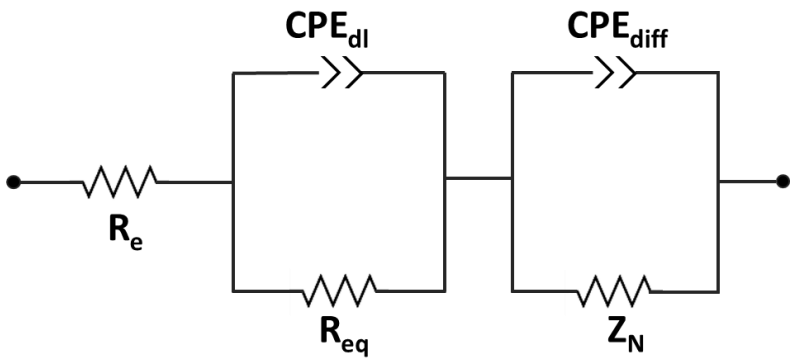


Figure 3.10 Equivalent circuit of the DSSC cathode in a three-electrode setup.

impedance ($Z_N$) component. The $Z_N$ can be formulated as follows:

$$Z_N = \frac{kT}{A\, n^2\, e_0^2\, c\, \sqrt{i\omega}}\ tanh\left(\sqrt{\frac{0.25\, i\, \omega}{D_I\, L}}\right) \qquad (3.3),$$

where $k$ is the Boltzmann constant, $T$ is the absolute temperature, $A$ is the electrode area, $n$ is the number of electrons participating in the electrochemical reaction, $e_0$ is the elementary charge, $c$ is the concentration of $I_3^-$, $D_I$ is the diffusion coefficient of $I_3^-$ in the electrolyte, and $L$ is the distance between the electrodes [137]. Based on the equivalent circuit in Figure 3.10, the impedance spectrum of the MA-CNTs cathode was simulated and overlaid with the electrochemical impedance spectrum, which is derived from the EIS experiment conducted in the three-electrode setup and shown in Figure 3.5(a). The fitting parameters of the simulated circuit's components are: $R_e = 0.77\ \Omega.cm^2$, $R_{eq} = 27.72\ \Omega.cm^2$, $Z_N = 27.72\ \Omega.cm^2$, $Q_{0\_CPE\_dif} = 1.112x10^{-4}$, $Q_{0\_CPE\_dl} = 4.8x10^{-8}$, $\beta_{CPE\_diff} = 0.694$, and $\beta_{CPE\_dl} = 0.946$. The heights of the CNTs in both planar and micro-array patterned configurations were about the same, so it can be assumed that the diffusion distance of the iodide ions from the top of the CNTs to the

photoelectrode is the same in both cells. The higher $R_{ct}$ of the CNTs in the micro-array patterned configuration than in the planar configuration was also confirmed by the electrochemical impedance spectra of the P-CNTs and MA-CNTs (Figure 3.9).

The photovoltaic performance of the DSSC was expected to decline after the addition of the manganese dioxide thin-film onto the MA-CNTs counter electrode, due to the insulating nature of $MnO_2$. The $J_{SC}$ decreased to 20.7 mA/cm$^2$ while the $V_{OC}$ increased to 0.73 V. The corresponding fill factor was reduced by 26 % to 0.26. The reduction of $J_{SC}$ and fill factor can be attributed to the increased $R_{ct}$ at the interface of the $MnO_2$-coated MA-CNTs and the $LiI/I_2$ electrolyte due to the lower catalytic activity of the $MnO_2$ layer. The improvement in the $V_{oc}$ can be attributed to the modification of the electrolyte redox potential due to the reaction between $MnO_2$ and $Li^+$ [138]. The power conversion efficiency reduced to 3.88 % by using the $MnO_2$-coated CNTs in the micro-array patterned configuration. Nevertheless, these results indicate a possible candidate for a common electrode for direct storage of solar energy in self-powering systems, combining photoanodes with supercapacitor cathodes in a DSSC. Table 3.1 summarizes and compares the photovoltaic performance of the DSSCs studied in this work.

Table 3.1 Summary of the photovoltaic characteristics obtained from different counter electrodes under 1 sun AM 1.5G illumination.

| **Counter Electrodes** | **$J_{sc}$ (mA/cm$^2$)** | **$V_{oc}$ (V)** | **FF** | **$\eta$ (%)** |
|---|---|---|---|---|
| **Platinum (*Control sample*)** | 20.6 | 0.70 | 0.44 | 6.29 |
| **P-CNT (*Planar CNTs*)** | 26.3 | 0.74 | 0.38 | 7.13 |
| **MA-CNT (*Micro-array patterned CNTs*)** | 22.1 | 0.70 | 0.35 | 5.47 |
| **$MnO_2$ / MA-CNT ($MnO_2$-coated MA-CNTs)** | 20.7 | 0.73 | 0.26 | 3.88 |

## 3.3 Summary

- P-CNT and MA-CNT cathodes on Si substrates were successfully fabricated through an HFCVD process.
- $MnO_2$ coating onto MA-CNT was achieved in a three-electrode system through the CV technique.
- A uniformly coated and N-719 dye-sensitized $TiO_2$ on FTO was fabricated as a photoanode. Spin coating technique yielded identical, reproducible, and controllable $TiO_2$ film on FTO substrates, for comparing the counter electrodes' performance.
- The P-CNTs exhibited higher power conversion efficiency (7.13 %) than Pt (6.29 %), indicating the potential to replace the Pt layer by CNTs in conventional DSSCs for greater cost efficiency and performance.

- The $MnO_2$-coated MA-CNT cathode, although exhibited reduced efficiency, provided a feasible method for the integration of energy conversion and storage devices for self-powering systems.
- Both P-CNTs and MA-CNTs cathodes exhibited higher photocurrent density (Jsc) than Pt, possibly due to better catalytic behavior of the CNTs owing to higher contact surface area with the electrolyte. The P-CNTs exhibited a very high Jsc of 26.3 $mA/cm^2$, which is the highest obtained so far for the vertically aligned CNTs to the best of our knowledge.

# CHAPTER IV

# PHOTOCAPACITORS WITH $MnO_2$/CNT-BASED CATHODES

In this chapter, the details of the fabrication process and the characterization of photocapacitor components are presented. The photoanodes were prepared in the same way as mentioned in Chapter 3 so that a repeatable $TiO_2$ film deposition onto an FTO-coated glass was achieved. Manganese dioxide-coated vertically aligned MA-CNTs grown on Si substrates were used as the counter electrodes. The $MnO_2$ coating was done in a three-electrode setup in an electrochemical workstation described previously. Tetraethylammonium tetrafluoroborate (TEABF4) in acetonitrile was employed as a redox mediator for the photovoltaic reactions and a charge transfer media for the pseudocapacitive reactions. The response of different amount of $MnO_2$ coatings to both photovoltaic and capacitive performances of the photocapacitor counter electrodes was also studied.

## 4.1. Photocapacitors with a Dye-Sensitized Photoanode and $MnO_2$ Coated Micro-Array CNTs as Supercapacitor Counter Electrode

### 4.1.1. Fabrication of the Photocapacitors with Different Counter Electrodes

The fabrication of the photoanodes and the synthesis of the vertically aligned MA-CNTs on n++ Si substrates were carried out following the same

methods described in Chapter 3. Electrochemical deposition of $MnO_2$ was performed using the same techniques described in the previous chapter. As part of this work, three photocapacitors with different cathodes were fabricated, two of which consisted of MnO2 coated MA-CNTs with 2 and 4 CV cycles and labeled as PC-1 and PC-2, respectively. The third photocapacitor, PC-0, which has the MA-CNT cathode, was used as the control.

Before assembling the photocapacitors, the electrodes were saturated with the electrolyte consisting of 1 M TEABF4 in acetonitrile (ACN). A 50 µm thick scotch tape with a 0.7 cm diameter aperture was used as the spacer between the electrodes. The photocapacitor device was secured with binder clips that also maintained adequate pressure. The photovoltaic and the galvanostatic-discharge characterization studies were performed on the CHI660C electrochemical workstation. An Oriel solar simulator (model 96000) equipped with a filter of AM 1.5 G was used at 1-sun (100 $mW/cm^2$) illumination intensity. The photovoltaic performances of the photocapacitors were evaluated through I-V measurements using the staircase voltammetry technique with the following parameters: 0.5 s for both the sampling delay time and the measuring integration time and 10 mV as the voltage source step size [130].

The top view SEM micrograph in Figure 4.1(a) shows the three-dimensional CNT array layout with each microelectrode having ~4 µm diameter. The CNT height achieved by the synthesis recipe used is typically ~45 µm, based on other characterization performed. The high-resolution SEM micrograph in Figure 4.1(b) shows a porous structure allowing for an excellent platform to

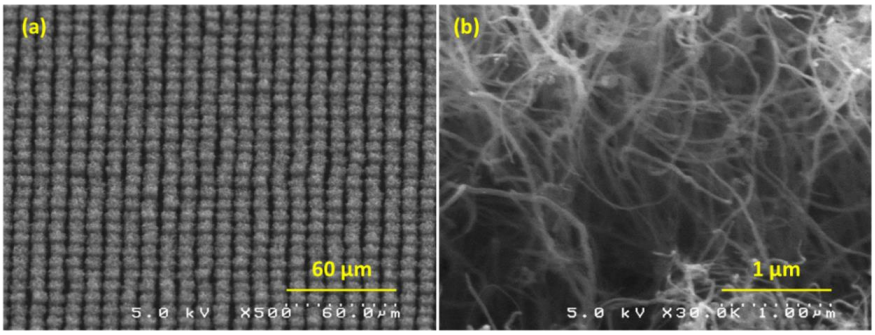


Figure 4.1 SEM micrographs of the as-grown MA-CNTs on Si: (a) Tilt view showing the micro-array patterned CNT layout; (b) High-resolution SEM image showing the microstructure of the multi-walled CNTs.

achieve a uniform $MnO_2$ coating and support the facile diffusion of the electrolyte as well.

Top-view SEM micrograph in Figure 4.2(a) shows a uniform $MnO_2$ coating on the MA-CNT, while a high magnification micrograph in Figure 4.2(b) reveals the porous microstructure of the $MnO_2$ film.

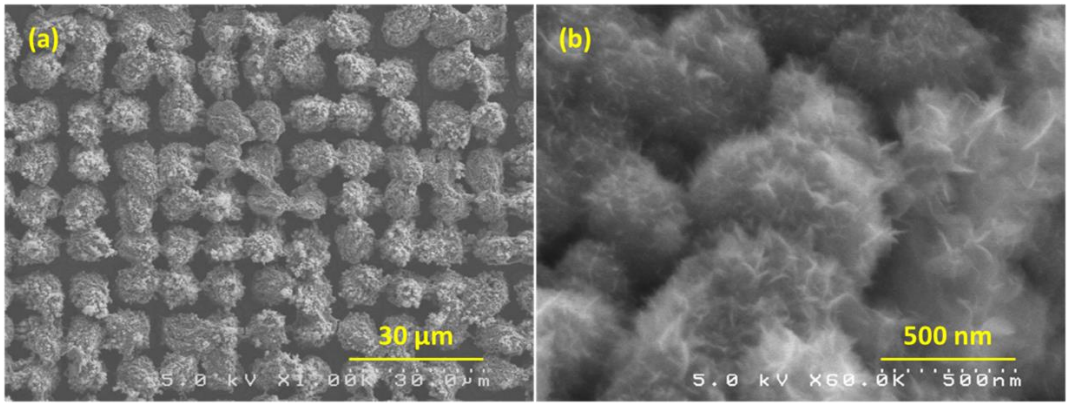


Figure 4.2 SEM micrographs of $MnO_2$ coated MA-CNTs: (a) Top-view showing the uniformly coated array; (b) High-resolution SEM image showing the porous microstructure of the $MnO_2$ film conducive for energy storage applications.

### 4.1.2. Photovoltaic Performance of the Photocapacitors with Different $MnO_2$ Coatings

To better understand the charging behavior of the photocapacitor under the exposure to sunlight, the phenomenological order of the processes is presented in the schematic diagram in Figure 4.3. The photovoltaic response of the photocapacitors PC-0, PC-1, and PC-2 were also recorded as the photocurrent density (mA/cm$^2$) versus voltage (V) curves under 1-sun illumination and are overlaid in Figure 4.4. The corresponding values for $V_{OC}$, short circuit current density ($J_{SC}$), and fill factor (*FF*) data are summarized in Table 4.1. In the case of the photocapacitor PC-0, with no $MnO_2$ coating, the values for the $J_{SC}$, $V_{OC}$, FF, and $\eta$ are 0.234 mA/cm$^2$, 0.2 V, 0.08, and 0.004, respectively. The relatively low values can be attributed to the use of an unconventional electrolyte for photovoltaic charging. As compared to the conventional $I_3^-/I^-$ redox couple where two electrons are involved in the reaction, the $BF_4^-/BF_3$ couple supports only a single electron transfer (steps 3 and 4 in Figure 4.3) [139]. In contrast, the

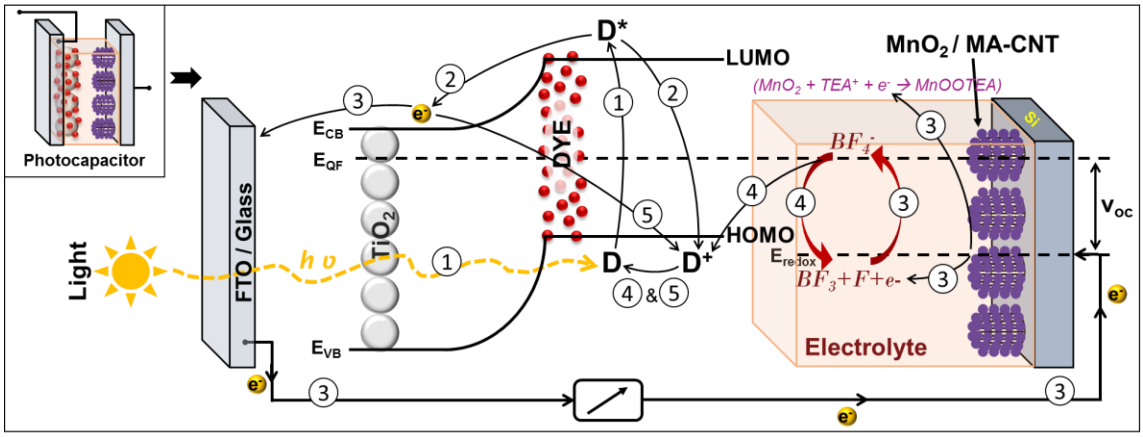


Figure 4.3 Schematic representation of the sequence of the processes inside the dye-sensitized $TiO_2$ - $MnO_2$/CNT photocapacitor during solar charging.

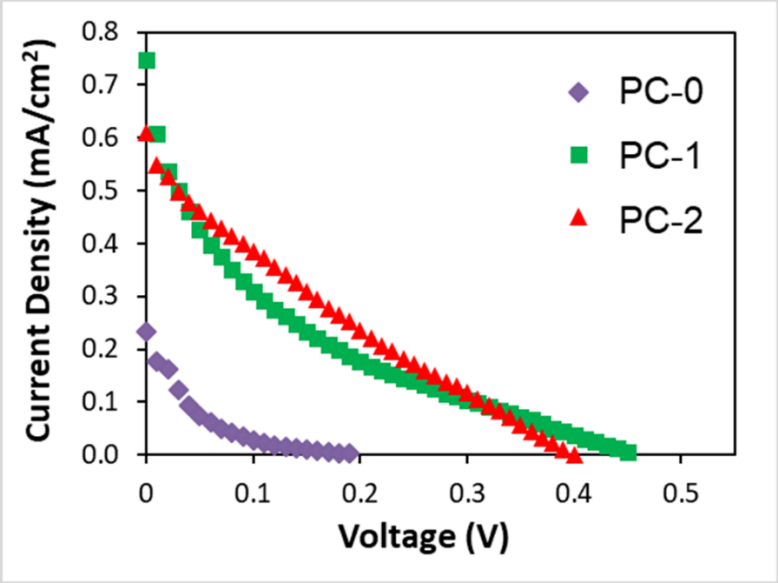


Figure 4.4 The photocurrent density (mA/cm$^2$) versus voltage (V) curves of the photocapacitors PC-0, PC-1, and PC-2 with counter electrodes having 0, 2, and 4 CV-cycles of $MnO_2$ coating on MA-CNTs, respectively.

MA-CNT substrates with $MnO_2$ coating, electrodes for PC-1 and PC-2 show a marked improvement in all these photovoltaic parameters. The highest $J_{SC}$ and $V_{OC}$ values of 0.749 mA/cm$^2$ and 0.46 V, respectively, were obtained for PC-1. In the case of these photocapacitors, not all the photogenerated electrons contribute to the redox reactions inside the electrolyte, but some are captured by the pseudocapacitive counter electrode ($MnO_2$/MA-CNT) as part of the charge storage reaction shown below:

$$MnO_2 + TEA^+ + e^- \rightarrow MnOOTEA \qquad (4.1).$$

The improvement in the photovoltaic parameters may be attributed to the fact that reaction (4.1) at the electrode-electrolyte interface leads to a greater degree of electrolyte's ionization reaction seen below:

$$TEABF4 \rightarrow TEA^+ + BF_4^- \qquad (4.2).$$

Table 4.1 Photovoltaic (through I-V analysis) performances of the photocapacitors PC-0, PC-1, and PC-2 obtained under 1-sun illumination.

| # of cycles for $MnO_2$ coating (Sample) | $J_{SC}$ (mA/cm$^2$) | $V_{OC}$ (V) | Fill Factor (FF) | Efficiency ($\eta$) (%) |
|---|---|---|---|---|
| 0 (PC-0) | 0.234 | 0.20 | 0.080 | 0.004 |
| 2 (PC-1) | 0.749 | 0.46 | 0.103 | 0.036 |
| 4 (PC-2) | 0.610 | 0.41 | 0.193 | 0.048 |

The increase in the $BF_4^-$ concentration, in turn, contributes to dye regeneration reactions based on the $BF_4^-/BF_3$ redox couple, as indicated by step 4 in Figure 4.3. As the amount of $MnO_2$ coating increased in the case of PC-2, we observed a drop in $J_{SC}$ and $V_{OC}$ to 0.61 mA/cm$^2$ and 0.41 V, respectively. These drops can be attributed to the increased resistance due to thicker $MnO_2$ coating in PC-2. The smaller $J_{SC}$ and $V_{OC}$ obtained from the higher amount of $MnO_2$ may also be responsible for more linear *J* vs. *V* response, which yields a nearly 2x increase in the fill factor and therefore the overall efficiency in PC-2, as compared to PC-1.

### 4.1.3. Capacitive Performance of the Photocapacitors with Different $MnO_2$ Coatings

The energy storage performance of the photocapacitors was characterized after charging them under 1-sun illumination for 40 min, followed by a constant-current discharge in the dark at 10 μA. The charge (*V-t*) and discharge (*V-t*) curves of PC-1 and PC-2 are overlaid and presented in Figures 4.5(a) and (b), respectively. The higher $MnO_2$ content in PC-2 provides more stable performance, allowing it to charge up to 0.932 V, as compared to only 0.853 V, in the case of PC-1. We also observed an enhancement in the

discharge step, where a higher capacitance of 13.1 mF/cm$^2$ for PC-2 was obtained, nearly 33% more than PC-1. The results obtained from PC-1 and PC-2 are summarized in Table 4.2. The use of a 3D network of CNTs in a micro-array patterned design with its high electronic conductivity provides an excellent platform for fabricating $MnO_2$ coated electrodes for photocapacitors [140,141]. The separator-free structure is another contributor to better ionic conductivity and thereby the device performance [142,143].

Additional charge storage characterization was performed on PC-2 using the same parameters, but with varying solar charge durations of 3, 6, 12, 20, and 40 min. Constant-current discharge (*V*-*t*) curves are overlaid, as illustrated in Figure 4.6(a). Accordingly, Figure 4.6(b) shows that the discharge capacitance obtained from PC-2 increased consistently from ~4.4 mF/cm$^2$ after 3 min of charging to ~13.1 mF/cm$^2$ after 40 min of charging. Manganese dioxide can store a higher amount of charge based on reaction 4.1 with prolonged charging due to

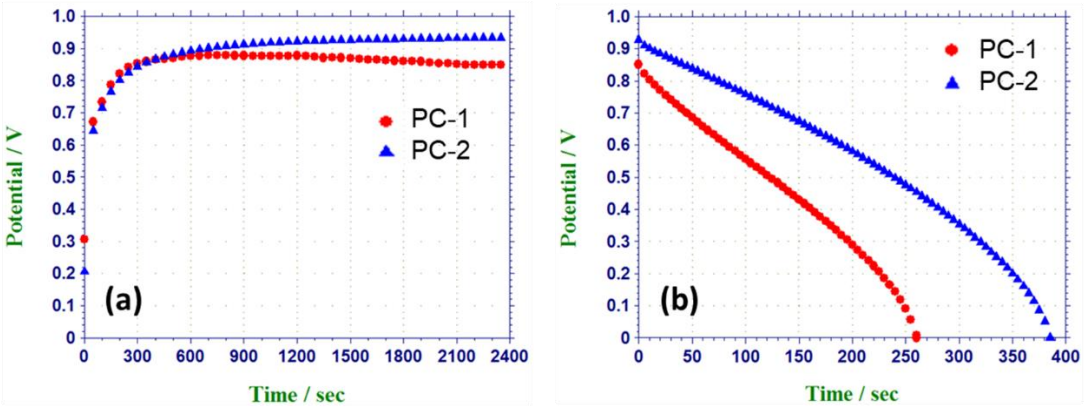


Figure 4.5 Voltage (V) versus time (s) curves of the photocapacitors PC-1 and PC-2 with different amounts of $MnO_2$ coatings: (a) Charging curves under 1-sun for 40 min; (b) Discharge curves at 10 μA constant-current.

Table 4.2 Energy storage performances of the photocapacitors PC-0, PC-1, and PC-2, after 1-sun solar charge for 40 min and 10 μA constant-current discharge.

| Sample | Charged Voltage (V) | Discharge Capacitance ($mF/cm^2$) |
|---|---|---|
| PC-1 | 0.853 | 8.8 |
| PC-2 | 0.932 | 13.1 |

its pseudocapacitive behavior, somewhat similar to secondary batteries. The charging voltage shows an increase to the maximum value from 0.848 V after 3 min of charging to 0.955 V after 12 min of charging but decreases to 0.932 V after 40 min of charging. At this stage, the reason for this behavior is not apparent; however, it may be due to changes in the electrolyte arising from slow evaporation of the solvent at high temperatures during solar illumination from the open edges of the counter electrode substrate, which in turn increases the salt

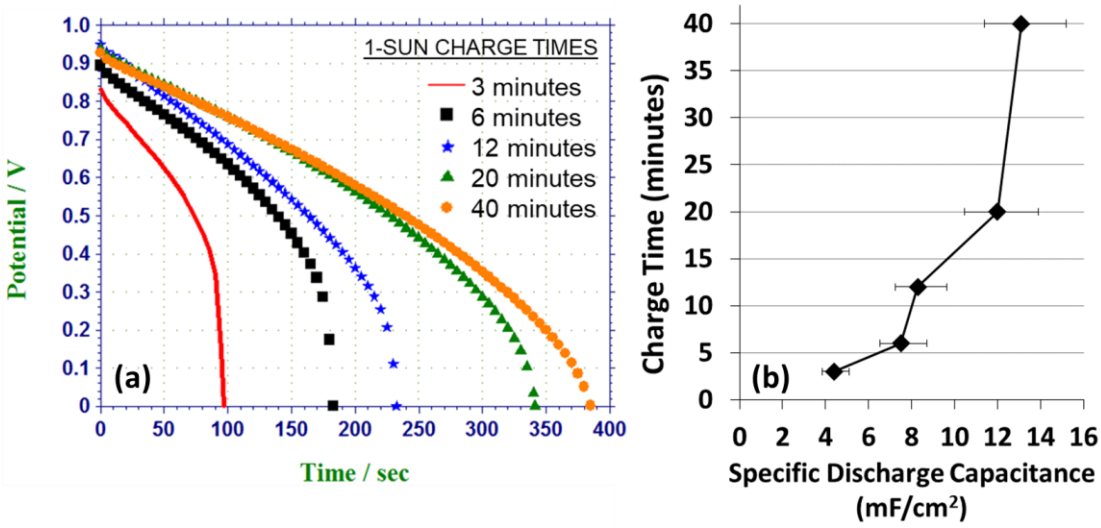


Figure 4.6 (a) Voltage (V) versus time (s) curves of the photocapacitor PC-2 under 10 μA constant-current discharge after 3, 6, 12, 20, and 40 min of solar charging at an illumination of 1 sun; (b) specific discharge capacitance (with uncertainty bars) vs. charge time.

concentration. We were able to test the devices' performance within the first two hours after the assembly, but consistently observed a considerable decay in the JSC, VOC, and discharge capacitance of the devices after 2 h, supporting the possibility for changes in the electrolyte. At higher concentrations, the charge carriers tend to form ion pairs that are electrically neutral and thus lead to reduced ionic conductivity [144]. The results of these experiments for PC-2 are summarized in Table 4.3. Overall, they can be considered promising for the application of pseudocapacitive electrodes to store energy in an integrated photocapacitor.

Table 4.3 Energy storage performance of PC-2 obtained after 1-sun solar charging for varying times, followed by 10 μA constant-current discharge.

| Cycle # | 1-Sun Charge Time (min.) | Charged Voltage (V) | Discharge Capacitance ($mF/cm^2$) |
|---|---|---|---|
| 1 | 3 | 0.848 | 4.4 |
| 2 | 6 | 0.901 | 7.5 |
| 3 | 12 | 0.955 | 8.3 |
| 4 | 20 | 0.942 | 12.0 |
| 5 | 40 | 0.932 | 13.1 |

## 4.2. Summary

- Integrated photocapacitors, made of N-719 dye-sensitized $TiO_2$ on FTO substrates as the photoanode, TEABF4 electrolyte, and $MnO_2$ coated micro-array patterned CNTs on Si substrates as the supercapacitor counter electrode, were successfully fabricated and characterized.

- The device was the first photocapacitor utilizing a $MnO_2$-based supercapacitor electrode.
- Highest values of the $J_{SC}$ and $V_{OC}$ recorded were 0.749 mA/cm$^2$ and 0.46 V, respectively; while a maximum FF obtained was 0.193.
- The low photovoltaic performance can be attributed to using a single, unconventional electrolyte (TEABF4) with a different redox couple available for the dye regeneration that involves only a single electron transfer. In contrast, the highest charging potential achieved was 0.955 V, which is the highest among the photocapacitors fabricated by other researchers, and capacitance of 13.1 mF/cm$^2$ was obtained using 10 µA discharge current, highlighting the influence of the pseudocapacitive response of $MnO_2$.
- The proposed design of a compact, integrated photocapacitor showed promising results by leveraging the 3D architecture of $MnO_2$ CNT arrays as an active charge storage counter electrode.

# CHAPTER V

# A NOVEL LITHIUM-ION BATTERY CATHODE MATERIAL: $Li_2Fe_xMn_yCo_zSiO_4$

This chapter elaborates on the fabrication of a new LIB cathode material: $Li_2Fe_xMn_yCo_zSiO_4$ (x + y + z = 1). The material's attachment onto a conductive vertically aligned CNT network on graphite substrate as the current collector is detailed. The structural and electrochemical characterizations of the material were also included.

## 5.1. Fabrication of a Novel Active Cathode Material

### 5.1.1. Carbon Nanotube on Graphite as a Host Material for Cathode

Graphite was used as a current collector for its lightweight, low cost, flexible, high electric and thermal conductivity, and chemically inert features [145]. Graphite foil, which is 127 µm thick and non-inhibited grade developed for use in nuclear or semiconductor applications (typically 99.8% pure) was purchased from Mineral Seal Corporation and used for the CNT growth. Small pieces were cut in two different configurations, 15 mm x 20 mm and 40 mm x 19 mm active cathode area, and an extension of 10 mm x 4 mm was left as an electrical contact area. Sample weight measurements were performed on Denver Instrument's APX-100 microbalance. VWR's Clinical 200 was employed as the centrifuge system for the

cathode suspension preparation. During the LIB cell assembly, Celgard's 25 µm thick polypropylene film (purchased from MTI Corporation) with a pore size of 0.21 µm x 0.05 µm was used as the separator. An aluminum laminated film with polypropylene and polyamide for the pouch cell case, and Al and Ni tabs, for the positive and negative terminals of the cell, respectively, were also purchased from MTI Corporation.

Graphite substrates were first cleaned with methanol, followed by drying at 100 $^{o}$C. Before the CNT growth, 15 nm titanium (buffer) and 3 nm cobalt (catalyst) were sequentially coated onto the substrates in Cressington 308R D.C. magnetron sputtering system. The VACNTs were synthesized in the HFCVD system, following the synthesis method described in Chapter 3. During the pretreatment and the CNT-growth processes, the substrate temperature was kept at 750 $^{o}$C.

### 5.1.2. Dilithium Ternary Orthosilicate - $Li_2(Fe_xMn_yCo_z)SiO_4$ Synthesis and Li-Ion Battery Cell Fabrication

$Li_2(Fe_xMn_yCo_z)SiO_4$ (dilithium ternary orthosilicate, or DTS, and x + y + z = 1) materials with different stoichiometric ratios of Fe (x = 0.5, 0.6, 0.7, and 0.8) were synthesized by a sol-gel process similar to Deng et al., using the mixture of manganese acetate tetrahydrate ($Mn(CH_3COO)_2{\cdot}4H_2O$), lithium acetate dihydrate ($CH_3COOLi\cdot 2H_2O$), iron (III) citrate hydrate ($C_6H_5FeO_7$-$xH_2O$), and cobalt carbonate ($CoCO_3$) in a solution of citric acid monohydrate in de-ionized water; followed by the addition of a tetraethyl orthosilicate (TEOS)/ethanol

solution [146]. Stoichiometric ratios of Mn and Co were kept the same (y = z) in these experiments. As shown in Figure 5.1, the mixture was stirred and heated in a volumetric flask immersed in a water bath at 70 $^{o}$C, until all the salts were dissolved. The resulting solution was clear, dark green colored. After adding TEOS/ethanol, the flask was maintained at 70 $^{o}$C, and the solution was continuously stirred for 24 h until getting the 'sol'- colloidal solution. Next, the water and ethanol were evaporated, thus forming a 'gel'. This gel was placed into a tube furnace and further dried at 100 $^{o}$C for 24 h under Ar flow at a flow rate of 25 sccm. It was then ground, and calcinated at 600 $^{o}$C for 90 min under Ar flow, transforming the color to black due to the decomposition of the excess citric acid used at the beginning of the synthesis. The use of citric acid has two purposes:

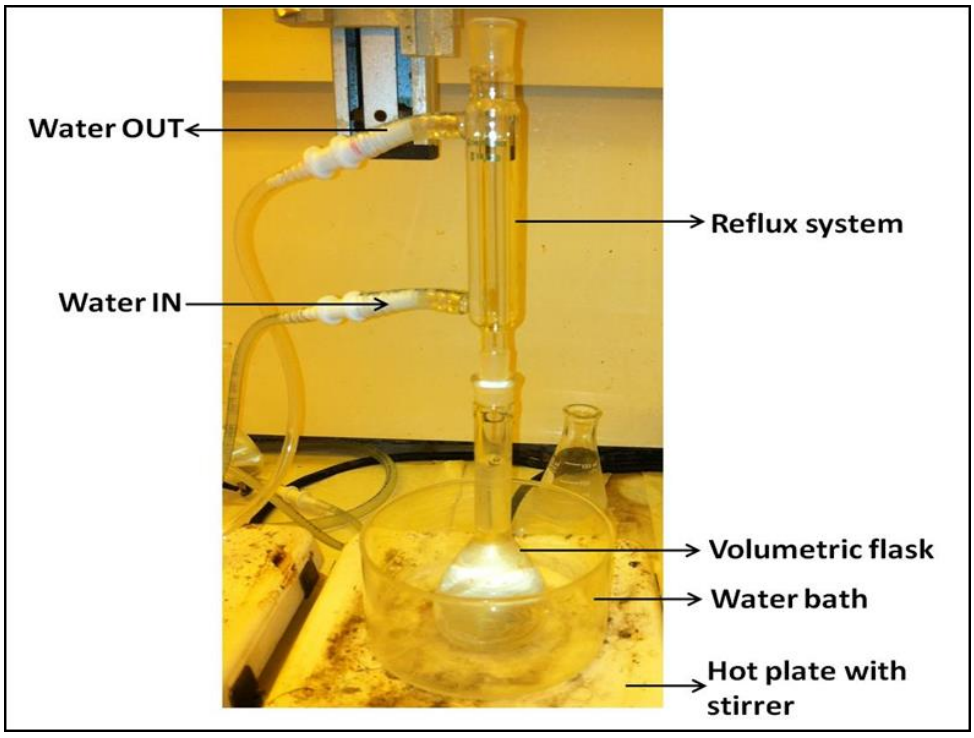


Figure 5.1 The reflux setup used for the synthesis of the dilithium ternary orthosilicates via the sol-gel process.

first is to let the chemical reactions resulting in the final silicate material to proceed during the synthesis; second is to act as a pyrolyzed carbon source during the calcination process. This carbon coating on the cathode particles is crucial for the battery's electrochemical performance since it enhances the conductivity inside cathode, as confirmed by the previous studies [114,147]. The final product was further ground manually using a porcelain mortar and pestle to obtain fine particles and was stored in an Ar-filled vial.

The DTS powder was then used to form a suspension in acetone; ultrasonicated, centrifuged, and drip-coated onto the MWCNT/graphite substrate, resulting in the final version of the cathode. Initially, two different cathode materials, $Li_2(Fe_{0.5}Mn_{0.25}Co_{0.25})SiO_4$ and $Li_2(Fe_{0.8}Mn_{0.1}Co_{0.1})SiO_4$ with high and low stoichiometric ratios of Fe, were synthesized and used to fabricate LIB cells DTS#1 and DTS#2, respectively. Then, to better understand the role of Fe on the electrochemical performance of the DTS cathode, two other cathode materials, $Li_2(Fe_{0.6}Mn_{0.2}Co_{0.2})SiO_4$ and $Li_2(Fe_{0.7}Mn_{0.15}Co_{0.15})SiO_4$, were synthesized and employed in the fabricated LIB cells DTS#3 and DTS#4, respectively. The net DTS cathode material masses for the LIB cells DTS#1-4 are 2, 2, 1.9, and 1.1 mg, respectively.

The Li-ion cells were fabricated in a dry atmosphere of Ar-filled 'glove-bag'. A 19 mm wide and 750 µm thick Li-foil was used as the anode, isolated from the cathode via the separator. An organic electrolyte, 1 M $LiPF_6$ salt dissolved in DMC:EC (1:1 vol. %) solvents, was used. After wetting the active cathode area with the electrolyte, separator and Li-foil were stacked on the cathode, and the Ni tabs were overlaid onto the electrodes. The sandwich of

electrodes was placed into the pouch cell package, then sealed with an impulse heat sealer. Afterward, the electrolyte was injected into the package, and the small opening was sealed, completing the assembly of 'coffee bag' type LIB cell, as displayed in Figure 5.2.

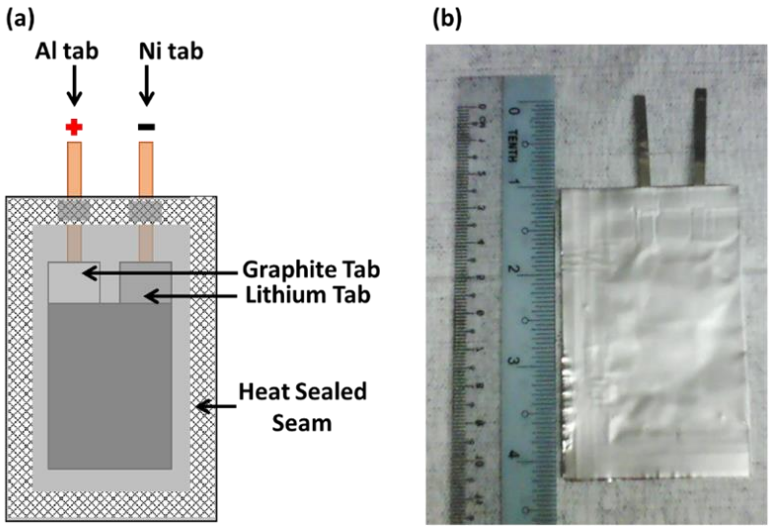


Figure 5.2 (a) The LIB cell in pouch cell configuration schematic, and (b) the assembled battery cell.

### 5.1.3. Material Characterization- SEM, ICP-MS, XPS, and XRD

A Hitachi S-4200 SEM was used to capture the scanning electron microscope images of the synthesized CNTs and DTS particles. The structural characterization of a novel cathode material also requires identification of its crystalline phases, which also allows determining the lithium intercalation mechanism. It can be achieved by observing the XRD pattern of the cathode material, which is unique due to the arrangements of the material's atoms in its crystal unit structure. The X-Ray diffraction experiments presented here were

performed on a Philips X'pert system with Cu K-α radiation at the wavelength of 1.54056 Å. The data acquisition was performed at 2θ = 15$^{o}$- 90$^{o}$, with a dwell time of 4 s/step, and a step size of 0.01$^{o}$.

Figure 5.3 shows typical SEM images of vertically aligned, ~7 µm tall MWCNTs grown on graphite, obtained at different magnifications. The first samples of the DTS materials, $Li_2Fe_{0.5}Mn_{0.25}Co_{0.25}SiO_4$ and $Li_2Fe_{0.8}Mn_{0.1}Co_{0.1}SiO_4$, were ground after calcination, and investigated in SEM, as Figure 5.4 shows. The grinding process appears to be inadequate for getting a uniform and small particle size distribution, which is very important for the even deposition of the particles into the CNT network, and for the electrochemical performance analysis. Therefore, all of the synthesized DTS materials were centrifuged before depositing them onto the cathode substrates. Figure 5.5

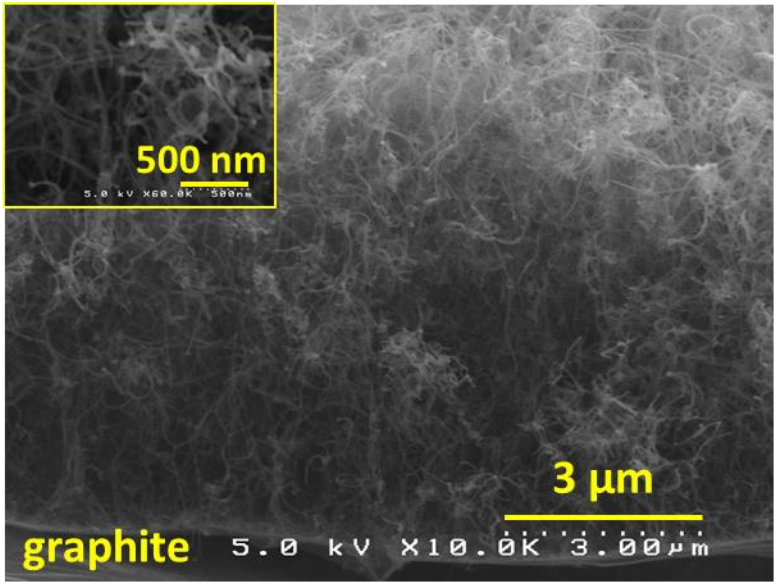


Figure 5.3 SEM image of the vertically aligned CNTs grown on graphite foil; inset- high-resolution SEM micrograph of the CNTs.

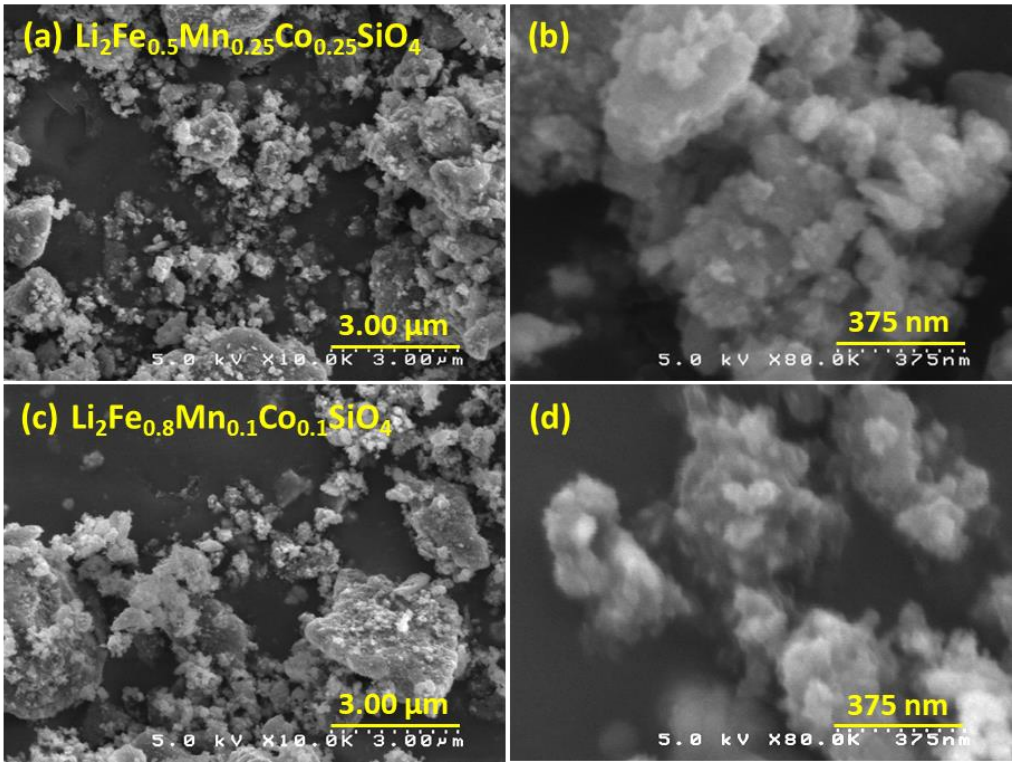


Figure 5.4 Low (a) and high (b) magnifications of the as-synthesized and ground DTS particle $Li_2Fe_{0.5}Mn_{0.25}Co_{0.25}SiO_4$. The relevant SEM analysis of $Li_2Fe_{0.8}Mn_{0.1}Co_{0.1}SiO_4$ is present in (c) and (d).

displays the high-resolution SEM micrographs of the active cathode particles

(DTS) incorporated into CNTs for the LIB cell DTS#4's cathode.

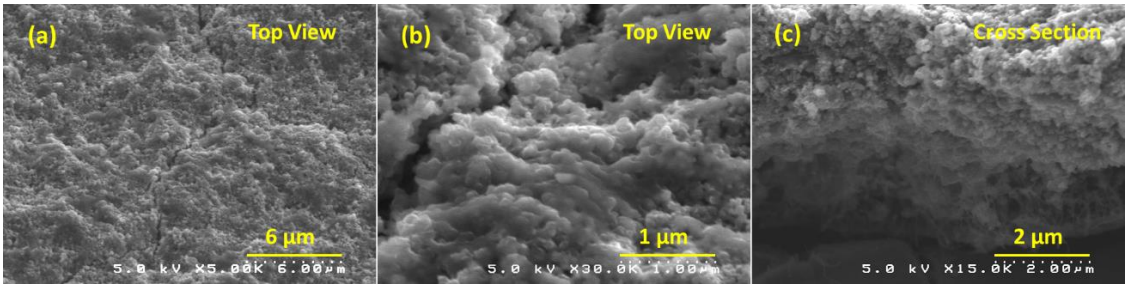


Figure 5.5 SEM micrographs of the DTS - $Li_2(Fe_{0.7}Mn_{0.15}Co_{0.15})SiO_4$, obtained after the centrifugation step, coated onto the CNT/graphite cathode (a) and (b) taken from the top view showing the uniform particle size distribution; (c) taken from the tilt-view cross-section showing the incorporation of nanoparticles into CNTs.

The chemical composition of the as-synthesized dilithium ternary orthosilicate ($Li_2Fe_{0.7}Mn_{0.15}Co_{0.15}SiO_4$) powder was confirmed by the Agilent 7500ce Inductively Coupled Plasma-Mass Spectrometry (ICP-MS). The ICP-MS technique involves a high-temperature ICP source to ionize the specimen's atoms first, then to separate and detect them with a mass spectrometer. Figure 5.6 shows the schematic representation of an ICP source in an ICP-MS device [148]. When the sample aerosol is introduced into the IC torch, the elements in the aerosol are first gasified and then ionized towards the end of the plasma. Later,

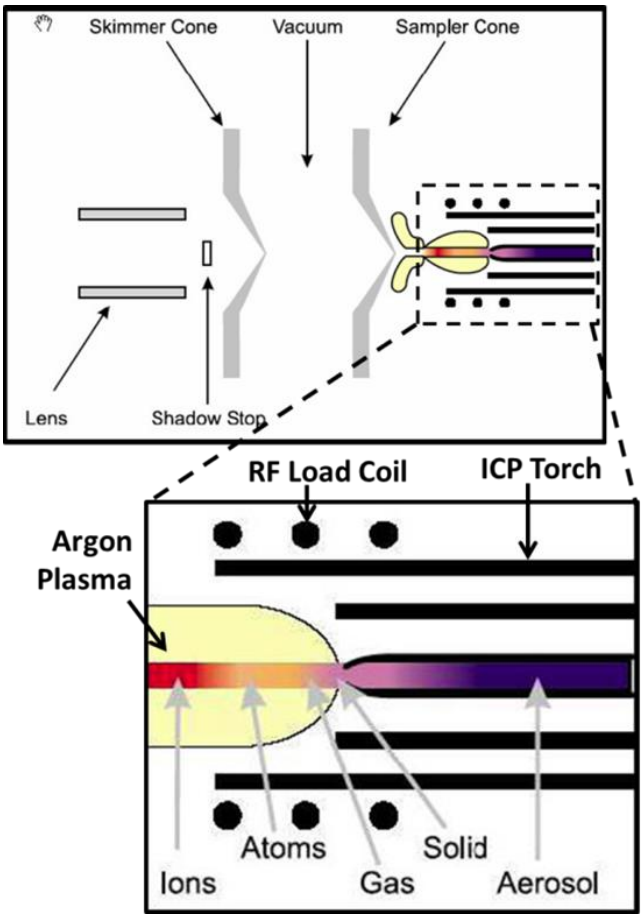


Figure 5.6 Schematic representation of the ICP-MS system, with a blow-up showing the ICP source in greater detail [148].

these ions are transferred into the mass spectrometer via the interface cones and separated by their mass-to-charge ratio. The ICP-MS experiment conducted on $Li_2(Fe_{0.7}Mn_{0.15}Co_{0.15})SiO_4$ revealed the concentrations of Fe, Mn, Co, Li, and Si in Table 5.1 as 13.54%, 3.251%, 2.328%, 5.009%, and 7.655%, respectively. Based on this, the formula of the dilithium ternary silicate cathode material is calculated as $Li_{2.11}Fe_{0.71}Mn_{0.17}Co_{0.12}Si_{0.8}O_4$, which is very close to the intended formula. The designed material is isostructural to $Li_2FeSiO_4$ and $Li_2MnSiO_4$. The XRD patterns of $Li_2(Fe_xMn_yCo_z)SiO_4$ ($x + y + z = 1$) with different stoichiometric ratios of Fe ($x = 0.5$, 0.6, 0.7, and 0.8), generated after data smoothing (Savitzky-Golay algorithm), are shown in Figure 5.7. The peak list of $Li_2(Fe_{0.7}Mn_{0.15}Co_{0.15})SiO_4$ is also presented in Table 5.2. It can be inferred that the structure does not have similar peaks with $Li_2FeSiO_4$, which is orthorhombic and belongs to the space group $Pmn2_1$, as Nyten et al. previously reported [149]. The reason for this might be due to the inadequate amount of catalytic reactions, as compared to other works for the $Li_2MSiO_4$ synthesis, where $OH^-$ anions were employed as the catalyst [150-152]. The high-intensity central peak at $2\theta = 45^o$ as well as the peaks at $65^o$ and $82^o$ are also due to fcc-Fe impurities. However,

Table 5.1 Results from the ICP-MS analysis of the dilithium ternary orthosilicate $Li_2(Fe_{0.7}Mn_{0.15}Co_{0.15})SiO_4$.

| | **Li** | **Fe** | **Mn** | **Co** | **Si** |
|---|---|---|---|---|---|
| **Concentration (%)** | 5.009 | 13.540 | 3.251 | 2.328 | 7.655 |
| **Atomic Mass (g/mole)** | 6.941 | 55.845 | 54.938 | 58.933 | 28.086 |
| **Atomic Ratio (%)** | 2.11 | 0.71 | 0.17 | 0.12 | 0.80 |

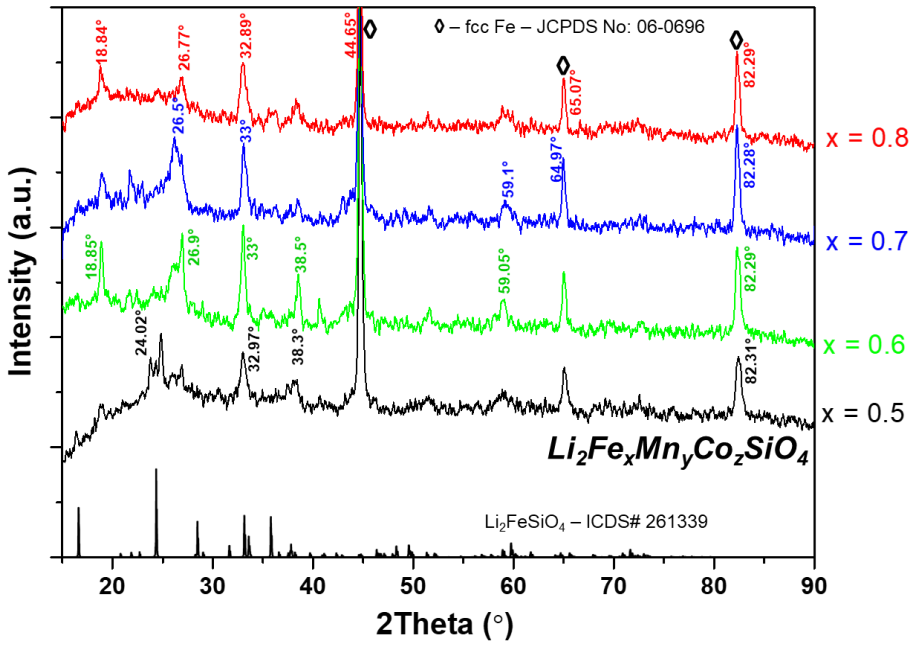


Figure 5.7 X-Ray Powder Diffraction spectrum of the dilithium ternary orthosilicate materials $Li_2(Fe_xMn_yCo_z)SiO_4$ (x + y + z = 1) (x = 0.5, 0.6, 0.7, 0.8, and y = z) with Cu K-α radiation.

considering there is a high amount of Fe impurity, causing a considerably high amount of diffraction peaks in our designated materials, the highest three peaks of $Li_2FeSiO_4$ were also observed in our $Li_2(Fe_{0.5}Mn_{0.25}Co_{0.25})SiO_4$ and

Table 5.2 List of the XRD peaks for $Li_2Fe_{0.7}Mn_{.15}Co_{0.15}SiO_4$.

| Peak List | | | | | | | |
|---|---|---|---|---|---|---|---|
| No. | 2-theta (deg) | d(ang.) | Height (cps) | FWHM (deg) | Int. I (cps deg) | Int. W(deg) | Asym. factor |
| 1 | 26.50(11) | 3.361(14) | 167(13) | 2.03(19) | 602(30) | 3.6(5) | 2.2(7) |
| 2 | 33.03(3) | 2.710(2) | 190(14) | 0.55(4) | 125(8) | 0.66(9) | 0.58(12) |
| 3 | 44.639(4) | 2.02830(19) | 2658(52) | 0.178(7) | 731(8) | 0.275(8) | 1.09(13) |
| 4 | 58.97(13) | 1.565(3) | 59(8) | 0.94(15) | 64(12) | 1.1(4) | 0.3(2) |
| 5 | 64.97(2) | 1.4343(4) | 322(18) | 0.16(3) | 96(6) | 0.30(4) | 1.5(10) |
| 6 | 82.284(19) | 1.1708(2) | 439(21) | 0.31(2) | 187(8) | 0.43(4) | 1.6(5) |

$Li_2(Fe_{0.6}Mn_{0.2}Co_{0.2})SiO_4$ materials at 2θ = 17º, 24º, and 33º, as Figure 5.7 shows. The cathode material $Li_2(Fe_{0.6}Mn_{0.2}Co_{0.2})SiO_4$ also has a peak at 2θ = 36º, which is the fourth highest peak of $Li_2FeSiO_4$.

## 5.2. Electrochemical Characterization

The electrochemical charge-discharge experiments of the LIB cells DTS#1 and DTS#2 were performed using the Vencon-UBA5 battery analyzer; DTS#3 and DTS#4 were charged-discharged using CHI660C potentiostat with a computerized data acquisition system. The potentiostat was also used for the AC impedance experiments.

AC impedance measurements were done in the frequency range between 17 Hz and 100 kHz at an AC amplitude of 5 mV. According to Figure 5.8, the as-fabricated LIB cell DTS#4's electrical contact resistance is ~2 Ω, and the polarization resistance is ~120 Ω, due to the uniform particle size distribution of DTS particles and their accommodation onto CNT forest. After the 1$^{st}$ cycle, the polarization resistance increases to ~180 Ω due to solid electrolyte interphase (SEI) formation on the electrodes.

Initially, the LIB cells DTS#1 and DTS#2 were charged and discharged in the voltage window of 1.8 V to 4.7 V since the charging voltage settled at a maximum of ~4.7 V, as shown in Figure 5.9. Since the cells did not reach the target voltage (4.7 V) at low currents during charging, a higher charge current (4.5 C) was used. The current rates during discharge were kept at 0.93 C for both cells. At the charging step, the voltage first reached 4.7 V and then dropped

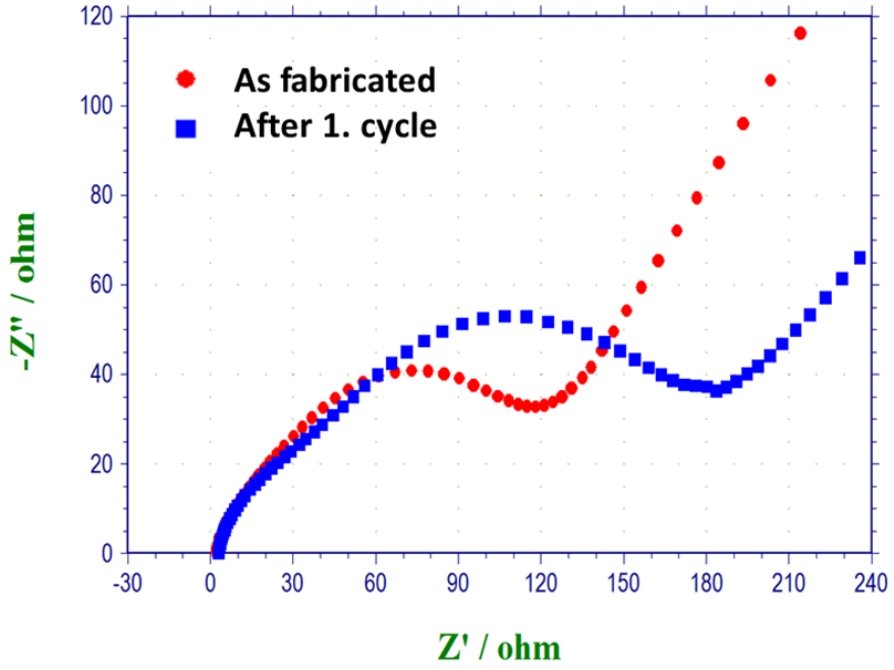


Figure 5.8 Nyquist plot of the AC impedance tests between the frequency range 100 kHz and 17 Hz for the LIB cell DTS#4 before and after the 1st charge-discharge cycle.

to 4.3 V and 4.5 V for DTS#1 and DTS#2, respectively. This voltage behavior is due to the switching from constant-current charging to constant-voltage charging (4.7 V) in the battery analyzer, which had a poor current resolution.

Discharge capacities obtained from DTS#1 and DTS#2 were 193 µAh and 363 µAh, respectively. While the discharge profile for DTS#1 mostly maintained a slope down to ~2.2 V, DTS#2 had a plateau-like profile from 4.2 V to 3.9 V, which will be explained later. A similar voltage profile below 2.2 V to 1.8 V with a reduced slope was observed in both cells, which might be due to the multi-phase transformations involving the delithiated-phases of the DTS material. A similar effect was also observed by the other researchers who used $Li_2FeSiO_4$ or

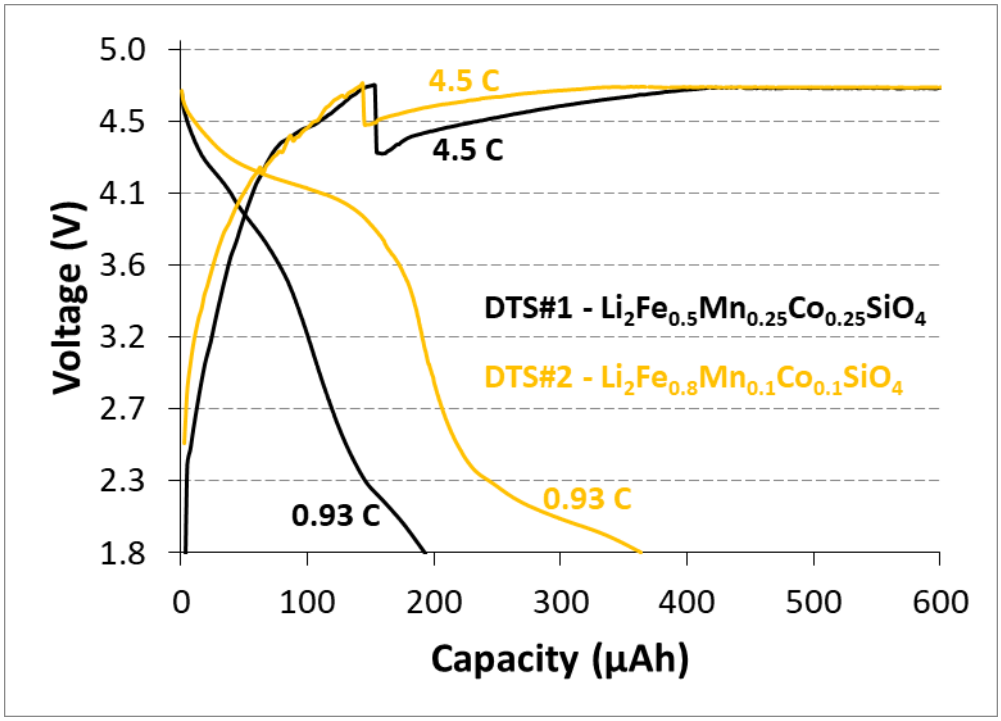


Figure 5.9 Charge-discharge curves of the LIB cells DTS#1 and DTS#2, which have active cathode materials $Li_2(Fe_{0.5}Mn_{0.25}Co_{0.25})SiO_4$ and $Li_2(Fe_{0.8}Mn_{0.1}Co_{0.1})SiO_4$, respectively.

$Li_2MnSiO_4$ cathode material in their LIB cells [146,153,154]. From Figure 5.9, it is obvious that the LIB cell DTS#2 yielded a higher discharge capacity than that of DTS#1, which is possibly due to the lower electronic conductivity and the lower stability of the silicate material $Li_2(Fe_{0.5}Mn_{0.25}Co_{0.25})SiO_4$ with higher Mn concentration [146].

On the other hand, charge-discharge tests of the LIB cells DTS#3 and DTS#4 were performed in the voltage window of 1.8 V - 4.9 V, to utilize more of $Fe^{2+}\leftrightarrow Fe^{4+}$, $Mn^{2+}\leftrightarrow Mn^{4+}$ and $Co^{2+}\leftrightarrow Co^{4+}$ transitions. Figure 5.10 shows the unidentical charge-discharge curves of the cells DTS#3 and DTS#4. At the beginning of the charging, the voltage of DTS#3 ascends to 3.3 V rapidly due to charge polarization. Between 3.3 and 4.1 V, the voltage profile follows a small-

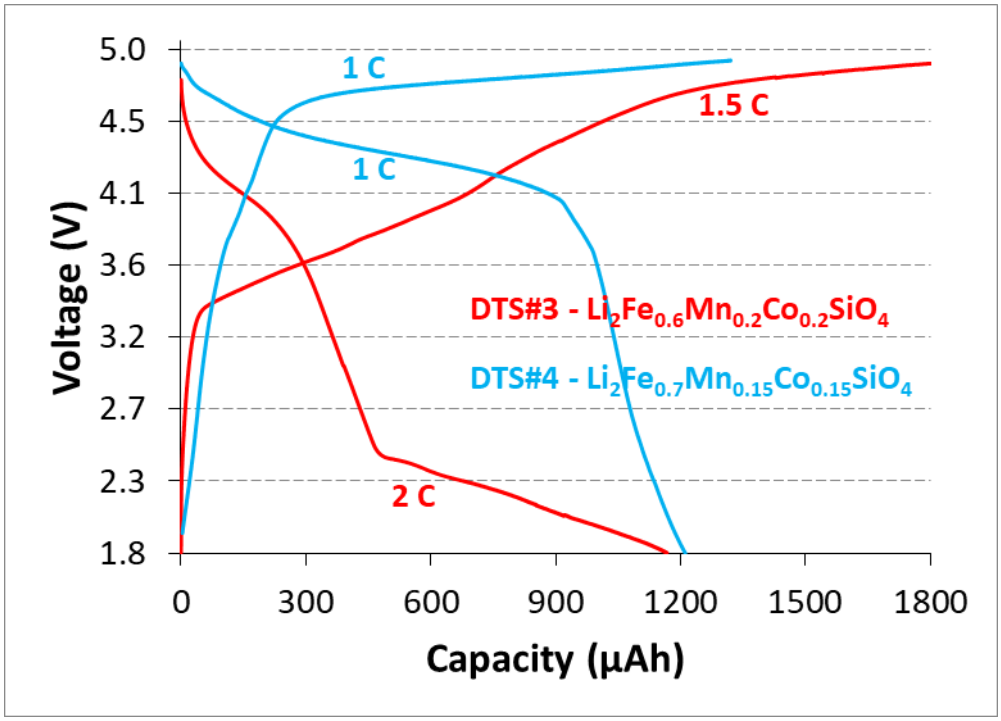


Figure 5.10 Charge-discharge curves of the LIB cells DTS#3 and DTS#4 with active cathode materials $Li_2(Fe_{0.6}Mn_{0.2}Co_{0.2})SiO_4$ and $Li_2(Fe_{0.7}Mn_{0.15}Co_{0.15})SiO_4$, sequentially.

sloped line, due to $Fe^{2+}/Fe^{3+}$ transition in the DTS material. At voltages above 4.1 V up to 4.9 V, $Mn^{2+}/Mn^{3+}$, $Co^{2+}/Co^{3+}$, and $Fe^{3+}/Fe^{4+}$ transitions are expected to occur in the cathode of the DTS#3 cell. At the discharge step, between ~4.2 and 3.8 V, the voltage drops following a small-slope line, followed by a sharp decline to 2.4V, and then a small-sloped voltage profile down to 1.8 V. The discharge profile of DTS#3 cell is at lower potentials than the charge profile. Besides the polarization effect, this is due to the structural changes occurring in the DTS material after the delithiation. For example, it was previously shown that the volume of the unit cell of $Li_2FeSiO_4$ expands to $LiFeSiO_4$ upon delithiation [155], which causes the strength of the interatomic bonds in the DTS material to alter, thus resulting in the shift of the lithium insertion voltage during discharge. In

Table 5.3, charge-discharge currents, voltage window, and discharge capacities of DTS#1-4 are listed. After the cell DTS#4 is charged to 1320 µAh, it yielded a discharge capacity of 1210 µAh at 1 C current rate (363 µA). If we consider DTS as the only electrochemically active material in our cathode structure, both charge and discharge specific capacities (1200 mAh/g, and 1101 mAh/g, respectively) exceed the theoretical capacity (330 mAh/g). The average voltage measured is 4.25 V. However, based on the previous studies, it is expected that there is a contribution to the capacity from graphite (~120 mg), into which $PF_6^-$ anions might intercalate above 4.3 V [156,157]. Inside their dual carbon cell, Seel and colleagues obtained 140 mAh/g specific discharge capacity between 3.5 and 5.45 V, while Read reached 120 mAh/g between 4 and 5.2 V. Accordingly, our LIB cell demonstrated a hybrid performance, employing both $Li^+$ and $PF_6^-$ ions – i.e., lithium-ion and anion intercalation. During the charge, in the potential window of 1.8 to 4.4 V, $Li^+$ ions deintercalate from DTS and migrate towards the Li anode; simultaneously, $PF_6^-$ anions migrate towards the cathode and accumulate in the CNT forest. The high surface area of the VACNTs also allows a large

Table 5.3 Charge-discharge test results of the LIB cells DTS#1-4.

| **LIB Cell** | **Fe:Mn:Co Ratio in Cathode** | **Charge Current (mA) / C rate** | | **Discharge Current (mA) / C rate** | | **Voltage Window (V)** | **Cathode Area ($cm^2$)** | **Cathode Material Mass (mg)** | **Discharge Capacity (µAh)** |
|---|---|---|---|---|---|---|---|---|---|
| **DTS#1** | 2:1:1 | 3 | *4.5* | 0.61 | *0.93* | 1.8 - 4.7 | 1.5 x 2 | 2 | 193 |
| **DTS#2** | 8:1:1 | 3 | *4.5* | 0.61 | *0.93* | 1.8 - 4.7 | 1.5 x 2 | 2 | 363 |
| **DTS#3** | 3:1:1 | 1.25 | *1.5* | 0.94 | *2* | 1.8 - 4.9 | 4 x 1.9 | 1.9 | 1167 |
| **DTS#4** | 4.7:1:1 | 0.36 | *1* | 0.36 | *1* | 1.8 - 4.9 | 4 x 1.9 | 1.1 | 1210 |

amount of $PF_6^-$ to accumulate at the cathode. At potentials beyond 4.4 V, besides further deintercalation of $Li^+$ from the DTS, $PF_6^-$ anions start intercalating into the graphite. Most of these $PF_6^-$ intercalation happens in a single phase, as confirmed by the constant slope (dq/dV) charge curve between ~4.7 and 4.9 V. During the discharge, these processes reverse: $Li^+$ ions intercalate into the DTS-host structure, and $PF_6^-$ ions deintercalate from the graphite and migrate to the bulk electrolyte. Although the discharge capacity contribution of the DTS material and graphite cannot be separated for DTS#4, yet it is possible for the LIB cell DTS#3. As shown in Figure 5.10, the discharge profile of DTS#3 from 2.4 V to 1.8 V can be mostly attributed to the lithium intercalation into the DTS host structure. The gravimetric specific discharge capacity of the DTS material in this voltage range is ~361 mAh/g, which is very close to the theoretical capacity (330 mAh/g) of the DTS material, and indicating two-lithium intercalation reactions taking place in the cathode. In addition, this specific capacity is the highest obtained for a LIB cathode material so far.

The cycling data of the LIB cell DTS#4 shows a stable performance in 100 consecutive charge-discharge cycles at 363 µA, with no capacity fade, and efficiencies above 90%, as Figure 5.11 illustrates.

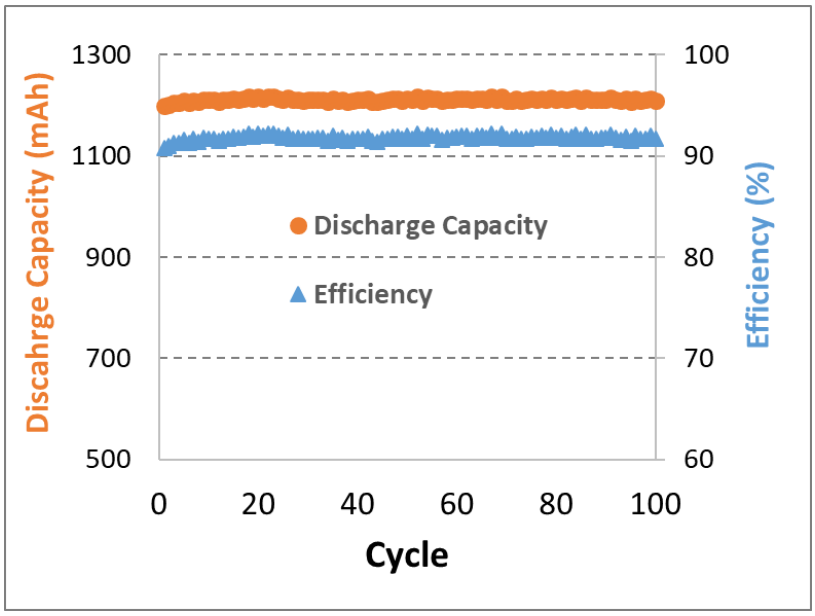


Figure 5.11 Cycling performance of the LIB cell at 363 µA for 100 consecutive charge-discharge cycles.

## 5.3. Summary

- A new cathode material, utilizing dilithium ternary silicate, $Li_2Fe_xMn_yCo_zSiO_4$ (x + y + z = 1) was synthesized and structurally characterized.
- Dilithium Ternary Silicate materials with different Fe:Mn:Co ratios (2:1:1, 3:1:1, 4.7:1:1, and 8:1:1) were synthesized and coated on CNTs that were grown on graphite substrates. The resultant carbon-based nanocomposite cathodes were characterized for LIB applications.
- Hybrid performance of the LIB cells was observed with the intercalation/deintercalation of $Li^+$ and $PF_6^-$ ions during galvanostatic charge/discharge tests.

- The results suggested that even though a structurally pure DTS material could not be synthesized, we were able to achieve a specific discharge capacity (361 mAh/g) very close to theoretical capacity between 2.4 and 1.8 V, which is an indicator of two-lithium intercalation reactions.
- Our LIB cell, DTS#4, was able to operate at potentials higher than 4 V and had a stable cycle life while employing a hybrid storage performance.

# CHAPTER VI

# MICROPATTERNED CNTS ON ALUMINUM AS A LIB CATHODE HOST

This chapter covers the work done to develop a novel cathode host: micro-array patterned CNTs on aluminum (MA-CNT/Al) for the LIBs. The new substrate was used to deposit a commercial active cathode material, lithium iron phosphate (LFP), via electrophoresis and vibration-assisted drip-coating, and was structurally characterized using SEM. Electrochemical performances of the cathodes fabricated using both of the material deposition techniques were also compared.

## 6.1. Fabrication of the Lithium Iron Phosphate/MA-CNT cathode

Aluminum has been a popular current collector/substrate material for batteries and supercapacitors due to its electrical conductivity, mechanical strength, and relative abundance in the earth's crust. Growing CNTs directly onto the surface of Al substrate lowers the internal resistance and the charge transfer resistance between the electrode and the electrolyte [158]. However, it has been challenging to grow CNTs on Al substrate due to Al's low melting point of 660 $^{o}$C. Others have been able to grow varying heights of CNTs on Al using complex processing techniques with exotic catalysts and unique CVD systems [158-161]. To

the best of our knowledge, no one has successfully demonstrated the VACNT synthesis on Al substrates, especially the micropatterned arrays using a simple HFCVD system with $CH_4$ as the carbon source gas [36].

Aluminum stock consisting of 127 μm thick foil of Al alloy 1145 (99.45% Al) was purchased from McMaster-Carr. As the active cathode material, lithium iron phosphate ($LiFePO_4$, or LFP) powder was purchased from MTI Corporation. Sample weight measurements were made on Denver Instrument's APX-100 microbalance. The power source used for electrophoretic deposition was Keithley 6517A Electrometer. A polypropylene (Celgard) film with 39% porosity and 25 μm thickness was used as the separator and was procured from MTI Corporation. The battery cell was assembled in a VTI Super (Gloucester, MA) glovebox filled with Ar as the working gas with $H_2O$ and $O_2$ levels maintained at below 0.1 ppm. Previously cut Al-foil discs (with a diameter of 2cm) were first cleaned with acetone and methanol, followed by drying on a 100 $^oC$ hot plate. Micropatterning of the CNTs on Al substrates was achieved using the same methods described in Chapter 3.

The synthesis of the vertically aligned CNTs on Al was carried out in the HFCVD system using the same recipe outlined in Chapter 3, with some parameters fine-tuned. Differently, the substrate was positioned 40 mm below the W-filament, and the filament temperature was set to 2100 $^oC$ during the CNT synthesis. After the CNT growth step for 15 min, the sample was cooled down to room temperature under $H_2$ ambient.

The LFP particle size distribution was obtained from the website of the LFP material's vendor; as Figure 6.1 shows, the peak particle size is ~6-7 μm,

with a D50 of 3.5 +/- 1 µm and D90 of < 15 [162]. Based on this analysis, it was determined that most of the particles exceeded the distance between the adjacent MWCNTs (~75 nm) and would not disperse into the CNTs effectively. To address this issue, we dried the as-received LFP powder under Ar at 125 $^{o}$C for 2 h and ball-milled to obtain finer particles. The cathode powder was then dispersed into acetone, ultrasonicated, and centrifuged, in order to retain only the fraction of smaller-sized particles. Using this suspension with different material deposition techniques, two different cathodes, thus two different battery cells were fabricated: Cell#1 with the cathode using vibration-assisted drip-coating and Cell#2 with the cathode using electrophoretic deposition.

A simple Al-foil based container was first fabricated with two 3 V DC micro-motors mounted on the side walls to hold the CNT/Al substrates on the heater while providing the vibrations while making Cell#1 cathodes. The LFP/acetone suspension was drip-coated with a pipette onto a 1.5 cm$^2$ micropatterned CNT/Al substrate on the heater (~80 $^{o}$C), resulting in a net 0.6 mg

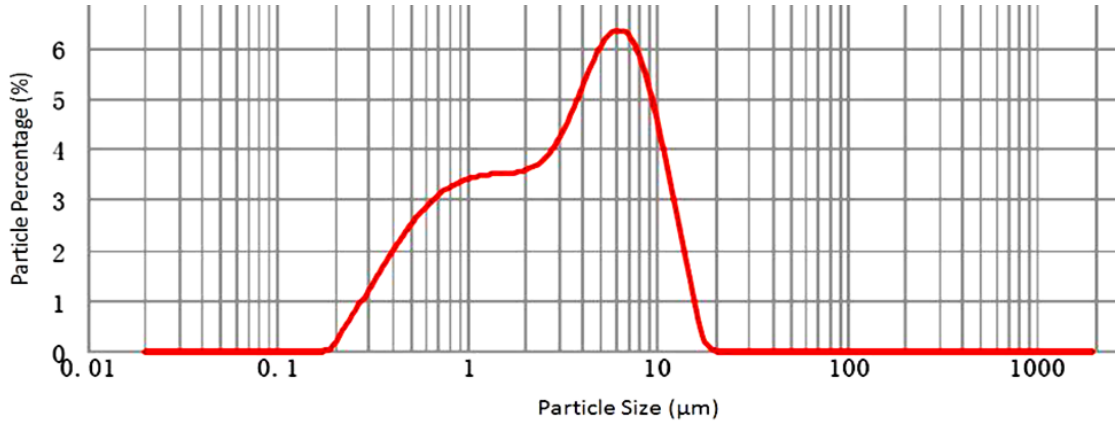


Figure 6.1 Particle size distribution of as received $LiFePO_4$ powder [162].

LFP coating. The acetone acted as the carrier medium for transporting the particles into the CNT network before evaporating. The electrophoretic deposition of LFP for Cell#2 electrode was performed in a parallel plate configuration without any supporting electrolyte. The CNT/Al substrate was mounted with a platinum foil counter electrode and a gap of ~13 mm in a beaker and filled with the LFP/acetone suspension. Under an applied electric field of ~1.9 kV/m using the power supply, the ferromagnetic LFP particles were uniformly coated onto the 3D CNT array structure, as represented in the schematic in Figure 6.2(a). Figures 6.2(b) and (c) also represent the perspective view of the micro-array patterned CNTs three-dimensionally, before and after the LFP particle coating, respectively. The mass of the LFP deposited on the electrode was calculated to be 0.4 mg.

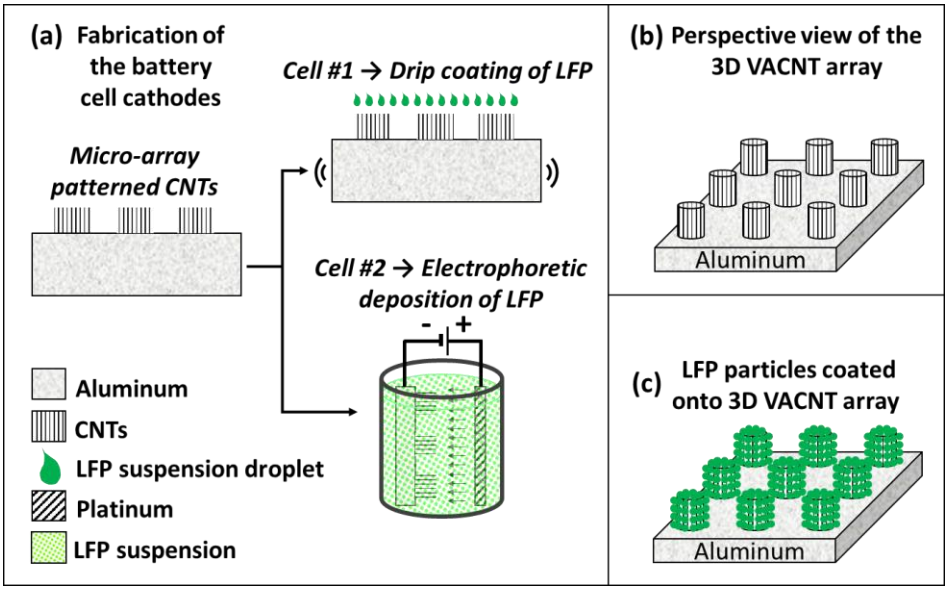


Figure 6.2 (a) Fabrication of Cell#1 and Cell#2 using vibration-assisted drip-coating and electrophoretic deposition, respectively; (b) Perspective view of the 3D CNT array on aluminum synthesized in an HFCVD system; (c) The 3D CNT array after LFP particles' deposition.

The LIB cells were then assembled in Swagelok cells inside the glove box. The electrolyte, consisting of 1 M $LiPF_6$ in DMC:EC (1:1 v/v), was used to wet the active area of the electrodes and the PP separator before assembling them with a ~1.9 cm diameter Li-foil anode. Electrochemical characterization was performed using constant-current charge-discharge and AC impedance spectroscopy techniques implemented in a CH Instruments Texas CHI 660C potentiostat, which is accompanied by its data acquisition software. The material analysis was done using a Hitachi S4200 scanning electron microscope to study the microstructure of the electrodes before and after LFP deposition.

Scanning electron micrographs in Figures 6.3(a) and (b) show the tilted view of the dense micropatterned vertically aligned CNT array on the Al substrates, which were used in Cell#1 and Cell#2, respectively. These arrays typically have CNTs with an average height of ~10 µm. In the insets of Figure 6.3, higher magnification SEM micrographs show the top view of the individual

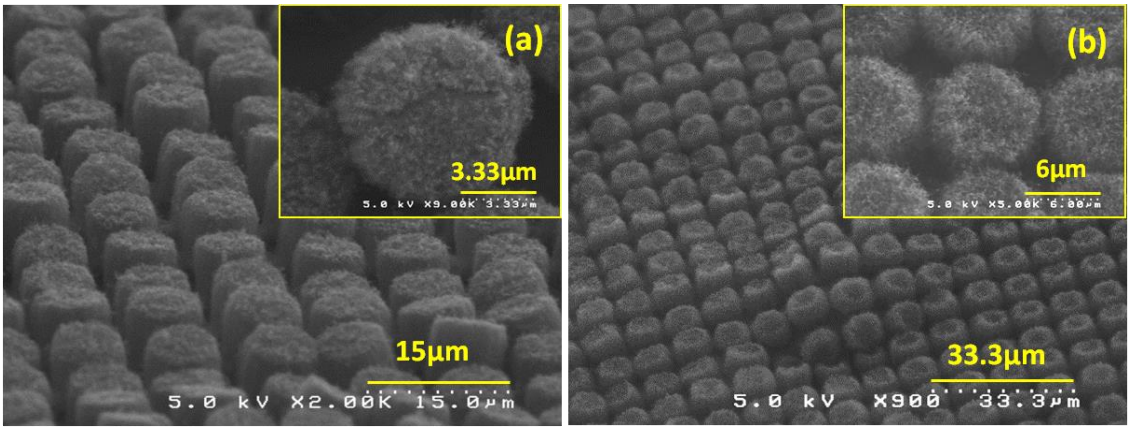


Figure 6.3 Tilted and top (inlets) SEM micrographs of vertically aligned, 9 µm-diameter patterned MWCNTs grown on Al, and used in Cell#1 (a), and Cell#2 (b).

CNT microelectrodes with a diameter of ~9 µm and a pitch of ~10 µm. The SEM micrographs recorded for the cathodes after the LFP coating using vibration-assisted drip-coating and electrophoretic deposition are shown in Figures 6.4(a) and (b), respectively. Higher magnification micrographs were also included in the inset of Figure 6.4. From these images, it is difficult to distinguish visually between the two cathodes, although, it is clear that the CNTs no longer retain their vertical alignment; they seem to have collapsed. This collapse can be attributed to the aspect ratio (height/diameter = ~1) of the CNT-array microelectrodes which may need to be modified to make them self-supporting and retain their vertical alignment even after the coating steps. Additionally, the capillary forces between the CNTs, when wet with acetone, cause contraction after the acetone evaporates, resulting in the final structures seen in Figure 6.4 [163-165]. Similar clustering effects have also been observed by the researchers when they exposed their vertical microstructures to liquids [163,166,167].

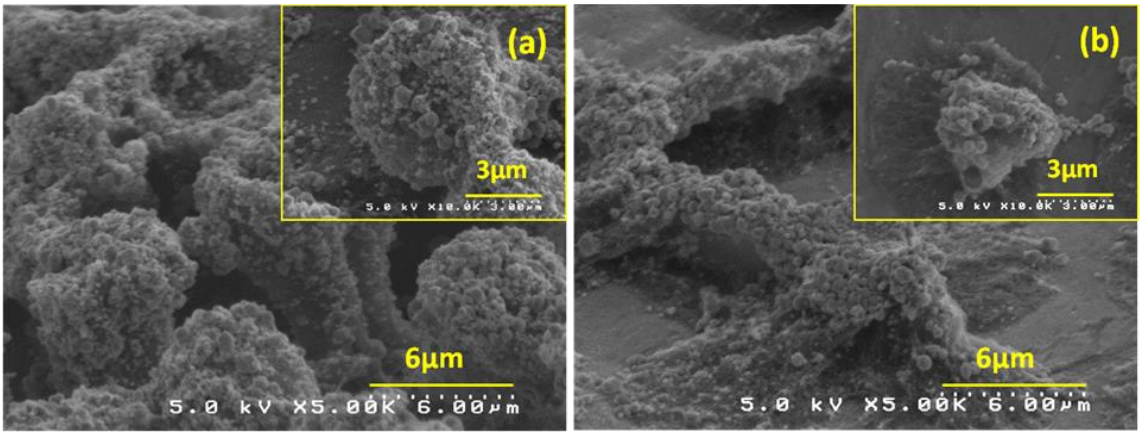


Figure 6.4 Tilted and top (inlets) SEM micrographs of the cathodes of Cell#1 and Cell#2 fabricated with (a) vibration-assisted drip-coating, and (b) electrophoretic deposition of $LiFePO_4$ nanoparticles onto micropatterned CNTs on Al, consecutively.

In Figure 6.5, X-ray diffraction (XRD) spectra of $LiFePO_4$ powder, which was obtained from the manufacturer's website, can be seen [162]. The well-separated diffraction peaks indicate that $LiFePO_4$ powder has a good crystallinity.

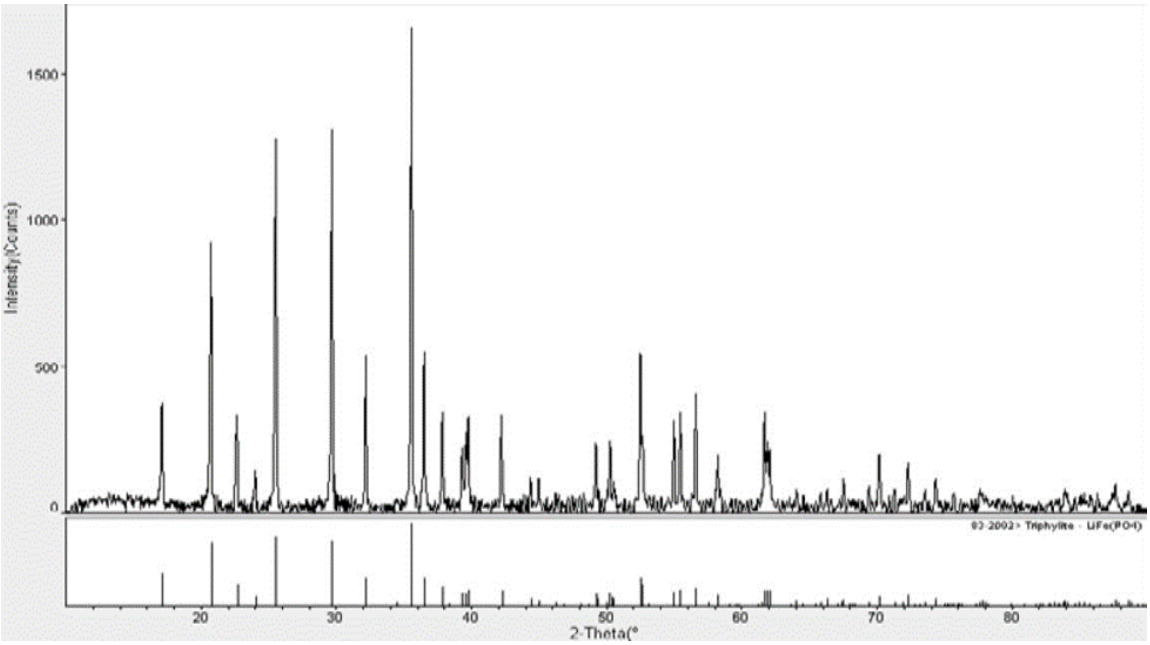


Figure 6.5 XRD pattern of the as-received $LiFePO_4$ powder [162].

## 6.2. Electrochemical Characterization

Galvanostatic charge-discharge tests were performed in the voltage window of 2 V - 4.5 V at the current rates of C/20, C/10, C/5, and C/2. The corresponding curves are overlaid in Figure 6.6. At the lowest C-rate tested, C/20, Cell#1 and Cell#2 yield gravimetric specific discharge capacities of 95 and 143 mAh/g, respectively. The corresponding values of gravimetric specific energy were calculated to be 302 and 486 Wh/kg, respectively. Cell#2's higher capacity can be related to relatively better bonding and thereby a better electrical contact

between the LFP nanoparticles and the CNTs achieved via electrophoretic deposition.

In contrast, the vibration-assisted drip-coating method was less efficient as observed during the fabrication process; the LFP nanoparticles tended to accumulate at the edge of the substrate, where the acetone dries faster, and the final structure resulted in a relatively weaker LFP-CNT bonding due to random physical adsorption of the powder. As mentioned previously, no differences were evident from the SEM micrographs, but they emerged during the electrochemical characterization. In the next cycle, at C/10, the specific capacities dropped to 76 and 126 mAh/g for Cell#1 and Cell#2, respectively. The effects of structural differences arising from the deposition techniques are more evident at a higher discharge rate of C/2, as illustrated in Figure 6.6, where the capacity decreases down to 54 and 99 mAh/g for Cell#1 and Cell#2, respectively. The importance of LFP-conductive carbon material bonding has been previously studied, highlighting its effect on the cyclability, Li+ diffusion rate, therefore high-power capability [90,110,168]. Results from the electrochemical characterization, i.e., specific

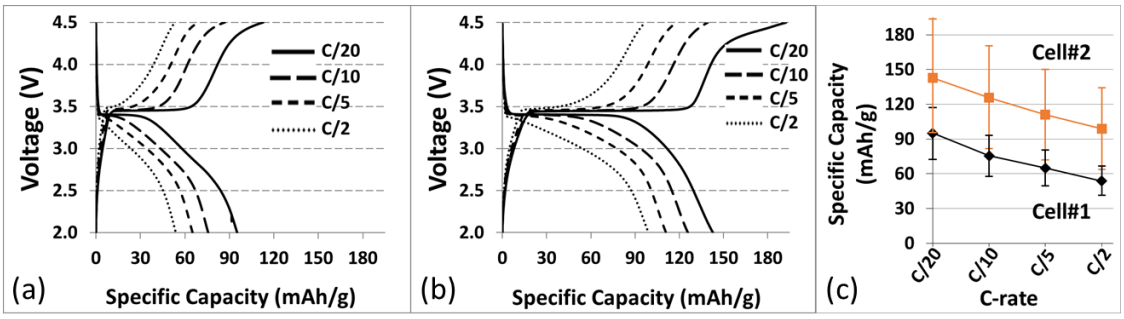


Figure 6.6 Charge-discharge curves of Cell#1 (a) and Cell#2 (b) at varying current rates (C/20 to C/2); (c) C-rate vs. specific discharge capacity of the cells with uncertainty bars.

capacity, specific energy, and specific power, obtained for the two cells are summarized in Table 6.1.

Nyquist plots were recorded using AC impedance spectroscopy in the frequency range of 1 Hz - 100 kHz with an AC amplitude of 5 mV. The spectra obtained for Cell#1 and Cell#2 after different charge-discharge cycles are overlaid in Figures 6.7(a) and (b), respectively. These results show that the polarization resistance ($R_p$) values for Cell#1 and Cell#2 increase from ~60 and 73 Ω before cycling to ~204 and ~165 Ω after more than ten cycles, respectively. The initial increase can be attributed to the formation of the solid electrolyte interface (SEI) on the electrodes. Based on the electrochemical dynamics inside the cell, an equivalent circuit is proposed, as seen in Figure 6.8, similar to Howey et al. work [169]. In this circuit, $R_e$ stands for the electrical resistance of the wires and the electrolyte, while $R_{ct}$ and $R_{SEI}$ represent the charge transfer and SEI

Table 6.1 Summary of electrochemical characterization results from Cell#1 (vibration-assisted drip-coating) and Cell#2 (electrophoretic deposition).

| LIB Cell | C rate | Specific Capacity (mAh/g) | Average Potential (V) | Specific Energy (Wh/kg) | Specific Power (W/kg) |
|---|---|---|---|---|---|
| **Cell#1** | 0.05 | 95.1 | 3.18 | 302.4 | 27.0 |
| | 0.1 | 75.6 | 3.09 | 233.6 | 31.5 |
| | 0.2 | 65.0 | 3.03 | 197.0 | 61.8 |
| | 0.5 | 53.8 | 2.94 | 158.2 | 149.9 |
| **Cell#2** | 0.05 | 142.8 | 3.40 | 485.5 | 28.9 |
| | 0.1 | 125.8 | 3.31 | 416.4 | 56.3 |
| | 0.2 | 111.0 | 3.21 | 356.3 | 109.1 |
| | 0.5 | 98.9 | 3.04 | 300.7 | 258.4 |

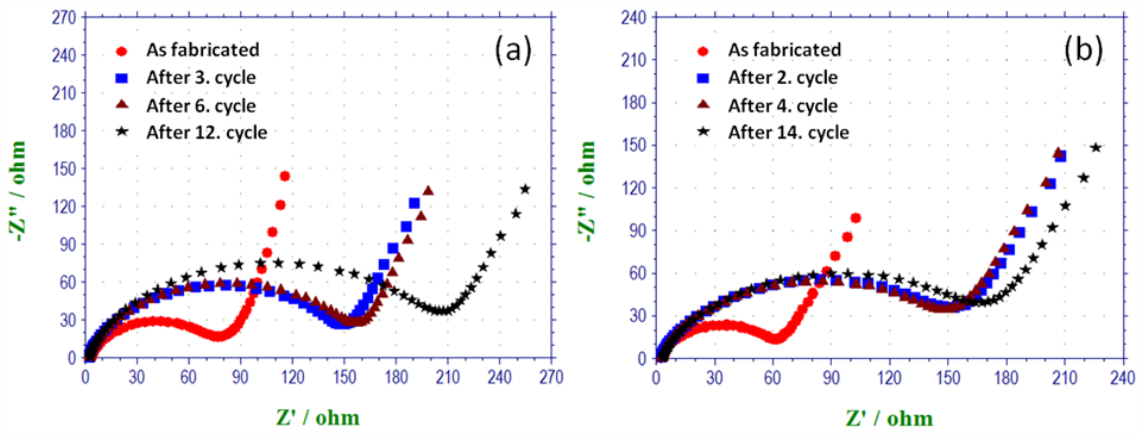


Figure 6.7 AC impedance spectroscopy scans of Cell#1 (a) and Cell#2 (b) before and after charge-discharge tests.

resistances, respectively, where $R_{ct} + R_{SEI} = R_p$ or the polarization resistance. In a LIB, $R_{ct}$ is accompanied by a double layer formation on the electrode surface just after the assembly of the cell. This double layer acts as an imperfect capacitor and can be represented by a constant phase element ($CPE_{dl}$). The impedance of a CPE was previously written in equation 3.1 of Chapter 3.

After the first cycle, the SEI layer forms on the electrodes, which acts as an electrical insulator but allows the diffusion of $Li^+$ ions. This diffusion through the SEI layer can be represented as another CPE ($CPE_{SEI}$) in parallel with $R_{SEI}$ in the circuit. In a Nyquist plot, the effects of the double layer and the SEI layer can be seen in the high and medium-frequency regions of the impedance spectrum, respectively, while in the low-frequency region, $Li^+$ diffusion at the electrode surface is dominant. At even lower frequencies, due to the high penetration depth of the AC signal (as compared to considerably low electrode pore length in porous materials), the electrode behaves as a quasi-planar surface, resulting in a capacitive response [170]. Therefore, the low-frequency region is seen as a straight

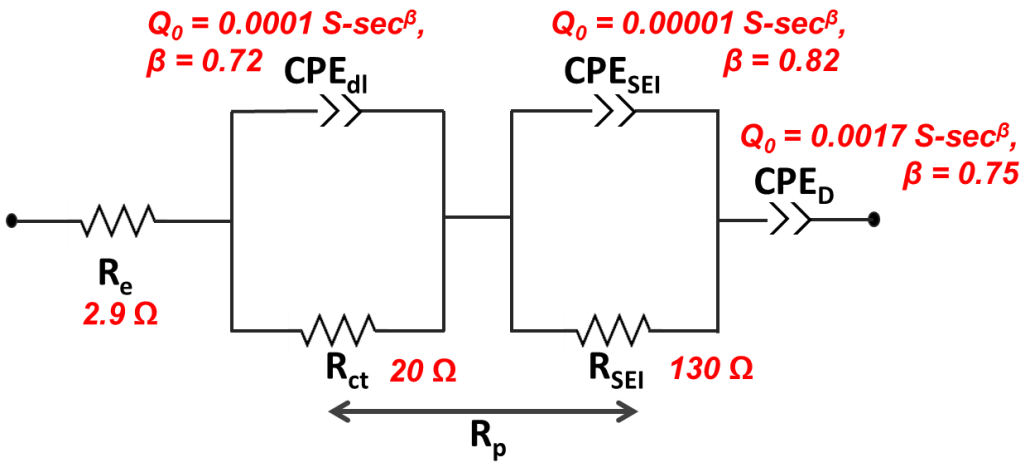


Figure 6.8 Equivalent circuit of a lithium-ion battery between cathode and anode. The values near each element correspond to the circuit whose impedance spectra is fitting to Cell#2's after the 2nd cycle.

line with a constant phase angle and represented by the CPE-diffusion ($CPE_D$) element in the equivalent circuit. We were able to achieve an excellent fit of the impedance spectrum from the model to the experimental data for Cell#2, as observed in Figure 6.9.

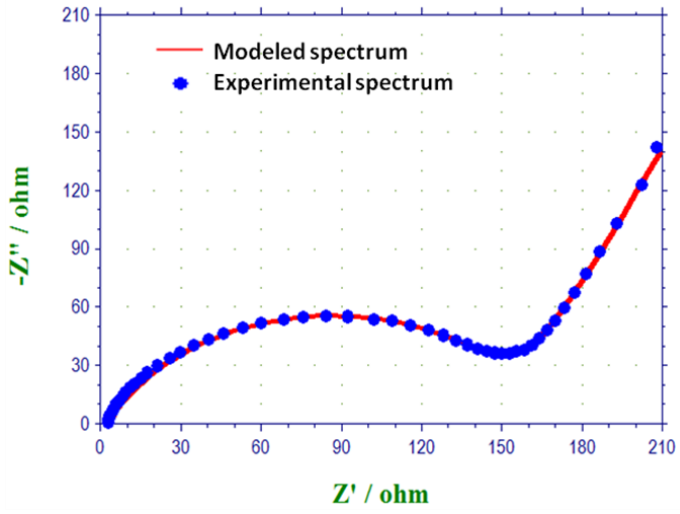


Figure 6.9 AC impedance spectrum of Cell#2 after 2nd charge-discharge cycle, in comparison with the equivalent circuit model's response.

The results demonstrated the strong potential of the application of vertically aligned CNTs on a conventional current collector (Al-foil) for developing LIB cathodes.

## 6.3. Summary

- A new energy storage cathode host consisting of micro-array patterned, vertically aligned CNTs on Al-foil was successfully fabricated after using $CH_4$ carbon precursor gas through the HFCVD process.
- LFP powder was used to demonstrate the viability of these 3D nanostructured CNT arrays as new cathodes, after being coated on them by two different techniques: electrophoresis and vibration-assisted drip-coating.
- Electrophoretic deposition produced a more stable cathode which yielded a higher specific capacity than the cathode prepared through the drip-coating method.
- The efficacy and simplicity of the electrophoretic deposition over the drip-coating method were evident from the higher specific capacity and stable performance, even at higher C rates.
- At low current rates, MA-CNT/Al was proven to be a very good candidate for a future conductive network of cathode materials.

# CHAPTER VII

# A NOVEL ADDITIVE-FREE CATHODE FABRICATION TECHNIQUE FOR A HIGH-ENERGY, HIGH-POWER LITHIUM-ION BATTERY

In this chapter, a novel technique to fabricate the Li-ion battery cathode, which involves the in-situ synthesis of the LFP material incorporated onto microarray patterned vertically aligned CNTs (MA-CNTs) on an aluminum substrate is described. Structural and material characterization of the binder and conductive additive-free cathode was detailed. Electrochemical charge-discharge and AC impedance spectroscopy measurements were conducted to better understand the cathode's energy storage and power capability in a LIB cell.

## 7.1. In situ Synthesis of $LiFePO_4$ on Vertically Aligned CNTs on Aluminum

### 7.1.1. Cathode Fabrication

For our experiments, a roll of Al-foil, which is 125 µm thick and consists of 1145 alloy (99.45 % Al) was purchased from McMaster-Carr. Initially, a circular Al (127 µm thick, Al alloy 1145) disc with ~2.2 cm diameter was cut, followed by cleaning with acetone and methanol, and drying on a 100 $^{o}$C hot plate. Micropatterning and the CNT growth processes were carried out similarly as in Chapter 6. Differently, the buffer and catalyst metal layer thicknesses on the Al substrate were 45 nm and 10 nm for Ti and Co, respectively. Besides, during the

CNT synthesis, the W filament temperature was set to 2100$^{o}$C, the substrate was kept 40 mm below the filament, and $CH_4$ was introduced into the HFCVD system for 15 min.

For the synthesis of the LFP material, Choi et al.'s recipe was used [104]. The precursor compounds, lithium acetate ($CH_3CO_2Li.2H_2O$), phosphorus oxide ($P_2O_5$), and lauric acid ($C_{12}H_{24}O_2$) were purchased from Alfa Aesar; iron chloride ($FeCl_2.4H_2O$) was purchased from Beantown Chemical. Synthesis of the LFP material and the battery assembly were made in a VTI Super (Glucoster, MA) Ar-filled glovebox ($H_2O$ and $O_2$ levels maintained at below 0.1 ppm). In our work, the precursor compounds, lithium acetate, iron chloride, phosphorous oxide, and lauric acid were dissolved separately in ethanol in the glove box. In this recipe, the role of lauric acid is to control the morphology of the final LFP particles, as a surfactant. First, 1 M iron chloride and 1 M phosphorous oxide solutions were slowly mixed and stirred for 3 h. Afterward, 1 M lithium acetate solution was added to this solution, and stirred for an additional 3 h, followed by adding 0.5 M lauric acid solution into it slowly and stirring for 4 h. The final solution was anhydrous and suitable to be deposited into the hydrophobic CNT forest.

The LFP precursor solution was drip-coated onto the MA-CNT/Al substrate in the glove box. A separate bulk-LFP precursor solution was also poured into a quartz boat and dried for the material analysis. Then, the substrate and the bulk-LFP were placed into a tube furnace filled with a gas mixture of $Ar:H_2$ = %90:%10 to prevent the formation of $Fe^{3+}$ impurities, and the samples were heat-treated at 500 $^{o}$C (heating rate was 1$^{o}$C/min) for 5 h. Figure 7.1 shows the preparation steps of the in situ synthesized LFP on vertically aligned

MACNTs on an Al substrate. The active area on the cathode and the net LFP cathode material mass were 2.54 $cm^2$ and ~0.57 mg, respectively. The mass ratio of the CNTs and the LFP material, $M_{LFP/CNT}$ is ~1.69.

### 7.1.2. Material Characterization

A Hitachi S-4200 scanning electron microscope (SEM) and a Thermo Scientific DXR Raman system, which was equipped with a 532 nm green laser, were used for the structural analysis of the CNTs. The crystal structure of the LFP was investigated by X-ray diffraction (XRD) analysis which was carried out on a Rigaku Powder X-ray Diffractometer with a Cu K-$\alpha$ radiation ($\lambda$ = 1.54059) in the $2\Theta$ range of $10^o$ to $70^o$.

An SEM picture of the MA-CNTs grown by HFCVD is shown in Figure 7.2. The height and the footprint of the MA-CNTs are 25 μm and ~8 x 8 $cm^2$, respectively. In this structure, the open space between the CNTs is beneficial to facilitate the electrolyte diffusion into the CNT forest. In Figure 7.3(a), the SEM

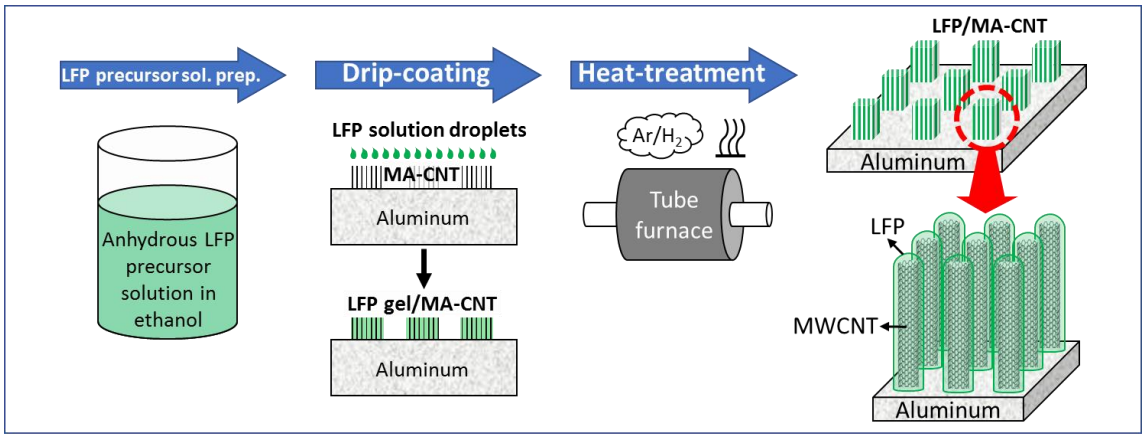


Figure 7.1 Fabrication stages of LFP/MA-CNT/Al Li-ion battery cathode.

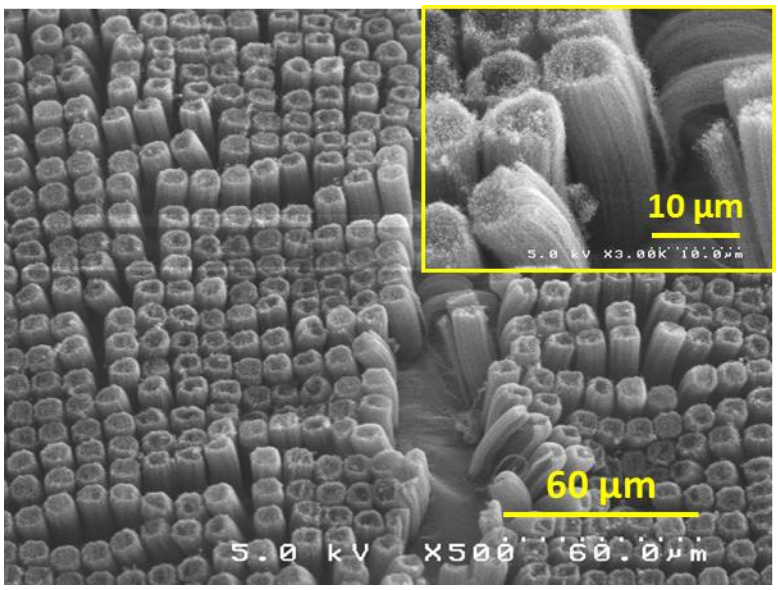


Figure 7.2 Top view SEM micrograph of the vertically aligned, micro-array patterned CNTs on Al substrate. Inlet – high magnification view of the CNT array.

image of the LFP-deposited MA-CNT shows that the CNTs collapsed during the drip-coating process of the LFP precursor solution. However, a thin and uniform LFP coating on the CNTs, which is critical for the high-power capability of the cathode was observed, as shown in Figure 7.3(b). The diameter of the LFP particles coated on the CNTs is ~10 nm, implying a very short Li-diffusion pathway. With this technique, any extra efforts to reduce the size of the cathode particles, like through conventional ball-milling, which may frequently be a many-hours long operation, were no longer required.

In regard to the structural characterization of the synthesized LFP material, its XRD spectrum is shown in Figure 7.4. It is clear that our $LiFePO_4$ is greatly crystalline with an orthorhombic structure; the highest peaks are in excellent agreement with the ones from the reference $LiFePO_4$ peaks of the Inorganic Crystal Structure Database (ICSD, No. 290335). The calculated lattice

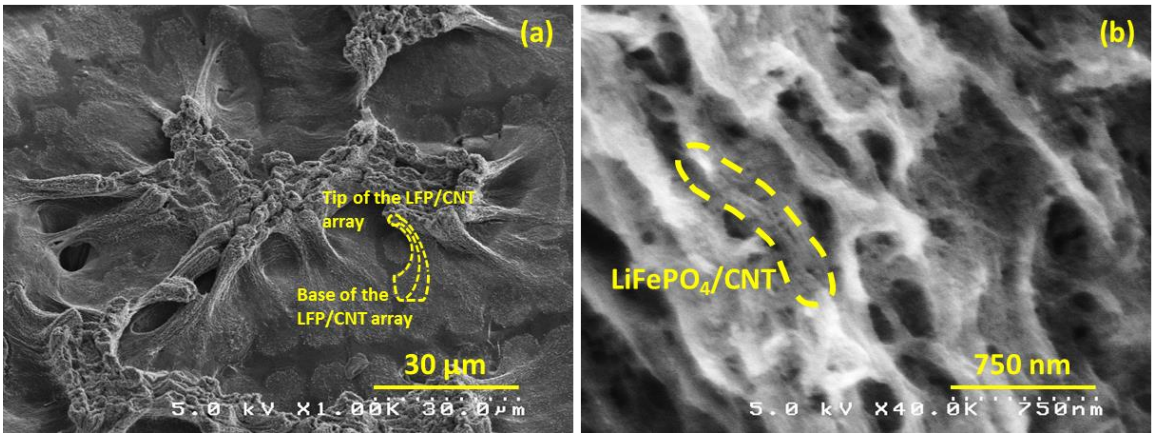


Figure 7.3 SEM micrographs of the LFP coated MA-CNT on Al after heat-treatment: (a) taken from the top view at low magnification and (b) taken at a higher magnification.

parameters (a = 10.338 Å, b = 6.013 Å, c = 4.696 Å) are matching with the ones from the works of other authors [168,171]. At *2Θ* values of 40.26 º, 44.18º, and 47.24º, we observed an iron phosphide ($Fe_2P$) formation. During the bulk-LFP synthesis, slow evaporation of the LFP precursor solution might've caused

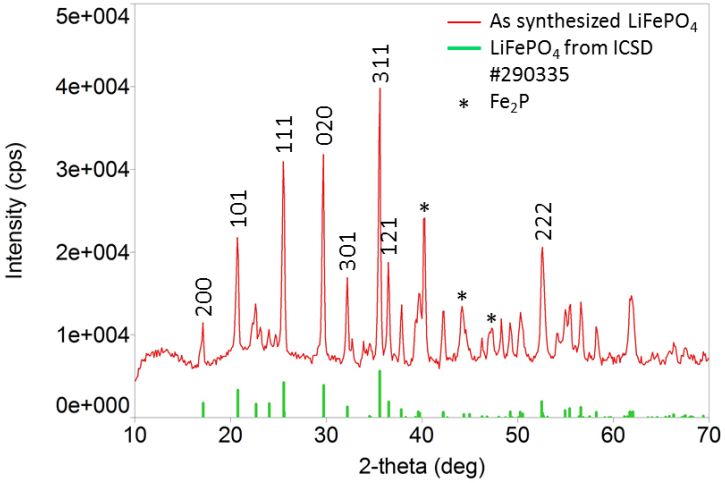


Figure 7.4 X-ray diffraction pattern of the anhydrous sol-gel synthesized $LiFePO_4$ material.

precipitation, especially of the hardly dissolved lithium acetate. This precipitation could've led to lithium deficiency and the appearance of $Fe^{2+}/Fe^{3+}$ redox couple, which catalyzes the formation of $Fe_2P$, however, we're not expecting this way of $Fe_2P$ formation on LFP/MA-CNTs/Al since the LFP precursor solution droplets were dried rapidly on the CNTs [172].

## 7.2. Electrochemical Characterization

For the electrochemical performance tests, the same Li-ion half-cell battery configuration described in Chapter 6 was employed. As the Li-ion battery electrolyte, 1 M $LiPF_6$ was dissolved in DMC and EC (DMC:EC = 1:1 v/v). Galvanostatic charge-discharge and AC impedance tests were performed in a CH Instruments Texas CHI 660C potentiostat, which is accompanied with a data acquisition software.

After assembling the cell, initially, the Nyquist plots of the AC impedance spectrum of the battery cell were obtained in the frequency range of 0.2 Hz – 100 kHz with an AC amplitude of 5 mV and at different stages of the cycling, as shown in Figure 7.5. According to these results, the polarization resistance ($R_p$) increases from 117 Ω before the charge-discharge tests to 674 Ω at cycle-37. This increase is because of the formation of a solid electrolyte interface (SEI) layer on the highly porous LFP/MA-CNT/Al cathode during the charge-discharge tests. After many cycles, such as after the $50^{th}$ cycle, the polarization resistance increases to 935 Ω, which is very large and can be attributed to the electrolyte decomposition, thus further SEI layer formation.

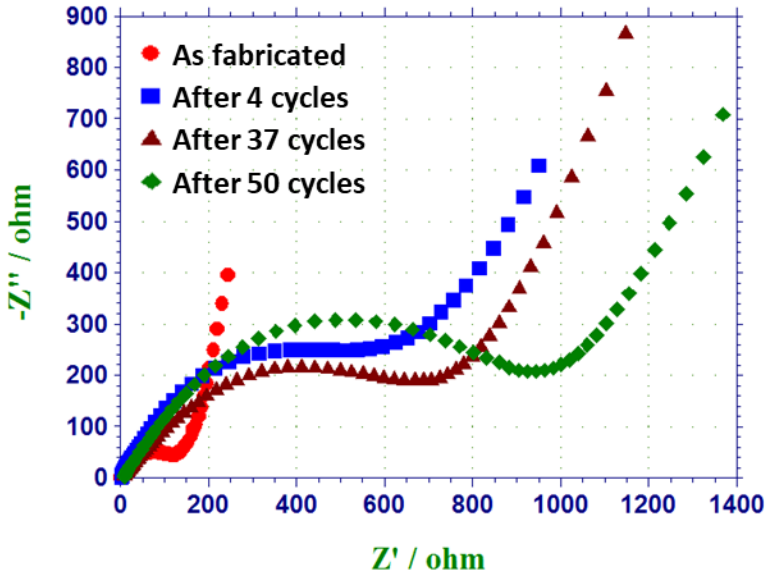


Figure 7.5 Nyquist plots of the AC impedance spectrum of the Li-ion battery cell with LFP/MA-CNT/Al cathode before cycling and after different charge-discharge cycles.

Galvanostatic charge-discharge tests of the Li-ion battery cell with the novel LFP/MA-CNT/Al cathode were performed initially in the voltage window of 2 V to 4.2 V at different C-rates (0.05, 0.1, 0.2, 0.5, 1, 2, 5, 10, 20, and 30 C). Figure 7.6(a) shows the constant-current charge-discharge curves at 0.1 C, and the gravimetric specific discharge capacity of the cell was 173.5 mAh/g, which is more than the theoretical capacity (170 mAh/g) of the LFP material. This slight excess in the capacity of the cathode might be related to the double-layer capacitance contribution from the CNTs. During charging, starting at 4 V, the voltage slope also decreases, which might be due to electrolyte decomposition, although the voltage window of 2 – 4.2 V is widely used for our electrolyte. The discharge curves of the battery cell obtained after charging at different C-rates are overlaid in Figure 7.6(b). At 0.05 C, the gravimetric specific discharge

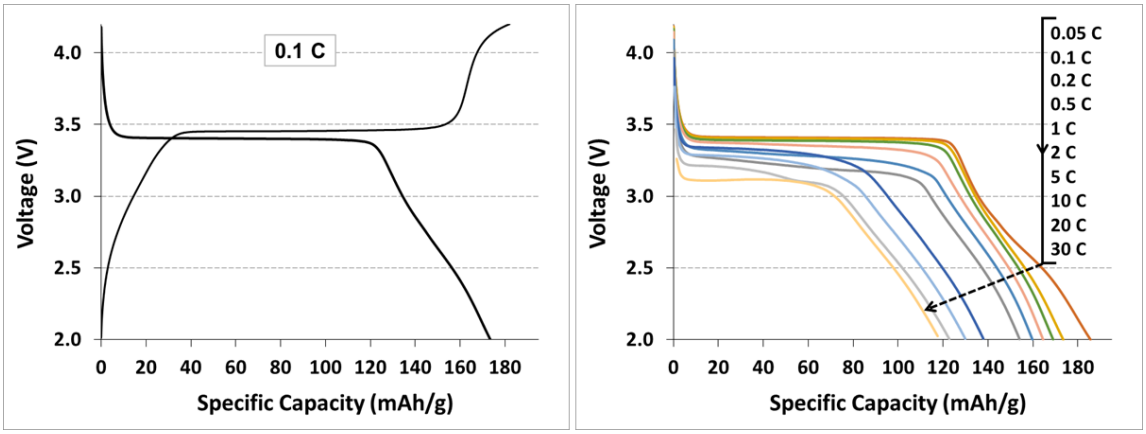


Figure 7.6 (a) Constant current charge-discharge curves of the Li-ion battery cell with an LFP/MA-CNT/Al cathode at a current rate of 0.1 C in the voltage window of 2 - 4.2 V. (b) Discharge curves at varying C-rates (0.05, 0.1, 0.2, 0.5, 1, 2, 5, 10, 20, and 30 C).

capacity of the cathode material was recorded as 185.5 mAh/g. It is one of the highest discharge capacities obtained for $LiFePO_4$ so far. At the higher discharge rates, our cathode maintained most of its capacity. For example, at 30 C, the discharge capacity of the LFP material was 117.6 mAh/g, which is 69 % of the theoretical capacity. In Figure 7.7, specific discharge capacity variation of the LFP material, after being cycled at different C-rates, can be seen. The high-power capability of our cathode is due to the strong bonding between each nanotube and the thin and uniform LFP coating surrounding the tube, which was obtained after the in-situ heat treatment of the anhydrous LFP precursor solution gel incorporated onto MA-CNTs on Al. Cycling performance of the cathode was also evaluated after charging and discharging the battery cell in the voltage window of 2 – 4 V to save electrolyte from degradation, for 61 consecutive cycles, starting at cycle-57, as illustrated in Figure 7.8. The gravimetric specific capacity of the cathode material was initially 159 mAh/g, and it increased up to

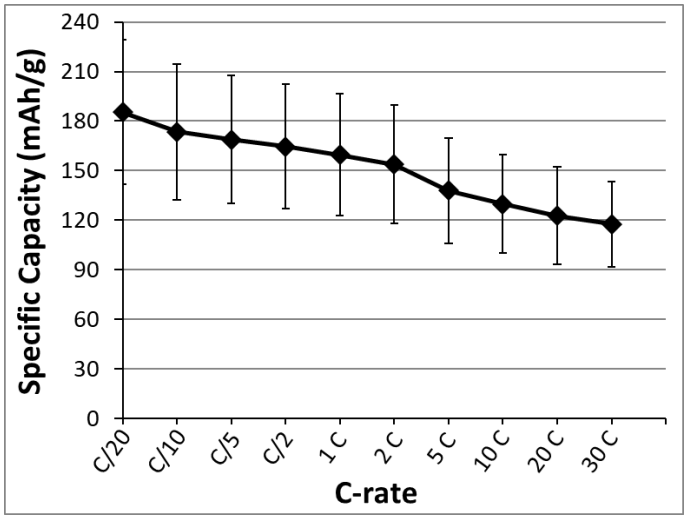


Figure 7.7 Gravimetric specific discharge capacity recordings of the Li-ion battery cell with LFP/MA-CNT/Al cathode at different current rates (0.05C to 30 C) after being cycled between 2 and 4 V. Error bars are added to every data point.

167.2 mAh/g at cycle-66, possibly due to the structural modifications such as on-site crack formations occurring on the cathode material after cycling at very high C-rates in the previous cycles, which allow a higher surface area of the LFP material, thus more Li-diffusion pathways. In the following cycles, we observed a

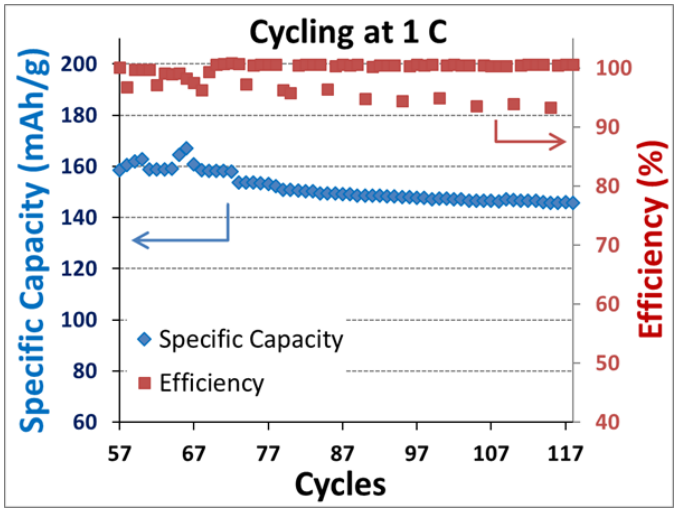


Figure 7.8 Specific capacity and efficiency recordings of the Li-ion battery cell with LFP/MA-CNT/Al cathode during cycling at 1 C current rate.

continuous drop in the capacity (145.8 mAh/g) up to at the 117$^{th}$ cycle. This drop might be related to the imperfect nature of the electrolyte after cycling, therefore limiting the Li-ion transport to the cathode, which can be confirmed by the increasing trend of the impedance after cycling (Figure 7.5). During the cycling tests, coulombic efficiency of the battery cell stayed mostly at ~100%, as shown in Figure 7.8. However, the cycling routine, thus, the rest times between the cycles were not fixed. For example, after cycle-68, we tried to run five consecutive charge-discharge cycles with zero rest time in between them; only at the 1$^{st}$ one of the consecutive cycles, the efficiency was less than %100. The reduced efficiency might be due to the migration of the decomposed electrolyte species away from the porous cathode. In Table 7.1, the electrochemical characterization results, such as the gravimetric specific capacity, the specific

Table 7.1 Summary of the electrochemical characterization results of the Li-ion battery cell after charging and discharging at varying C-rates.

| C rate | Specific Capacity (mAh/g) | Average Potential (V) | Specific Energy (Wh/kg) | Specific Power (W/kg) |
|---|---|---|---|---|
| 0.05 | 185.5 | 3.4 | 631 | 29 |
| 0.1 | 173.5 | 3.4 | 590 | 58 |
| 0.2 | 168.9 | 3.4 | 571 | 115 |
| 0.5 | 164.5 | 3.3 | 550 | 284 |
| 1 | 159.7 | 3.3 | 521 | 554 |
| 2 | 153.9 | 3.2 | 490 | 1081 |
| 5 | 137.9 | 3.3 | 451 | 2779 |
| 10 | 129.9 | 3.2 | 416 | 5439 |
| 20 | 122.8 | 3.1 | 380 | 10521 |
| 30 | 116.3 | 3.1 | 360 | 15766 |

energy, the specific power, and the average potential are listed. The highest values of the specific energy and the specific power of the cell were 631 Wh/kg at 0.05 C and ~15.8 kW/kg at 30 C, respectively.

## 7.3. Summary

- A novel binder-free Li-ion battery cathode, $LiFePO_4$ synthesized on micro-array patterned vertically aligned CNTs on Al-foil was successfully fabricated.
- We obtained a very high gravimetric specific capacity, 185.5 mAh/g at 0.05 C, although a small portion of it might be coming from the double layer capacity of the highly porous CNTs.
- Even though we did not use any binder or any conductive additive, the binding between the LFP cathode material and the CNT is very strong, as confirmed by the charge-discharge tests at high C-rates (129.9 mAh/g discharge capacity at 10 C).

- Another contribution to the high-power performance is coming from the thin and uniform coating of the LFP material on the CNTs, which allows short Li-diffusion pathways and good electrical contact.
- In this work, the net cathode fabrication time is nearly same as the total LFP material synthesis time, since the MA-CNT/Al synthesis takes less time and can be made simultaneously; therefore, this novel cathode

fabrication technique takes at least 30% less time than the slurry technique.

- The high CNT to LFP mass ratio can be reduced with further optimization of the cathode, e.g., sequential deposition of the LFP material onto the CNTs.
- The areal mass loading of the active material in our cathode structure can also be increased by growing taller CNTs and utilizing them as the current collectors for a higher mass of the LFP material.

# CHAPTER VIII

# CONCLUSIONS AND RECOMMENDATIONS FOR FUTURE WORK

## 8.1. Conclusions

### 8.1.1. CNT-based DSSC Cathodes

Vertically aligned CNTs in planar and microarray-patterned configurations were successfully synthesized on Si substrates in an HFCVD system making our cathode for the DSSCs without the need for any binder/additives. The CNT height was nearly 45 μm and the MA-CNTs had a footprint of ~7.5 x 7.5 $\mu m^2$. A cathode control sample, Pt/Si, was also fabricated. We were also able to produce a standardized photoanode, $TiO_2$ spin-coated onto FTO/glass and sensitized with N-719 dye for our DSSCs.

After the I-V measurements under solar illumination, higher $J_{SC}$, $V_{OC}$, and $\eta$ for the P-CNTs, and higher $J_{SC}$ and $V_{OC}$ for the MA-CNTs were observed than those of the Pt-cathode, indicating a better electrocatalytic activity for the vertically aligned CNTs. Our P-CNTs also achieved a $J_{SC}$ of 26.3 mAh/g, which is the highest $J_{SC}$ obtained from a CNT-based DSSC cathode so far to the best of our knowledge. We demonstrated that vertically aligned CNTs have good electrocatalytic performance, which makes them a preferred alternative to the expensive and corrosive conventional Pt-cathode.

### 8.1.2. $MnO_2$/MA-CNT-based Cathodes for Photocapacitors

Microarray patterned CNTs on Si substrates and dye/$TiO_2$/FTO/glass photoanodes were prepared in the same way described in Chapter 3. With the CV technique, different amount of $MnO_2$ was coated onto the MA-CNTs, making the cathodes of the photocapacitors. An MA-CNT/Si substrate was used as the control sample. An electrolyte consisting of 1M TEABF4 in acetonitrile was used for the electrochemical reactions. Unlike many photocapacitors fabricated with a three-electrode, two-electrolyte setup, our devices employ a much simpler configuration: two electrodes (a photoanode and a capacitive cathode) sandwiching a single electrolyte without a separator.

The patterned CNTs are proven to be suitable for acting as a host for the pseudocapacitive $MnO_2$ particles. Our photocapacitor was able to reach a charging voltage of 0.955 V, which is higher than those of many other devices fabricated by the researchers. With a capacitance of 13.1 $mF/cm^2$ and being made of low-cost, our compact photocapacitor can be a good candidate for the portable and household energy harvesting/storage devices.

### 8.1.3. Novel LIB Cathode Material: $Li_2Fe_xMn_yCo_zSiO_4$

A new cathode material with more than one Li atom in the unit structure, $Li_2Fe_xMn_yCo_zSiO_4$ (DTS, x + y + z = 1) was synthesized. Four different DTS materials' synthesis was devised via a sol-gel method: $Li_2Fe_{0.5}Mn_{0.25}Co_{0.25}SiO_4$, $Li_2Fe_{0.6}Mn_{0.2}Co_{0.2}SiO_4$, $Li_2Fe_{0.7}Mn_{0.15}Co_{0.15}SiO_4$, and $Li_2Fe_{0.8}Mn_{0.1}Co_{0.1}SiO_4$, which were used as the cathode materials in the LIB cells DTS#1, DTS#3,

DTS#4, and DTS#2, respectively. Structural characterization achieved through XRD presented a big amount of metallic Fe impurity, and the baseline peaks at different 2Θ values did not match with the other simpler dilithium metal silicate compounds (i.e., $Li_2FeSiO_4$ and $LiFe_xMn_{1-x}SiO_4$) scientists have synthesized. The fabricated LIB cathodes consisted of the DTS materials deposited onto VACNT/graphite substrates.

Electrochemical charge-discharge tests of the LIB cells showed a hybrid performance characterized by intercalation/deintercalation of the two-lithium ions ($Li^+$) and $PF_6^-$ anions, making it difficult to calculate the gravimetric capacity of the DTS material. For the cell DTS#3, however, the sharp decline in the voltage slope starting at 2.4 V and continuing down to 1.8 V made this calculation possible, and the specific capacity of the DTS material was calculated to be ~361 mAh/g, which is very close to its theoretical capacity. Hence, demonstrating extremely high capacity is achievable by using this novel dilithium ternary orthosilicate material compared to many other cathode materials.

### 8.1.4. MA-CNTs/Al as the LIB Cathode Host

Vertically aligned CNTs were grown on Al substrates in the microarray configuration in HFCVD using $CH_4$ for the first time as the carbon source. Unlike the conventional LIB battery cathodes, MA-CNT/Al was used as the host of the LFP cathode material, which eliminated to use any binder. The LFP material was deposited onto the host structure with two different methods: vibration-assisted drip coating and electrophoretic deposition. The electrophoretic deposition of the

LFP material onto MA-CNT/Al also made the cathode fabrication more facile than the slurry technique.

The equivalent circuit of the LIB cell was successfully modeled, and its simulated AC impedance spectroscopy response perfectly matched with the fabricated LIB cell's response. After the charge-discharge tests at varying C-rates, the LIB cell with the electrophoretically deposited LFP on MA-CNT/Al as the cathode maintained most of its capacity at low C-rates, proving the novel cathode host as a good candidate for the binder-free LIB cathodes at low-power applications.

### 8.1.5. Novel LIB Cathode Fabrication Technique: In-situ Synthesis of $LiFePO_4$ on MA-CNT/Al

A binder and additive-free LIB cathode fabrication technique, in-situ synthesis of the LFP material on MA-CNT/Al was devised and electrochemically tested. An anhydrous LFP precursor solution was deposited onto the MA-CNT/Al substrate, which was then calcinated at 500$^{o}$C, resulting in a thin and uniform LFP coating on the CNTs. The net fabrication time of this cathode was at least 30 % faster than the slurry technique.

With in-situ synthesized LFP on MA-CNT/Al cathode, we were able to obtain a very high specific discharge capacity (185.5 mAh/g), which is one of the highest discharge capacities obtained for the LFP material so far and a high-power performance during the charge-discharge tests. This cathode fabrication

technique can be considered very practical and efficient for the next-generation LIB cathodes.

## 8.2. Recommended Future Work

In order to improve the performance of the DSSCs, cathodes made of CNTs with different heights might be fabricated. Optimum $\eta$ and $J_{SC}$ can be found by evaluating the electrocatalytic performance of these CNTs. In addition, electrolytes with various redox couples (for example, $Co^{(II/III)}$ or $Cu^{(I/II)}$) should also be studied to enhance $\eta$, $J_{SC}$, and *FF* of the DSSCs.

The low $J_{SC}$, $\eta$, and *FF* of the photocapacitors can also be improved through examination of different electrolytes having redox couples with suitable redox energy levels for the regeneration of the dye molecules as well as providing electrons for the reduction of the $MnO_2$ particles. Both the DSSC and the photocapacitor performances can be made more stable for the long operation time through sealing them as the other scientists have done [70,71,134], which will eliminate the evaporation of the electrolyte solvent and the resultant change in the diffusion kinetics of the electrolyte.

The synthesis method of the DTS material must be refined since its XRD spectrum deviates from the similar dilithium metal silicates. The possible reason might be the inadequate amount of catalysts for the chemical reactions to be complete. As Yan's group showed, hydroxide ions ($OH^-$), which were derived from acetic acid, catalyze the formation reactions of dilithium metal silicate materials [151]. In our synthesis routine, however, there is not a catalyst and the

citric acid dissolved in water is not likely to release $OH^-$ ions when dissolved in water because of the strong covalent bonds between them and the carbon atoms. As a result, the synthesized material might be deviating from the desired DTS material, based on the XRD spectrum analysis; therefore, modifying the synthesis into a catalyst-assisted one would be beneficial for the DTS formation reactions.

The low power performance of the MA-CNT/Al cathode host can be improved with the addition of trace amount of binder to the final LFP/MA-CNT cathode. The binder can be prepared as a solution (for example, PVDF in NMP) and drip coated onto identical cathodes in different amounts; thus, we can determine the minimum amount of binder required for an improved power capability of the LIB cathode.

The decent areal mass loading of the cathode material in the in-situ synthesized LFP/MA-CNT/Al might be improved with consecutive deposition of the LFP material onto the CNTs such that the LFP precursor solution will be drip coated again to fill the gaps in the nanostructure of the LFP/MA-CNT and calcinated again. This process might be done repeatedly until the desired mass of LFP material is obtained in the cathode. With the help of this technique and growing taller VACNTs, very high areal cathode material mass loadings, which are greater than that of the conventional slurry technique (~2 mg/cm$^2$) [106,110] can be achieved. Scientists have shown the effect of water, keeping the catalyst particles clean for a longer duration, which is vital for the taller CNT growth, therefore recommended for the future attempts to grow very tall CNTs [174-176]. Since we have only tried one calcination temperature, 500$^o$C in the synthesis of

LFP/MA-CNT, higher calcination temperatures must also be studied, which might provide stronger bonding between the LFP particle and the CNTs. However, Al's melting point (660 $^{o}$C) might be limiting in the high-temperature heat treatment, considering the exothermic chemical processes might also cause extra heat to build upon the substrate.

Nickel, which has a high melting point (1455 $^{o}$C) can be used for the calcination process, but its high standard oxidation potential (0.25 V vs. standard hydrogen electrode (SHE)) compared to the standard oxidation potential of Li-metal (3.04 V vs. SHE) makes it unsuitable for a Li-metal anode. For this reason, graphite anode might be used for the Ni cathode substrate in the proposed LIB cell. Another advantage of the high-temperature durable Ni can be that we can grow a few layers thick graphene on it. Graphene, being the base layer for the VACNTs would be chemically resistant, protecting the Ni-substrate against the vigorous chemical reactions occurring at high-temperature calcination of the cathode material precursor solution.

The unstable behavior of the electrolyte in the LIBs might be improved by using some of the recently developed stable electrolytes. Wang's group's 1 M lithium bis(fluorosulfonyl)amide (LiFSA) salt dissolved in DMC and Drozhzhin's group's $LiBF_4$ dissolved in propylene carbonate (PC) in the molar ratio of 1:4, respectively might be good alternative electrolytes [177,178].

# PUBLICATIONS

## Conference Presentations

1. Joyce B. Kang, Supil Raina, Shao-Hua Hsu, Serkan Akbulut and Mesut Yilmaz "Advanced, flexible ultracapacitor electrodes on carbon fiber cloth using nano-architectured $MnO_2$/CNT", *ECS 225th Meeting*, May 11- 16, 2014, Orlando, FL.
2. Supil Raina, Shao-Hua Hsu, Serkan Akbulut, Mesut Yilmaz, Weng P. Kang, Mick Howell, Jin-Hua Huang "Design and Development of 3D Nanostructured $MnO_2$/CNT Electrodes for Supercapacitor Applications", *ECS 225th Meeting*, May 11- 16, 2014, Orlando, FL.
3. Supil Raina, Shao-Hua Hsu, Mesut Yilmaz, Serkan Akbulut, Weng P. Kang, Jin-Hua Huang "$Li_2Fe_xMn_yCo_zSiO_4$ Nanoparticles Incorporated CNTs As a Novel High Capacity Cathode for Lithium Ion Batteries", *ECS 224th Meeting*, October 27- November 1, 2013, San Francisco, CA.
4. Supil Raina, Shao-Hua Hsu, Serkan Akbulut, Mesut Yilmaz, Weng P. Kang, Jin-Hua Huang "Advanced $MnO_2$/CNT Ultracapacitors- Transition From Planar to Micropatterned Array Electrodes", *ECS 224th Meeting*, October 27- November 1, 2013, San Francisco, CA.
5. W. P. Kang, Supil Raina, S. H. Hsu, M. Yilmaz, Jin-Hua Huang, A. Serkan, "A Novel Nano-Structured Ternary Orthosilicate on Carbon Nanotube as Lithium-Ion Battery Cathode", *ECS 223rd meeting*, 2013, Toronto, Canada.

6. W. P. Kang, S. H. Hsu, S. Raina, S. Akbulut, M. Yilmaz, J. H. Huang, “Micropatterned MnO2/CNT Ultracapacitor Array with High Volumetric Capacitance”, *IEEE Nanotechnology Materials and Devices Conference*, 2013, Tainan, Taiwan.
7. Supil Raina, S. H. Hsu, W. P. Kang, J. H. Huang and M. Yilmaz, “In Situ Electrochemical Deposition of MnO2 on CNTs for Ultracapacitor Applications”, *ECS 222nd meeting*, 2012, Honolulu, HI.

## Journal Publications

1. Mesut Yilmaz, Supil Raina, Shao-Hua Hsu, Weng P. Kang, “Micropatterned Arrays of Vertically-Aligned CNTs Grown on Aluminum as a New Cathode Platform for $LiFePO_4$ Integration in Lithium Ion Batteries”, *Ionics*, (2018).
2. Mesut Yilmaz, Shao-Hua Hsu, Supil Raina, Mick Howell, Weng Poo Kang, and Jin-Hua Huang, “Dye-sensitized solar cells using carbon nanotube-based counter electrodes in planar and micro-array patterned configurations”, *Journal of Renewable and Sustainable Energy,* 10, (2018) 063501.
3. Mesut Yilmaz, Shao-Hua Hsu, Supil Raina, Mick Howell, Weng P. Kang, “Integrated Photocapacitors based on Dye-Sensitized $TiO_2$/FTO as Photoanode and $MnO_2$ Coated Micro-Array CNTs as Supercapacitor Counter Electrode with TEABF4 Electrolyte”, *Journal of Renewable and Sustainable Energy,* 10, (2018) 063503.
4. Halina Krzyżanowska, William F. Paxton, Mesut Yilmaz, Anthony Mayo, John Kozub, Mick Howell, Justin Gregory, James E. Butler, Weng Poo Kang,

Richard Mu, Jimmy L. Davidson, and Norman H. Tolk, “Low Temperature Diamond Growth Arising from Ultrafast Pulsed-Laser Pretreatment”, Carbon 131, (2018) 120-126.

5. Mesut Yilmaz, Supil Raina, Shao-Hua Hsu, Weng Poo Kang, “Growing micropatterned CNT arrays on aluminum substrates using hot-filament CVD process”, *Materials Letters*, 209, (2017) 376-378.
6. Serkan Akbulut, Mesut Yilmaz, Supil Raina, Shao-Hua Hsu and Weng Poo Kang, “Advanced supercapacitor prototype using nanostructured double-sided $MnO_2$/CNT electrodes on flexible graphite foil”, *Journal of Applied Electrochemistry*, 47(9), (2017) 1035-1044.
7. Serkan Akbulut, Mesut Yilmaz, Supil Raina, Shao-Hua Hsu and Weng Poo Kang, “Solid-state supercapacitor cell based on 3D nanostructured $MnO_2$/CNT microelectrode array on graphite and $H_3PO_4$/PVA electrolyte”, *Diamond and Related Materials* 74, (2017) 222-228.

# APPENDIX A

# UNCERTAINTY ANALYSIS OF THE MEASUREMENTS

Uncertainty analysis was conducted separately for each fabricated device. For the calculations including only a single variable with a known uncertainty, the upper-lower bound method was used. If we try to calculate the value of function $f(x)$ of variable $x$, which has uncertainty $u_x$, we find maximum ($f_{max}$) and minimum ($f_{min}$) values of $f$ and then use these values to calculate the uncertainty ($u_f$) and the average value ($f_{avg}$) of $f$:

$$f_{avg} = \frac{f_{min}+f_{max}}{2} \quad \text{(A.1)},$$

$$u_f = \frac{f_{max}-f_{min}}{2} \quad \text{(A.2)},$$

and

$$f_{calc} = f_{avg} \mp u_f \quad \text{(A.3)},$$

where $f_{calc}$ is the calculated $f$ with uncertainty values.

In our experiments, some uncertainties were high because we fabricated cells in small scale and optimizations such as high material mass-loading, high active area, were not made for our cells since some of our work is preliminary of the future work. During our measurements, the best available tools were utilized in our facilities, such as CH Instruments' CHI660C model electrochemical workstation for the current and potential measurements with $\ll$ 1 nA and $\ll$ 1 mV uncertainties. However, for some measurements, such as the material mass, the highest precision weighing scale we could utilize had an uncertainty of 0.1 mg;

when multiple weight measurements regarding an electrode fabrication were made, it increased the uncertainties in material mass calculations.

For the uncertainty analysis of variables, which are the function of multiple parameters with known uncertainties, Moffat's uncertainty analysis was used [179]. During the performance characterization of each device, when *N* number of measurements were made for a sample parameter (e.g., the gravimetric specific discharge capacity of a LIB cell), if our measurements for a variable $f$ are $x_1, x_2, \dots, x_N$, a single measurement can be represented as $x_i \mp u_{x_i}$, where $u_{x_i}$ is the uncertainty associated with the parameter $x_i$.

Based on the method described by Moffat [179], the uncertainty of $f(x_1, x_2, \dots, x_N)$ will be

$$u_f = \sqrt{\left(\frac{\partial f}{\partial x_1}\right)^2 {u_{x_1}}^2 + \left(\frac{\partial f}{\partial x_2}\right)^2 {u_{x_2}}^2 + \cdots + \left(\frac{\partial f}{\partial x_N}\right)^2 {u_{x_N}}^2} \qquad \text{(A.4)}.$$

## A.1.Uncertainty Analysis in Photovoltaic Performance of the DSSCs

For the uncertainty analysis of the DSSCs' photovoltaic performance, upper-lower bound method was used. In our devices, the circular active area (A) is calculated as

$$A = \pi \left(\frac{R}{2}\right)^2 \qquad \text{(A.5)}.$$

Accordingly, $J_{SC}$ and η are

$$J_{SC} = \frac{I \times 4}{\pi \times R^2} \qquad \text{(A.6)}$$

and

$$\eta = \frac{P_{max}}{P_{in}} = \frac{I_m \times V_m \times 4}{100\ mW/cm^2 \times \pi \times R^2}\ , \quad \text{(A.7)},$$

where $I_m$ and $V_m$ are current and potential readings from the I-V test, constituting the maximum power ($P_{max}$). In our experiments, we also used a meter stick with 0.1 cm division and considering that we employed interpolation fraction of ½,

$$meter\ stick\ uncertainty = smallest\ division \times interpolation\ fraction$$

$$= 0.05\ cm \quad \text{(A.8)}$$

Using the meter stick uncertainty ($u_m$), we first calculated minimum ($J_{SC\_min}$ and $\eta_{min}$), maximum ($J_{SC\_max}$ and $\eta_{max}$) of $J_{SC}$ and $\eta$. The average ($J_{SC\_avg}$ and $\eta_{avg}$) of $J_{SC}$ and η are:

$$J_{SC\_avg} = \frac{J_{SC\_min} + J_{SC\_max}}{2} \quad \text{(A.9)}$$

and

$$\eta_{avg} = \frac{\eta_{min} + \eta_{max}}{2} \quad \text{(A.10)}.$$

Uncertainties of $J_{SC}$ and η are

$$u_{JSC} = \frac{J_{SC\_max} - J_{SC\_min}}{2} \quad \text{(A.11)}$$

and

$$u_\eta = \frac{\eta_{max} - \eta_{min}}{2} \quad \text{(A.12)},$$

respectively. In Table A.1, we calculated the uncertainties of $J_{SC}$ and $\eta$ of our DSSCs.

Table A.1 Photovoltaic performance measurements with uncertainties in our DSSCs with different counter electrodes.

| DSSC Counter Electrode | Diameter (R) of active opening (cm) | $J_{SC}$ (mA/cm$^2$) | $\eta$ (%) |
|---|---|---|---|
| Platinum (Control sample) | 1.0 ± 0.05 | 20.8 ± 2.1 | 6.34 ± 0.63 |
| P-CNT (Planar CNTs) | 0.7 ± 0.05 | 26.7 ± 3.8 | 7.24 ± 1.03 |
| MA-CNT (Micro-array patterned CNTs) | 0.7 ± 0.05 | 22.5 ± 3.2 | 5.82 ± 1.63 |

## A.2.Uncertainty in the Performance Calculations of the Photocapacitors

Similar to the uncertainty analysis in Appendix A.2, we calculated uncertainties of $J_{SC,}$ $\eta$, and specific discharge capacitance of our photocapacitors and listed them in Table A.2. For the photocapacitor PC-2 with 4-cycle MnO2-coated cathode, specific discharge capacitance calculations with uncertainty, which were obtained after solar charging for varying times followed by a constant current discharge, were also listed in Table A.3.

Table A.2 Photovoltaic ($J_{SC}$ and $\eta$) and capacitive (specific discharge capacitance) performance of photocapacitors with different $MnO_2$-coated counter electrodes calculated with uncertainties.

| # of cycles for $MnO_2$ coating (Sample) | Diameter, $R$ (cm) | $J_{SC}$ (mA/cm$^2$) | $\eta$ (%) | Specific Discharge Capacitance with Uncertainty (mF/cm$^2$) |
|---|---|---|---|---|
| 0 (PC-0) | 0.7 ± 0.05 | 0.238 ± 0.034 | 0.004 ± 0.001 | N/A |
| 2 (PC-1) | 0.7 ± 0.05 | 0.761 ± 0.108 | 0.037 ± 0.005 | 8.94 ± 1.27 |
| 4 (PC-2) | 0.7 ± 0.05 | 0.620 ± 0.088 | 0.049 ± 0.007 | 13.30 ± 1.89 |

Table A.3 Uncertainties of specific discharge capacitance in our photocapacitor PC-2 (with 4-cycle $MnO_2$ coated cathode) obtained after 1-sun solar charging for varying times, followed by 10 μA constant-current discharge.

| Cycle # | 1-Sun Charge Time (min.) | Diameter, *R* (cm) | Specific Discharge Capacitance Calculation with Uncertainty ($mF/cm^2$) |
|---|---|---|---|
| 1 | 3 | 0.7 ± 0.05 | 4.5 ± 0.6 |
| 2 | 6 | 0.7 ± 0.05 | 7.6 ± 1.1 |
| 3 | 12 | 0.7 ± 0.05 | 8.4 ± 1.2 |
| 4 | 20 | 0.7 ± 0.05 | 12.2 ± 1.7 |
| 5 | 40 | 0.7 ± 0.05 | 13.3 ± 1.9 |

## A.3.Uncertainty in Electrochemical Performance of the LIB Cells with $Li_2Fe_xMn_yCo_zSiO_4$ Cathode

As we explained in Chapter V, gravimetric specific discharge capacity calculations were not listed for the LIB cells with $Li_2Fe_xMn_yCo_zSiO_4$ cathode material except for the LIB cell DTS#3. If we reevaluate the calculations with uncertainty for this cell with the upper-lower bound method, its active cathode material will have a gravimetric specific discharge capacity of 366.0 ± 33.3 mAh/g.

## A.4.Electrochemical Performance Measurements with Uncertainties for the LIB Cells with Deposited-LFP/MA-CNT/Al Cathode

For the uncertainty analysis of the specific discharge capacity calculations of LIB cells with deposited-LFP/MA-CNT/Al cathode, we used Moffat's

uncertainty analysis[179] since we have multiple variables (with uncertainties from two different measurements) involved in our gravimetric specific discharge capacity uncertainty ($u_{C_s}$) calculations. Gravimetric specific discharge capacity, $C_s$, is calculated as

$$C_s = \frac{C_r}{m_{e2-}m_{e1}} \quad \text{(A.13)},$$

where $C_r$, $m_{e1}$, and $m_{e2}$ are raw discharge capacity and the mass of the electrode before and after LFP material deposition, respectively. Our CHI660C electrochemical workstation measures $C_r$ with negligible uncertainty, therefore we consider it precise in each measurement. Using the equation (A.4),

$$u_{C_s} = C_r\sqrt{\frac{{u_{m_{e1}}}^2 + {u_{m_{e2}}}^2}{(m_{e2-}m_{e1})^4}} \quad \text{(A.14)},$$

where $u_{m_{e1}} = u_{m_{e2}} = 0.1\,mg$ and are weighing scale uncertainties of the electrode mass measurements before and after LFP deposition, respectively. Accordingly, we calculated the gravimetric specific discharge capacities of the LIB cells with deposited-LFP/MA-CNT/Al cathodes, as shown in Table A.4.

Table A.4 Uncertainty calculations of gravimetric specific discharge capacity measurement at different C-rates for the Li-ion battery cells with deposited-LFP/MA-CNT/Al cathodes.

| Cell | C-rate | Raw Discharge Capacity (uAh) | LFP Mass, m (mg) | Mass Uncertainty, $u_m$ (mg) | Gravimetric Specific Discharge Capacity of LFP with Uncertainty (mAh/g) |
|---|---|---|---|---|---|
| **Cell#1** | 0.05 | 57.1 | 0.6 | 0.1 | 95.2 ± 22.4 |
| | 0.1 | 45.3 | 0.6 | 0.1 | 75.5 ± 17.8 |
| | 0.2 | 39.1 | 0.6 | 0.1 | 65.2 ± 15.4 |
| | 0.5 | 32.3 | 0.6 | 0.1 | 53.8 ± 12.7 |
| **Cell#2** | 0.05 | 57.2 | 0.4 | 0.1 | 143.0 ± 50.6 |
| | 0.1 | 50.3 | 0.4 | 0.1 | 125.8 ± 44.5 |
| | 0.2 | 44.4 | 0.4 | 0.1 | 111.0 ± 39.2 |
| | 0.5 | 39.6 | 0.4 | 0.1 | 99.0 ± 35.0 |

## A.5.Uncertainty in Electrochemical Performance of the LIB Cells with In-situ Synthesized-LFP/MA-CNT/Al Cathode

In our experiments, we used the same meter stick uncertainty as in Appendix A.1, which is 0.05 cm. During the electrode fabrication, we took an aluminum substrate (with a mass $m_{e0}$); synthesized CNT on a circular area on it (yielding an electrode mass of $m_{e1}$ and an active area diameter = $R_1$ = 2.20 cm); deposited the LFP precursor solution onto it, then wiped off both LFP and CNT off a circular ring of LFP/CNT area to get a circular active area with a diameter $R_2$ so that $R_2$ (1.80 cm) ≤ $R_{Li\text{-}foil}$ (1.90 cm), where $R_{Li\text{-}foil}$ is the diameter of the anode, Li-foil. After the calcination of LFP on the electrode, we measured the final electrode mass, $m_{e2}$. Our mass measurements are

$$m_{e0} = bare\ substrate\ mass, \quad \text{(A.15)},$$

$$m_{e1} = m_{CNTR1} + m_{e0} \quad \text{(A.16)},$$

$$m_{e2} = m_{CNTR2} + m_{LFP} \quad \text{(A.17)},$$

$$m_{e2} - m_{e1} = 0.4\ mg, \quad \text{(A.18)},$$

$$m_{e1} - m_{e0} = m_{CNTR1} = 0.5\ mg \quad \text{(A.19)},$$

$$m_{CNTR2} = m_{CNTR1}\left(\frac{R_2}{R_1}\right)^2 \quad \text{(A.20)},$$

where $m_{CNTR1}$, $m_{CNTR2}$, and $m_{LFP}$ are CNT mass on the circular area with a diameter $R_1$, CNT mass on the circular area with a diameter $R_2$, and net LFP material mass on the final electrode, respectively. From the equations (A.15-20),

$$C_s = \frac{C_r}{m_{LFP}} = \frac{C_r}{m_{e2} - m_{e0} - (m_{e1} - m_{e0})\left(\frac{R2}{R1}\right)^2} = \frac{C_r}{k} \quad \text{(A.21)},$$

and from the equation (A.4),

$$u_{C_s} = \sqrt{\begin{array}{c}\left(\frac{\partial C_s}{\partial m_{e0}}\right)^2 {u_{m_{e0}}}^2 + \left(\frac{\partial C_s}{\partial m_{e1}}\right)^2 {u_{m_{e1}}}^2 + \left(\frac{\partial C_s}{\partial m_{e2}}\right)^2 {u_{m_{e2}}}^2 \\ + \left(\frac{\partial C_s}{\partial R_1}\right)^2 {u_{R1}}^2 + \left(\frac{\partial C_s}{\partial R_2}\right)^2 {u_{R2}}^2\end{array}} \quad \text{(A.22)},$$

where $u_{m_{e0}} = u_{m_{e1}} = u_{m_{e2}} = 0.1\ mg$ and are weighing scale uncertainties for the measurements $m_{e0}$, $m_{e1}$, and $m_{e2}$, respectively; $u_{R1} = u_{R2} = 0.05\ cm$ and are meter stick uncertainties associated with the measurements $R_1$ and $R_2$, respectively; $C_s$ is gravimetric specific discharge capacity. If we calculate

$$\frac{\partial C_s}{\partial m_{e0}} = d_1 = \frac{\left[1 - (R_2/R_1)^2\right] C_r}{k^2} \quad \text{(A.23)},$$

$$\frac{\partial C_s}{\partial m_{e1}} = d_2 = \frac{C_r\,(R_2/R_1)^2}{k^2} \quad \text{(A.24)},$$

$$\frac{\partial C_s}{\partial m_{e2}} = d_3 = \frac{-C_r}{k^2} \quad \text{(A.25)},$$

$$\frac{\partial C_s}{\partial R_1} = d_4 = \frac{-2\,C_r\,(m_{e1}-m_{e0}){R_2}^2}{k^2\,{R_1}^3} \quad \text{(A.26)},$$

and

$$\frac{\partial C_s}{\partial R_2} = d_5 = \frac{2\,C_r\,R_2\,(m_{e1}-m_{e0})}{k^2\,{R_1}^2} \quad \text{(A.27)},$$

then

$$u_{C_s} = \sqrt{{d_1}^2\,{u_{m_{e0}}}^2 + {d_2}^2\,{u_{m_{e1}}}^2 + {d_3}^2\,{u_{m_{e2}}}^2 + {d_4}^2\,{u_{R_1}}^2 + {d_5}^2\,{u_{R_2}}^2} \quad \text{(A.28)}.$$

The $u_{C_s}$ formula simply shows us that in our uncertainty calculations for the gravimetric specific discharge capacity, we need to employ every single measurement's uncertainty we have done from the beginning of electrode fabrication. In this case, it will include five measurement uncertainties, three of which are the weighing scale measurement uncertainties (0.1 mg), and the remaining two are meter sick uncertainties (0.05 cm). Using the above equations, we calculated the uncertainties of gravimetric specific discharge capacities obtained at different C-rates for the LIB cell with in-situ synthesized-LFP/MA-CNT/Al cathode, as shown in Table A.5.

Table A.5 Uncertainty calculations of gravimetric specific discharge capacity measurement at different C-rates for the Li-ion battery cell with in-situ synthesized-LFP/MA-CNT/Al cathode.

| C-rate | Raw Charge Capacity (uAh) | Gravimetric Specific Discharge Capacity with Uncertainty (mAh/g) |
|---|---|---|
| 0.05 | 110.4 | 185.5 ± 43.9 |
| 0.1 | 103.0 | 173.5 ± 41.0 |
| 0.2 | 97.5 | 168.9 ± 38.8 |
| 0.5 | 94.6 | 164.5 ± 37.6 |
| 1 | 92.1 | 159.7 ± 36.6 |
| 2 | 89.6 | 153.9 ± 35.6 |
| 5 | 79.8 | 137.9 ± 31.7 |
| 10 | 74.8 | 129.9 ± 29.7 |
| 20 | 73.8 | 122.8 ± 29.4 |
| 30 | 64.9 | 117.6 ± 25.8 |

# REFERENCES


1. M. Inagaki, F. Kang, Chapter 1: Introduction, Materials Science and Engineering of Carbon: Fundamentals (Second Edition), Elsevier, 2014.

2. A. Demming, King of the elements?, Nanotechnology. 21 (2010) 300201. doi:10.1088/0957-4484/21/30/300201.

3. S. Iijima, Helical microtubules of graphitic carbon, Nature. 354 (1991) 56–58. doi:10.1038/354056a0.

4. P.R. Bandaru, Electrical Properties and Applications of Carbon Nanotube Structures, Journal of Nanoscience and Nanotechnology. 7 (2007) 1239–1267. doi:10.1166/jnn.2007.307.

5. C. Cha, S.R. Shin, N. Annabi, M.R. Dokmeci, A. Khademhosseini, Carbon-Based Nanomaterials: Multifunctional Materials for Biomedical Engineering, ACS Nano. 7 (2013) 2891–2897. doi:10.1021/nn401196a.

6. V. Popov, Carbon nanotubes: properties and application, Materials Science and Engineering: R: Reports. 43 (2004) 61–102. doi:10.1016/j.mser.2003.10.001.

7. A. Jorio, G. Dresselhaus, M.S. Dresselhaus, Carbon nanotubes: advanced topics in the synthesis, structure, properties, and applications, Springer, Berlin, 2008.

8. M.F.L.D. Volder, S.H. Tawfick, R.H. Baughman, A.J. Hart, Carbon Nanotubes: Present and Future Commercial Applications, Science. 339 (2013) 535–539. doi:10.1126/science.1222453.

9. S. Kumar, R. Rani, N. Dilbaghi, K. Tankeshwar, K.-H. Kim, Carbon nanotubes: a novel material for multifaceted applications in human healthcare, Chem. Soc. Rev. 46 (2017) 158–196. doi:10.1039/c6cs00517a.

10. C. S. Psomopoulos, Solar Energy: Harvesting the Sun’s Energy for Sustainable Future, Handbook of Sustainable Engineering, J. Kauffman, K. M. Lee (Eds.) 2013, 1065–1107., doi:10.1007/978-1-4020-8939-8_117.

11. J. Su, L. Vayssieres, A Place in the Sun for Artificial Photosynthesis?, ACS Energy Letters. 1 (2016) 121–135. doi:10.1021/acsenergylett.6b00059.

12. A. Lenert, D.M. Bierman, Y. Nam, W.R. Chan, I. Celanović, M. Soljačić, et al., A nanophotonic solar thermophotovoltaic device, Nature Nanotechnology. 9 (2014) 126–130. doi:10.1038/nnano.2013.286.

13. World Energy Resources 2016, 'Used by permission of the World Energy Council. www.worldenergy.org'

14. M.S. Whittingham, History, Evolution, and Future Status of Energy Storage, Proceedings of the IEEE. 100 (2012) 1518–1534. doi:10.1109/jproc.2012.2190170.

15. V. S. Bagotsky, A. M. Skundin, and Y. M. Volfkovich, Part III: Fuel Cells, Electrochemical Power Sources : Batteries, Fuel Cells, and Supercapacitors, Wiley, 2015

16. U. Bossel, Does a Hydrogen Economy Make Sense?, Proceedings of the IEEE. 94 (2006) 1826–1837. doi:10.1109/jproc.2006.883715.

17. M.F. Felgenhauer, M.A. Pellow, S.M. Benson, T. Hamacher, Evaluating co-benefits of battery and fuel cell vehicles in a community in California, Energy. 114 (2016) 360–368. doi:10.1016/j.energy.2016.08.014.

18. W. Zuo, R. Li, C. Zhou, Y. Li, J. Xia, J. Liu, Battery-Supercapacitor Hybrid Devices: Recent Progress and Future Prospects, Advanced Science. 4 (2017) 1600539. doi:10.1002/advs.201600539.

19. L. Dai, D.W. Chang, J.-B. Baek, W. Lu, Carbon Nanomaterials for Advanced Energy Conversion and Storage, Small. 8 (2012) 1130–1166. doi:10.1002/smll.201101594.

20. F. Du et al., Chapter 7: Vertically-Aligned Carbon Nanotubes for Electrochemical Energy Conversion and Storage, Nanomaterials for sustainable energy, Q. Li (Ed.), Springer, Switzerland, 2016.

21. C.-H. Lin, C.-H. Tsai, F.-G. Tseng, C.-C.M. Ma, H.-C. Wu, C.-K. Hsieh, Three-dimensional vertically aligned hybrid nanoarchitecture of two-dimensional molybdenum disulfide nanosheets anchored on directly grown one-dimensional carbon nanotubes for use as a counter electrode in dye-sensitized solar cells, Journal of Alloys and Compounds. 692 (2017) 941–949. doi:10.1016/j.jallcom.2016.09.149.

22. H. Dai, Carbon Nanotubes: Synthesis, Integration, and Properties, Accounts of Chemical Research. 35 (2002) 1035–1044. doi:10.1021/ar0101640.

23. I. Álvarez-Martos, A. Fernández-Gavela, J. Rodríguez-García, N. Campos-Alfaraz, A.B. García-Delgado, D. Gómez-Plaza, et al., Electrochemical

properties of spaghetti and forest like carbon nanotubes grown on glass substrates, Sensors and Actuators B: Chemical. 192 (2014) 253–260. doi:10.1016/j.snb.2013.10.088.

24. M. Chhowalla, K.B.K. Teo, C. Ducati, N.L. Rupesinghe, G.A.J. Amaratunga, A.C. Ferrari, et al., Growth process conditions of vertically aligned carbon nanotubes using plasma enhanced chemical vapor deposition, Journal of Applied Physics. 90 (2001) 5308–5317. doi:10.1063/1.1410322.

25. K. Moulton, N.B. Morrill, A.M. Konneker, B.D. Jensen, R.R. Vanfleet, D.D. Allred, et al., Effect of iron catalyst thickness on vertically aligned carbon nanotube forest straightness for CNT-MEMS, Journal of Micromechanics and Microengineering. 22 (2012) 055004. doi:10.1088/0960-1317/22/5/055004.

26. K. Bartsch, K. Biedermann, T. Gemming, A. Leonhardt, On the diffusion-controlled growth of multiwalled carbon nanotubes, Journal of Applied Physics. 97 (2005) 114301. doi:10.1063/1.1922067.

27. P. Coquay, E. Flahaut, E.D. Grave, A. Peigney, R.E. Vandenberghe, C. Laurent, Fe/Co Alloys for the Catalytic Chemical Vapor Deposition Synthesis of Single- and Double-Walled Carbon Nanotubes (CNTs). 2. The CNT−Fe/Co−MgAl2O4System, The Journal of Physical Chemistry B. 109 (2005) 17825–17830. doi:10.1021/jp052494y.

28. G.D. Nessim, Properties, synthesis, and growth mechanisms of carbon nanotubes with special focus on thermal chemical vapor deposition, Nanoscale. 2 (2010) 1306–1323. doi:10.1039/b9nr00427k.

29. X. Cai, H. Cong, C. Liu, Synthesis of vertically-aligned carbon nanotubes without a catalyst by hydrogen arc discharge, Carbon. 50 (2012) 2726–2730. doi:10.1016/j.carbon.2012.02.031.

30. N. Wang, B.D. Yao, Nucleation and growth of well-aligned, uniform-sized carbon nanotubes by microwave plasma chemical vapor depositon, Applied Physics Letters. 78 (2001) 4028–4030. doi:10.1063/1.1381036.

31. J.B. Park, S.H. Jeong, M.S. Jeong, S.C. Lim, I.H. Lee, Y.H. Lee, The rapid growth of vertically aligned carbon nanotubes using laser heating, Nanotechnology. 20 (2009) 185604. doi:10.1088/0957-4484/20/18/185604.

32. J.-H. Han, B.-S. Moon, W.S. Yang, J.-B. Yoo, C.-Y. Park, Growth characteristics of carbon nanotubes by plasma enhanced hot filament chemical vapor deposition, Surface and Coatings Technology. 131 (2000) 93–97. doi:10.1016/s0257-8972(00)00766-0.

33. S. Handuja, P. Srivastava, V.D. Vankar, On the Growth and Microstructure of Carbon Nanotubes Grown by Thermal Chemical Vapor Deposition, Nanoscale Research Letters. 5 (2010) 1211–1216. doi:10.1007/s11671-010-9628-8.

34. R.V. Salvatierra, D. Zakhidov, J. Sha, N.D. Kim, S.-K. Lee, A.-R.O. Raji, et al., Graphene Carbon Nanotube Carpets Grown Using Binary Catalysts for High-Performance Lithium-Ion Capacitors, ACS Nano. 11 (2017) 2724–2733. doi:10.1021/acsnano.6b07707.

35. K.-H. Kim, A. Gohier, J.E. Bourée, M. Châtelet, C.-S. Cojocaru, The role of catalytic nanoparticle pretreatment on the growth of vertically aligned carbon nanotubes by hot-filament chemical vapor deposition, Thin Solid Films. 575 (2015) 84–91. doi:10.1016/j.tsf.2014.10.013.

36. M. Yilmaz, S. Raina, S.H. Hsu, W.P. Kang, Growing micropatterned CNT arrays on aluminum substrates using hot-filament CVD process, Materials Letters. 209 (2017) 376–378. doi:10.1016/j.matlet.2017.08.061.

37. S.-G. Kim, S.-Y. Kim, H.-W. Lee, Effect of ammonia gas etching on growth of vertically aligned carbon nanotubes/nanofibers, Transactions of Nonferrous Metals Society of China. 21 (2011) s130–s134. doi:10.1016/s1003-6326(11)61076-5.

38. R. Brukh, S. Mitra, Mechanism of carbon nanotube growth by CVD, Chemical Physics Letters. 424 (2006) 126–132. doi:10.1016/j.cplett.2006.04.028.

39. Y. Ishikawa, H. Jinbo, Synthesis of Multiwalled Carbon Nanotubes at Temperatures below 300°C by Hot-Filament Assisted Chemical Vapor Deposition, Japanese Journal of Applied Physics. 44 (2005). doi:10.1143/jjap.44.l394.

40. C.S. Cojocaru, D. Kim, D. Pribat, J.-E. Bourée, Synthesis of multi-walled carbon nanotubes by combining hot-wire and dc plasma-enhanced chemical vapor deposition, Thin Solid Films. 501 (2006) 227–232. doi:10.1016/j.tsf.2005.07.162.

41. G.S. Bumbrah, R.M. Sharma, Raman spectroscopy – Basic principle, instrumentation and selected applications for the characterization of drugs of abuse, Egyptian Journal of Forensic Sciences. 6 (2016) 209–215. doi:10.1016/j.ejfs.2015.06.001.

42. H. Nii, Y. Sumiyama, H. Nakagawa, A. Kunishige, Influence of Diameter on the Raman Spectra of Multi-Walled Carbon Nanotubes, Applied Physics Express. 1 (2008) 064005. doi:10.1143/apex.1.064005.

43. L. Bokobza, J. Zhang, Raman spectroscopic characterization of multiwall carbon nanotubes and of composites, Express Polymer Letters. 6 (2012) 601–608. doi:10.3144/expresspolymlett.2012.63.

44. A. Bahrami, S. Mohammadnejad, S. Soleimaninezhad, Photovoltaic cells technology: principles and recent developments, Optical and Quantum Electronics. 45 (2012) 161–197. doi:10.1007/s11082-012-9613-9.

45. G. Han, S. Zhang, P.P. Boix, L.H. Wong, L. Sun, S.-Y. Lien, Towards high efficiency thin film solar cells, Progress in Materials Science. 87 (2017) 246–291. doi:10.1016/j.pmatsci.2017.02.003.

46. A. Goodrich, P. Hacke, Q. Wang, B. Sopori, R. Margolis, T.L. James, et al., A wafer-based monocrystalline silicon photovoltaics road map: Utilizing known technology improvement opportunities for further reductions in manufacturing costs, Solar Energy Materials and Solar Cells. 114 (2013) 110–135. doi:10.1016/j.solmat.2013.01.030.

47. T. Saga, Advances in crystalline silicon solar cell technology for industrial mass production, NPG Asia Materials. 2 (2010) 96–102. doi:10.1038/asiamat.2010.82.

48. T.D. Lee, A.U. Ebong, A review of thin film solar cell technologies and challenges, Renewable and Sustainable Energy Reviews. 70 (2017) 1286–1297. doi:10.1016/j.rser.2016.12.028.

49. M.P. Lumb, S. Mack, K.J. Schmieder, M. González, M.F. Bennett, D. Scheiman, et al., GaSb-Based Solar Cells for Full Solar Spectrum Energy Harvesting, Advanced Energy Materials. 7 (2017) 1700345. doi:10.1002/aenm.201700345.

50. A. Nozik, Quantum dot solar cells, Physica E: Low-Dimensional Systems and Nanostructures. 14 (2002) 115–120. doi:10.1016/s1386-9477(02)00374-0.

51. B. Oregan, M. Grätzel, A low-cost, high-efficiency solar cell based on dye-sensitized colloidal TiO2 films, Nature. 353 (1991) 737–740. doi:10.1038/353737a0.

52. J. Wu, Z. Lan, J. Lin, M. Huang, Y. Huang, L. Fan, and G. Luo, Electrolytes in Dye-Sensitized Solar Cells, Chem. Rev. 115, (2015) 2136–2173. doi: 10.1021/cr400675m

53. M.K. Nazeeruddin, E. Baranoff, M. Grätzel, Dye-sensitized solar cells: A brief overview, Solar Energy. 85 (2011) 1172–1178. doi:10.1016/j.solener.2011.01.018.

54. L. Kavan, Electrochemistry and dye-sensitized solar cells, Current Opinion in Electrochemistry. 2 (2017) 88–96. doi:10.1016/j.coelec.2017.03.008.

55. G. Kang, J. Choi, T. Park, Pt-Free Counter Electrodes with Carbon Black and 3D Network Epoxy Polymer Composites, Scientific Reports. 6 (2016). doi:10.1038/srep22987.

56. J.D. Roy-Mayhew, D.J. Bozym, C. Punckt, I.A. Aksay, Functionalized Graphene as a Catalytic Counter Electrode in Dye-Sensitized Solar Cells, ACS Nano. 4 (2010) 6203–6211. doi:10.1021/nn1016428.

57. Z. Shi, K. Deng, L. Li, Pt-free and efficient counter electrode with nanostructured CoNi2S4 for dye-sensitized solar cells, Scientific Reports. 5 (2015). doi:10.1038/srep09317.

58. J. Zhang, J. Feng, Y. Hong, Z. Hu, K. Xia, P. Wang, et al., Carbon nanotube based flexible counter electrode for quasi-solid state dye sensitized solar cells, Journal of Renewable and Sustainable Energy. 6 (2014) 043116. doi:10.1063/1.4892546.

59. J. Han, H. Kim, D.Y. Kim, S.M. Jo, S.-Y. Jang, Water-Soluble Polyelectrolyte-Grafted Multiwalled Carbon Nanotube Thin Films for Efficient Counter Electrode of Dye-Sensitized Solar Cells, ACS Nano. 4 (2010) 3503–3509. doi:10.1021/nn100574g.

60. G. Wang, L. Zhang, J. Zhang, A review of electrode materials for electrochemical supercapacitors, Chem. Soc. Rev. 41 (2012) 797–828. doi:10.1039/c1cs15060j.

61. A. Borenstein, O. Hanna, R. Attias, S. Luski, T. Brousse, D. Aurbach, Carbon-based composite materials for supercapacitor electrodes: a review, Journal of Materials Chemistry A. 5 (2017) 12653–12672. doi:10.1039/c7ta00863e.

62. Y. Liu, J. Zhou, L. Chen, P. Zhang, W. Fu, H. Zhao, et al., Highly Flexible Freestanding Porous Carbon Nanofibers for Electrodes Materials of High-

Performance All-Carbon Supercapacitors, ACS Applied Materials & Interfaces. 7 (2015) 23515–23520. doi:10.1021/acsami.5b06107.

63. Z. Wang, Z. Li, J. Feng, S. Yan, W. Luo, J. Liu, et al., MnO2 nanolayers on highly conductive TiO0.54N0.46 nanotubes for supercapacitor electrodes with high power density and cyclic stability, Physical Chemistry Chemical Physics. 16 (2014) 8521. doi:10.1039/c3cp55456b.

64. L. Yuan, X.-H. Lu, X. Xiao, T. Zhai, J. Dai, F. Zhang, et al., Flexible Solid-State Supercapacitors Based on Carbon Nanoparticles/MnO2 Nanorods Hybrid Structure, ACS Nano. 6 (2011) 656–661. doi:10.1021/nn2041279.

65. X. Zhang, D. Zhao, Y. Zhao, P. Tang, Y. Shen, C. Xu, et al., High performance asymmetric supercapacitor based on MnO2 electrode in ionic liquid electrolyte, Journal of Materials Chemistry A. 1 (2013) 3706. doi:10.1039/c3ta00981e.

66. Q. Cheng, J. Ma, H. Zhang, N. Shinya, L.-C. Qin, J. Tang, Electrodeposition of MnO2 on Carbon Nanotube Thin Films as Flexible Electrodes for Supercapacitors, Transactions of the Materials Research Society of Japan. 35 (2010) 369–372. doi:10.14723/tmrsj.35.369.

67. T. Miyasaka, T.N. Murakami, The photocapacitor: An efficient self-charging capacitor for direct storage of solar energy, Applied Physics Letters. 85 (2004) 3932–3934. doi:10.1063/1.1810630.

68. T.N. Murakami, N. Kawashima, T. Miyasaka, A high-voltage dye-sensitized photocapacitor of a three-electrode system, Chemical Communications. (2005) 3346. doi:10.1039/b503122b.

69. X. Zhang, X. Huang, C. Li, H. Jiang, Dye-Sensitized Solar Cell with Energy Storage Function through PVDF/ZnO Nanocomposite Counter Electrode, Advanced Materials. 25 (2013) 4093–4096. doi:10.1002/adma.201301088.

70. N. Bagheri, A. Aghaei, M.Y. Ghotbi, E. Marzbanrad, N. Vlachopoulos, L. Häggman, et al., Combination of Asymmetric Supercapacitor Utilizing Activated Carbon and Nickel Oxide with Cobalt Polypyridyl-Based Dye-Sensitized Solar Cell, Electrochimica Acta. 143 (2014) 390–397. doi:10.1016/j.electacta.2014.07.125.

71. A.P. Cohn, W.R. Erwin, K. Share, L. Oakes, A.S. Westover, R.E. Carter, et al., All Silicon Electrode Photocapacitor for Integrated Energy Storage and Conversion, Nano Letters. 15 (2015) 2727–2731. doi:10.1021/acs.nanolett.5b00563.

72. M. Skunik-Nuckowska, K. Grzejszczyk, P.J. Kulesza, L. Yang, N. Vlachopoulos, L. Häggman, et al., Integration of solid-state dye-sensitized solar cell with metal oxide charge storage material into photoelectrochemical capacitor, Journal of Power Sources. 234 (2013) 91–99. doi:10.1016/j.jpowsour.2013.01.101.

73. W. Wang et al., Chapter 1 - Electrochemical cells for medium- and large-scale energy storage: fundamentals, In *Advances in Batteries for Medium and Large-Scale Energy Storage*, C. Menictas, Woodhead, 2015.

74. D. G. Enos, Chapter 3 - Lead-acid batteries for medium- and large-scale energy storage, In *Advances in Batteries for Medium and Large-Scale Energy Storage*, C. Menictas, Woodhead, 2015.

75. B.B. Mckeon, J. Furukawa, S. Fenstermacher, Advanced Lead–Acid Batteries and the Development of Grid-Scale Energy Storage Systems, Proceedings of the IEEE. 102 (2014) 951–963. doi:10.1109/jproc.2014.2316823.

76. Z. Huang, G. Du, Chapter 4 - Nickel-based batteries for medium- and large-scale energy storage, In *Advances in Batteries for Medium and Large-Scale Energy Storage*, C. Menictas, Woodhead, 2015.

77. J.F. Parker, I.R. Pala, C.N. Chervin, J.W. Long, D.R. Rolison, Minimizing Shape Change at Zn Sponge Anodes in Rechargeable Ni–Zn Cells: Impact of Electrolyte Formulation, Journal of The Electrochemical Society. 163 (2015). doi:10.1149/2.1001602jes.

78. X. Lu, Z. Yang, Chapter 5 - Molten salt batteries for medium- and large-scale energy storage, In *Advances in Batteries for Medium and Large-Scale Energy Storage*, C. Menictas, Woodhead, 2015.

79. K. Nitta, S. Inazawa, S. Sakai, A. Fukunaga, E. Itani, K. Numata, R. Hagiwara, T. Nohira, Development of molten salt electrolyte battery. SEI Technical Review. 76 (2013) 33-39.

80. D. Geng, N. Ding, T.S.A. Hor, S.W. Chien, Z. Liu, D. Wuu, et al., From Lithium-Oxygen to Lithium-Air Batteries: Challenges and Opportunities, Advanced Energy Materials. 6 (2016) 1502164. doi:10.1002/aenm.201502164.

81. J.-S. Lee, S.T. Kim, R. Cao, N.-S. Choi, M. Liu, K.T. Lee, et al., Metal-Air Batteries with High Energy Density: Li-Air versus Zn-Air, Advanced Energy Materials. 1 (2010) 34–50. doi:10.1002/aenm.201000010.

82. M. Parans Paranthaman et al., Chapter 13 - Aluminum-ion batteries for medium- and large-scale energy storage, In *Advances in Batteries for Medium and Large-Scale Energy Storage*, C. Menictas, Woodhead, 2015.

83. X. Li et al., Chapter 8 - Zinc-based flow batteries for medium- and large-scale energy storage, In *Advances in Batteries for Medium and Large-Scale Energy Storage*, C. Menictas, Woodhead, 2015.

84. S. Mehboob, A. Mehmood, J.-Y. Lee, H.-J. Shin, J. Hwang, S. Abbas, et al., Excellent electrocatalytic effects of tin through in situ electrodeposition on the performance of all-vanadium redox flow batteries, Journal of Materials Chemistry A. 5 (2017) 17388–17400. doi:10.1039/c7ta05657e.

85. M. Whittingham, F.R. Gamble, The lithium intercalates of the transition metal dichalcogenides, Materials Research Bulletin. 10 (1975) 363–371. doi:10.1016/0025-5408(75)90006-9.

86. M. M. Doeff, Batteries: Overview of Battery Cathodes, In *Springer Encyclopedia of Sustainability Science and Technology*, Springer Science + Business Media, (2012) 709-739.

87. S.J. An, J. Li, C. Daniel, D. Mohanty, S. Nagpure, D.L. Wood, The state of understanding of the lithium-ion-battery graphite solid electrolyte interphase (SEI) and its relationship to formation cycling, Carbon. 105 (2016) 52–76. doi:10.1016/j.carbon.2016.04.008.

88. K. Xu, Electrolytes and Interphases in Li-Ion Batteries and Beyond, Chemical Reviews. 114 (2014) 11503–11618. doi:10.1021/cr500003w.

89. P. Roy, S.K. Srivastava, Nanostructured anode materials for lithium ion batteries, Journal of Materials Chemistry A. 3 (2015) 2454–2484. doi:10.1039/c4ta04980b.

90. J. Yang, J. Wang, Y. Tang, D. Wang, X. Li, Y. Hu, et al., LiFePO4–graphene as a superior cathode material for rechargeable lithium batteries: impact of stacked graphene and unfolded graphene, Energy & Environmental Science. 6 (2013) 1521. doi:10.1039/c3ee24163g.

91. Q. Huang, Q. Wang, Redox-assisted Li -storage in lithium-ion batteries, Chinese Physics B. 25 (2016) 018213. doi:10.1088/1674-1056/25/1/018213.

92. C. Liu, Z.G. Neale, G. Cao, Understanding electrochemical potentials of cathode materials in rechargeable batteries, Materials Today. 19 (2016) 109–123. doi:10.1016/j.mattod.2015.10.009.

93. H. Liu, J. Wang, X. Zhang, D. Zhou, X. Qi, B. Qiu, et al., Morphological Evolution of High-Voltage Spinel LiNi0.5Mn1.5O4 Cathode Materials for Lithium-Ion Batteries: The Critical Effects of Surface Orientations and Particle Size, ACS Applied Materials & Interfaces. 8 (2016) 4661–4675. doi:10.1021/acsami.5b11389.

94. M.A.-D. Dompablo, M. Armand, J. Tarascon, U. Amador, On-demand design of polyoxianionic cathode materials based on electronegativity correlations: An exploration of the Li2MSiO4 system (M=Fe, Mn, Co, Ni), Electrochemistry Communications. 8 (2006) 1292–1298. doi:10.1016/j.elecom.2006.06.003.

95. N. Bensalah, H. Dawood, Review on Synthesis, Characterizations, and Electrochemical Properties of Cathode Materials for Lithium Ion Batteries, Journal of Material Science & Engineering. 5 (2016). doi:10.4172/2169-0022.1000258.

96. Y. Shen, J.R. Eltzholtz, B.B. Iversen, Controlling Size, Crystallinity, and Electrochemical Performance of Li4Ti5O12 Nanocrystals, Chemistry of Materials. 25 (2013) 5023–5030. doi:10.1021/cm402366y.

97. B. Fultz, J. Howe, Chapter 1 - Diffraction and the X-Ray Powder Diffractometer, In *Transmission Electron Microscopy and Diffractometry of Materials*, Graduate Texts in Physics. Springer, Berlin, Heidelberg, 2013

98. B.W. Byles, N.K.R. Palapati, A. Subramanian, E. Pomerantseva, The role of electronic and ionic conductivities in the rate performance of tunnel structured manganese oxides in Li-ion batteries, APL Materials. 4 (2016) 046108. doi:10.1063/1.4948272.

99. M. Park, X. Zhang, M. Chung, G.B. Less, A.M. Sastry, A review of conduction phenomena in Li-ion batteries, Journal of Power Sources. 195 (2010) 7904–7929. doi:10.1016/j.jpowsour.2010.06.060.

100. Y.-N. Xu, S.-Y. Chung, J.T. Bloking, Y.-M. Chiang, W.Y. Ching, Electronic Structure and Electrical Conductivity of Undoped LiFePO[sub 4], Electrochemical and Solid-State Letters. 7 (2004). doi:10.1149/1.1703470.

101. S.-Y. Chung, J.T. Bloking, Y.-M. Chiang, Electronically conductive phospho-olivines as lithium storage electrodes, Nature Materials. 1 (2002) 123–128. doi:10.1038/nmat732.

102. J. Ni, Y. Zhao, J. Chen, L. Gao, L. Lu, Site-dependent electrochemical performance of Mg doped LiFePO4, Electrochemistry Communications. 44 (2014) 4–7. doi:10.1016/j.elecom.2014.04.004.

103. M. Chen, L.-L. Shao, H.-B. Yang, T.-Z. Ren, G. Du, Z.-Y. Yuan, Vanadium-doping of LiFePO4/carbon composite cathode materials synthesized with organophosphorus source, Electrochimica Acta. 167 (2015) 278–286. doi:10.1016/j.electacta.2015.03.185.

104. D. Choi, P.N. Kumta, Surfactant based sol–gel approach to nanostructured LiFePO4 for high rate Li-ion batteries, Journal of Power Sources. 163 (2007) 1064–1069. doi:10.1016/j.jpowsour.2006.09.082.

105. J. Gim, V. Mathew, J. Lim, J. Song, S. Baek, J. Kang, et al., Pyro-Synthesis of Functional Nanocrystals, Scientific Reports. 2 (2012). doi:10.1038/srep00946.

106. L. Bao, L. Li, G. Xu, J. Wang, R. Zhao, G. Shen, et al., Olivine LiFePO 4 nanocrystallites embedded in carbon-coating matrix for high power Li-ion batteries, Electrochimica Acta. 222 (2016) 685–692. doi:10.1016/j.electacta.2016.11.024.

107. R. Tian, H. Liu, Y. Jiang, J. Chen, X. Tan, G. Liu, et al., Drastically Enhanced High-Rate Performance of Carbon-Coated LiFePO4 Nanorods Using a Green Chemical Vapor Deposition (CVD) Method for Lithium Ion Battery: A Selective Carbon Coating Process, ACS Applied Materials & Interfaces. 7 (2015) 11377–11386. doi:10.1021/acsami.5b01891.

108. H.C. Shin, W.I. Cho, H. Jang, Electrochemical properties of the carbon-coated LiFePO4 as a cathode material for lithium-ion secondary batteries, Journal of Power Sources. 159 (2006) 1383–1388. doi:10.1016/j.jpowsour.2005.12.043.

109. Y.-G. Huang, F.-H. Zheng, X.-H. Zhang, Q.-Y. Li, H.-Q. Wang, Effect of carbon coating on cycle performance of LiFePO4/C composite cathodes using Tween80 as carbon source, Electrochimica Acta. 130 (2014) 740–747. doi:10.1016/j.electacta.2014.03.091.

110. W.-B. Luo, S.-L. Chou, Y.-C. Zhai, H.-K. Liu, Self-assembled graphene and LiFePO4 composites with superior high rate capability for lithium ion batteries, Journal of Materials Chemistry A. 2 (2014) 4927. doi:10.1039/c3ta14471b.

111. L.-H. Hu, F.-Y. Wu, C.-T. Lin, A.N. Khlobystov, L.-J. Li, Graphene-modified LiFePO4 cathode for lithium ion battery beyond theoretical capacity, Nature Communications. 4 (2013) 1687. doi:10.1038/ncomms2705.

112. J.-P. Jegal, K.-B. Kim, Carbon nanotube-embedding LiFePO4 as a cathode material for high rate lithium ion batteries, Journal of Power Sources. 243 (2013) 859–864. doi:10.1016/j.jpowsour.2013.06.090.

113. W.-B. Luo, L. Wen, H.-Z. Luo, R.-S. Song, Y.-C. Zhai, C. Liu, et al., Carbon nanotube-modified LiFePO4 for high rate lithium ion batteries, New Carbon Materials. 29 (2014) 287–294. doi:10.1016/s1872-5805(14)60138-4.

114. X.-L. Wu, Y.-G. Guo, J. Su, J.-W. Xiong, Y.-L. Zhang, L.-J. Wan, Carbon-Nanotube-Decorated Nano-LiFePO4@C Cathode Material with Superior High-Rate and Low-Temperature Performances for Lithium-Ion Batteries, Advanced Energy Materials. 3 (2013) 1155–1160. doi:10.1002/aenm.201300159.

115. I.V. Thorat, V. Mathur, J.N. Harb, D.R. Wheeler, Performance of carbon-fiber-containing LiFePO4 cathodes for high-power applications, Journal of Power Sources. 162 (2006) 673–678. doi:10.1016/j.jpowsour.2006.06.032.

116. C.Y. Wu, G.S. Cao, H.M. Yu, J. Xie, X.B. Zhao, In Situ Synthesis of LiFePO4/Carbon Fiber Composite by Chemical Vapor Deposition with Improved Electrochemical Performance, The Journal of Physical Chemistry C. 115 (2011) 23090–23095. doi:10.1021/jp205146d.

117. J. Gomez, E.E. Kalu, R. Nelson, C. Akpovo, M.H. Weatherspoon, J.P. Zheng, Binder-Free Electrode Fabrication by Electroless-Electrolytic Method, ECS Electrochemistry Letters. 1 (2012). doi:10.1149/2.007206eel.

118. S. Luo, K. Wang, J. Wang, K. Jiang, Q. Li, S. Fan, Binder-Free LiCoO2/Carbon Nanotube Cathodes for High-Performance Lithium Ion Batteries, Advanced Materials. 24 (2012) 2294–2298. doi:10.1002/adma.201104720.

119. A. Guerfi, M. Kaneko, M. Petitclerc, M. Mori, K. Zaghib, LiFePO4 water-soluble binder electrode for Li-ion batteries, Journal of Power Sources. 163 (2007) 1047–1052. doi:10.1016/j.jpowsour.2006.09.067.

120. C. Daniel, Lithium Ion Batteries and Their Manufacturing Challenges. In *The Bridge*; Latanision, R.M., Fletcher, C.H. (Eds.); National Academy of Engineering: Washington, DC, USA, 2015; Volume 45, pp. 21–24

121. A.W. Golubkov, D. Fuchs, J. Wagner, H. Wiltsche, C. Stangl, G. Fauler, et al., Thermal-runaway experiments on consumer Li-ion batteries with metal-oxide and olivin-type cathodes, RSC Adv. 4 (2014) 3633–3642. doi:10.1039/c3ra45748f.

122. Y. Zeng, G. Gao, G. Wu, H. Yang, Nanosheet-structured vanadium pentoxide thin film as a carbon- and binder-free cathode for lithium-ion battery applications, Journal of Solid State Electrochemistry. 19 (2015) 3319–3328. doi:10.1007/s10008-015-2941-5.

123. B.S. Lalia, T. Shah, R. Hashaikeh, Microbundles of carbon nanostructures as binder free highly conductive matrix for LiFePO4 battery cathode, Journal of Power Sources. 278 (2015) 314–319. doi:10.1016/j.jpowsour.2014.12.079.

124. K.V. Sreelakshmi, S. Sasi, A. Balakrishnan, N. Sivakumar, A.S. Nair, S.V. Nair, et al., Hybrid Composites of LiMn2O4-Graphene as Rechargeable Electrodes in Energy Storage Devices, Energy Technology. 2 (2014) 257–262. doi:10.1002/ente.201300120.

125. Y. Huang, H. Liu, Y.-C. Lu, Y. Hou, Q. Li, Electrophoretic lithium iron phosphate/reduced graphene oxide composite for lithium ion battery cathode application, Journal of Power Sources. 284 (2015) 236–244. doi:10.1016/j.jpowsour.2015.03.037.

126. R. Liu, H. Zhang, Y. Huang, W. Wang, Z. Li, Z. Yu, et al., In situ gelatin carbonation to prepare a binder-free LiFePO4 cathode for high-power lithium ion batteries, Electrochimica Acta. 78 (2012) 563–568. doi:10.1016/j.electacta.2012.06.052.

127. V.F. Lvovich, Fundamentals of Electrochemical Impedance Spectroscopy, In *Impedance Spectroscopy Applications to Electrochemical and Dielectric Phenomena*, Wiley, Chicester, 2012.

128. S. Akbulut, M. Yilmaz, S. Raina, S.-H. Hsu, W.P. Kang, Solid-state supercapacitor cell based on 3D nanostructured MnO 2 /CNT microelectrode array on graphite and H 3 PO 4 /PVA electrolyte, Diamond and Related Materials. 74 (2017) 222–228. doi:10.1016/j.diamond.2017.03.016.

129. S. Raina, Nanodiamond macroelectrodes and ultramicroelectrode arrays for bio-analyte detection, dissertation, 2011.

130. N. Koide, L. Han, Measuring methods of cell performance of dye-sensitized solar cells, Review of Scientific Instruments. 75 (2004) 2828–2831. doi:10.1063/1.1784556.

131. W. Maiaugree, S. Lowpa, M. Towannang, P. Rutphonsan, A. Tangtrakarn, S. Pimanpang, et al., A dye sensitized solar cell using natural counter

electrode and natural dye derived from mangosteen peel waste, Scientific Reports. 5 (2015). doi:10.1038/srep15230.

132. P. Poudel, L. Zhang, P. Joshi, S. Venkatesan, H. Fong, Q. Qiao, Enhanced performance in dye-sensitized solar cells via carbon nanofibers–platinum composite counter electrodes, Nanoscale. 4 (2012) 4726. doi:10.1039/c2nr30586k.

133. J. Velten, A.J. Mozer, D. Li, D. Officer, G. Wallace, R. Baughman, et al., Carbon nanotube/graphene nanocomposite as efficient counter electrodes in dye-sensitized solar cells, Nanotechnology. 23 (2012) 085201. doi:10.1088/0957-4484/23/8/085201.

134. H. Anwar, A.E. George, I.G. Hill, Vertically-aligned carbon nanotube counter electrodes for dye-sensitized solar cells, Solar Energy. 88 (2013) 129–136. doi:10.1016/j.solener.2012.11.013.

135. L. Kavan, Exploiting Nanocarbons in Dye-Sensitized Solar Cells, Making and Exploiting Fullerenes, Graphene, and Carbon Nanotubes Topics in Current Chemistry. (2013) 53–93. doi:10.1007/128_2013_447.

136. Y. Chen, X. Zhang, Q. Tao, W. Fu, H. Yang, S. Su, et al., High catalytic activity of a PbS counter electrode prepared via chemical bath deposition for quantum dots-sensitized solar cells, RSC Advances. 5 (2015) 1835–1840. doi:10.1039/c4ra08076a.

137. L. Kavan, J.H. Yum, Grätzel Michael, Optically Transparent Cathode for Dye-Sensitized Solar Cells Based on Graphene Nanoplatelets, ACS Nano. 5 (2011) 165–172. doi:10.1021/nn102353h.

138. P. Simon, Y. Gogotsi, Materials for electrochemical capacitors, Nature Materials. 7 (2008) 845–854. doi:10.1038/nmat2297.

139. G. Boschloo, A. Hagfeldt, Characteristics of the Iodide/Triiodide Redox Mediator in Dye-Sensitized Solar Cells, Accounts of Chemical Research. 42 (2009) 1819–1826. doi:10.1021/ar900138m.

140. W. Yuan, Y. Zhang, L. Cheng, H. Wu, L. Zheng, D. Zhao, The applications of carbon nanotubes and graphene in advanced rechargeable lithium batteries, Journal of Materials Chemistry A. 4 (2016) 8932–8951. doi:10.1039/c6ta01546h.

141. M. Hughes, G.Z. Chen, M.S.P. Shaffer, D.J. Fray, A.H. Windle, Electrochemical Capacitance of a Nanoporous Composite of Carbon

Nanotubes and Polypyrrole, Chemistry of Materials. 14 (2002) 1610–1613. doi:10.1021/cm010744r.

142. M. Yang, J. Hou, Membranes in Lithium Ion Batteries, Membranes. 2 (2012) 367–383. doi:10.3390/membranes2030367.

143. S.S. Zhang, A review on the separators of liquid electrolyte Li-ion batteries, Journal of Power Sources. 164 (2007) 351–364. doi:10.1016/j.jpowsour.2006.10.065.

144. K. Perera, M.A.K.L. Dissanayake, Conductivity variation of the liquid electrolyte, EC : PC : LiCF3SO3 with salt concentration, Sri Lankan Journal of Physics. 7 (2006) 1–5. doi:10.4038/sljp.v7i0.202.

145. D. W. Olson, Graphite, U.S. Geological Survey, (2013) 32.1

146. C. Deng, S. Zhang, S. Yang, Effect of Mn substitution on the structural, morphological and electrochemical behaviors of Li2Fe1−xMnxSiO4 synthesized via citric acid assisted sol–gel method, Journal of Alloys and Compounds. 487 (2009). doi:10.1016/j.jallcom.2009.08.007.

147. Y. Wang, D. Su, G. Wang, The Effect of Carbon Coating on the Electrochemical Performance of Nanosized Li2FeSiO4Cathode Materials, Acta Physica Polonica A. 123 (2013) 279–282. doi:10.12693/aphyspola.123.279.

148. What is ICP-MS?... and more importantly, what can it do?, Introduction to ICP-MS. (n.d.). https://crustal.usgs.gov/laboratories/icpms/intro.html (accessed December 11, 2017).

149. A. Nytén, S. Kamali, L. Häggström, T. Gustafsson, J.O. Thomas, The lithium extraction/insertion mechanism in Li2FeSiO4, J. Mater. Chem. 16 (2006) 2266–2272. doi:10.1039/b601184e.

150. J. Yang, X. Kang, D. He, T. Peng, L. Hu, S. Mu, Hierarchical shuttle-like Li2FeSiO4 as a highly efficient cathode material for lithium-ion batteries, Journal of Power Sources. 242 (2013) 171–178. doi:10.1016/j.jpowsour.2013.05.088.

151. Z. Yan, S. Cai, X. Zhou, Y. Zhao, L. Miao, Sol-Gel Synthesis of Nanostructured Li2FeSiO4/C as Cathode Material for Lithium Ion Battery, Journal of The Electrochemical Society. 159 (2012). doi:10.1149/2.110206jes.

152. L. Qu, S. Fang, L. Yang, S.-I. Hirano, Synthesis and characterization of high capacity Li2MnSiO4/C cathode material for lithium-ion battery, Journal of Power Sources. 252 (2014) 169–175. doi:10.1016/j.jpowsour.2013.11.076.

153. X. Lu, H. Wei, H.-C. Chiu, R. Gauvin, P. Hovington, A. Guerfi, et al., Rate-dependent phase transitions in Li2FeSiO4 cathode nanocrystals, Scientific Reports. 5 (2015). doi:10.1038/srep08599.

154. M.M. Kalantarian, M. Oghbaei, S. Asgari, S. Ferrari, D. Capsoni, P. Mustarelli, Understanding non-ideal voltage behaviour of cathodes for lithium-ion batteries, J. Mater. Chem. A. 2 (2014) 19451–19460. doi:10.1039/c4ta04341c.

155. A. Saracibar, A.V.D. Ven, M.E.A.-D. Dompablo, Crystal Structure, Energetics, And Electrochemistry of Li2FeSiO4 Polymorphs from First Principles Calculations, Chemistry of Materials. 24 (2012) 495–503. doi:10.1021/cm202818u.

156. J.A. Seel, J.R. Dahn, Electrochemical Intercalation of PF6 into Graphite, Journal of The Electrochemical Society. 147 (2000) 892–898. doi:10.1149/1.1393288.

157. J.A. Read, In-Situ Studies on the Electrochemical Intercalation of Hexafluorophosphate Anion in Graphite with Selective Cointercalation of Solvent, The Journal of Physical Chemistry C. 119 (2015) 8438–8446. doi:10.1021/jp5115465.

158. I.B. Dogru, M.B. Durukan, O. Turel, H.E. Unalan, Flexible supercapacitor electrodes with vertically aligned carbon nanotubes grown on aluminum foils, Progress in Natural Science: Materials International. 26 (2016) 232–236. doi:10.1016/j.pnsc.2016.05.011.

159. S. Dörfler, I. Felhösi, T. Marek, S. Thieme, H. Althues, L. Nyikos, et al., High power supercap electrodes based on vertical aligned carbon nanotubes on aluminum, Journal of Power Sources. 227 (2013) 218–228. doi:10.1016/j.jpowsour.2012.11.068.

160. N. Yoshikawa, T. Asari, N. Kishi, S. Hayashi, T. Sugai, H. Shinohara, An efficient fabrication of vertically aligned carbon nanotubes on flexible aluminum foils by catalyst-supported chemical vapor deposition, Nanotechnology. 19 (2008) 245607. doi:10.1088/0957-4484/19/24/245607.

161. S. Liatard, K. Benhamouda, A. Fournier, R. Ramos, C. Barchasz, J. Dijon, Vertically-aligned carbon nanotubes on aluminum as a light-weight positive

electrode for lithium-polysulfide batteries, Chemical Communications. 51 (2015) 7749–7752. doi:10.1039/c4cc08848d.

162. MTI Corporation, LiFePO4 (Phosphate) Powder for Li-ion Battery Cathode, MTIXTL, http://www.mtixtl.com/LiFePO4PowderforLi-ionBatteryCathode-EQ-Lib-LFPO-S21.aspx (2017), Accessed 15 April 2017

163. E.V. Hooijdonk, C. Bittencourt, R. Snyders, J.-F. Colomer, Functionalization of vertically aligned carbon nanotubes, Beilstein Journal of Nanotechnology. 4 (2013) 129–152. doi:10.3762/bjnano.4.14.

164. R.D. Gately, M.I.H. Panhuis, Filling of carbon nanotubes and nanofibres, Beilstein Journal of Nanotechnology. 6 (2015) 508–516. doi:10.3762/bjnano.6.53.

165. S.C. Boncel, K.Z. Walczak, K.K.K. Koziol, Dynamics of capillary infiltration of liquids into a highly aligned multi-walled carbon nanotube film, Beilstein Journal of Nanotechnology. 2 (2011) 311–317. doi:10.3762/bjnano.2.36.

166. I. Chakraborty, N. Singh, S. Gohil, S. Ghosh, P. Ayyub, Clustered copper nanorod arrays: a new class of adhesive hydrophobic materials, Soft Matter. 9 (2013) 11513. doi:10.1039/c3sm52243a.

167. D. Chandra, S. Yang, A.A. Soshinsky, R.J. Gambogi, Biomimetic Ultrathin Whitening by Capillary-Force-Induced Random Clustering of Hydrogel Micropillar Arrays, ACS Applied Materials & Interfaces. 1 (2009) 1698–1704. doi:10.1021/am900253z.

168. F. Pan, W.-L. Wang, D. Chen, W. Yan, Influence of LiFePO4/C interface on electrochemical properties, Journal of Materials Chemistry. 21 (2011) 14680. doi:10.1039/c1jm11551k.

169. D.A. Howey, P.D. Mitcheson, V. Yufit, G.J. Offer, N.P. Brandon, Online Measurement of Battery Impedance Using Motor Controller Excitation, IEEE Transactions on Vehicular Technology. 63 (2014) 2557–2566. doi:10.1109/tvt.2013.2293597.

170. D.D. Macdonald, Reflections on the history of electrochemical impedance spectroscopy, Electrochimica Acta. 51 (2006) 1376–1388. doi:10.1016/j.electacta.2005.02.107.

171. M.R. Roberts, A. Madsen, C. Nicklin, J. Rawle, M.G. Palmer, J.R. Owen, et al., Direct Observation of Active Material Concentration Gradients and Crystallinity Breakdown in LiFePO4 Electrodes During Charge/Discharge

Cycling of Lithium Batteries, The Journal of Physical Chemistry C. 118 (2014) 6548–6557. doi:/10.1021/jp411152s.

172. J. Molenda, A. Kulka, A. Milewska, W. Zając, K. Świerczek, Structural, Transport and Electrochemical Properties of LiFePO4 Substituted in Lithium and Iron Sublattices (Al, Zr, W, Mn, Co and Ni), Materials. 6 (2013) 1656–1687. doi:10.3390/ma6051656.

173. MTI Corporation, Li-Ion Battery Cathode - Aluminum Foil Single Side Coated by LiMn2O4 (241mm L x 200mm W x 0.1mm Thickness) 5 sheets/bag bc-af-241mn-ss, MTIXTL, http://www.mtixtl.com/Li-IonBatteryCathode-AluminumfoilsinglesidecoatedbyLiMn2O4267mm.aspx (2018), Accessed 18 April 2018

174. S. Patole, P. Alegaonkar, H.-C. Lee, J.-B. Yoo, Optimization of water assisted chemical vapor deposition parameters for super growth of carbon nanotubes, Carbon. 46 (2008) 1987–1993. doi:10.1016/j.carbon.2008.08.009.

175. B. Kim, H. Chung, W. Kim, High-performance supercapacitors based on vertically aligned carbon nanotubes and nonaqueous electrolytes, Nanotechnology. 23 (2012) 155401. doi:10.1088/0957-4484/23/15/155401.

176. K. Hata, Water-Assisted Highly Efficient Synthesis of Impurity-Free Single-Walled Carbon Nanotubes, Science. 306 (2004) 1362–1364. doi:10.1126/science.1104962.

177. J. Wang, Y. Yamada, K. Sodeyama, C.H. Chiang, Y. Tateyama, A. Yamada, Superconcentrated electrolytes for a high-voltage lithium-ion battery, Nature Communications. 7 (2016). doi:10.1038/ncomms12032.

178. O. Drozhzhin, V. Shevchenko, M. Zakharkin, P. Gamzyukov, L. Yashina, A. Abakumov, et al., Improving salt-to-solvent ratio to enable high-voltage electrolyte stability for advanced Li-ion batteries, Electrochimica Acta. 263 (2018) 127–133. doi:10.1016/j.electacta.2018.01.037.

179. R.J. Moffat, Contributions to the Theory of Single-Sample Uncertainty Analysis, Journal of Fluids Engineering. 104 (1982) 250. doi:10.1115/1.3241818.